January 2009

Mechanisms of Feedback in the Visual System

Adam Eggebrecht
Washington University in St. Louis

WASHINGTON UNIVERSITY
Department of Physics

Dissertation Examination Committee:
Ralf Wessel, Chair
Anders E. Carlsson
James G. Miller
Zohar Nussinov
Erik Herzog
Kurt Thoroughman

MECHANISMS OF FEEDBACK IN THE VISUAL SYSTEM

by

Adam Thomas Eggebrecht

A dissertation presented to the
Graduate School of Arts and Sciences
of Washington University in
partial fulfillment of the
requirements for the degree
of Doctor of Philosophy

August 2009

Saint Louis, Missouri

ACKNOWLEDGEMENTS

I would not be where I am today, or who I am, without the support of the people whom I have had around me. I feel very fortunate to have the motivation and encouragement of family, friends, and esteemed colleagues.

First and foremost I am greatly indebted to my advisor for the last six years, Ralf Wessel. His patience and support are limitless. Ralf has always been willing to discuss an idea, no matter how ridiculous. He was always supportive and positive as I dealt with troubleshooting a new preparation for the lab. Ralf supported me when I felt the need to explore a rabbit hole of an idea which may or may not pan out to be helpful or relevant to my work. He always happily guided me back to focus, or welcomed in a new line of attack on a question we were dealing with. Ralf's ability to explain concepts from a variety of perspectives and his easy going and positive demeanor have made working with him in the lab a real treat.

I doubt if I would have applied to a graduate school without the support and conversation of Dr. John Clark. His kindness and passions for science and Frank Herbert novels were very appreciated when I was trying to figure out what I wanted to do with myself years ago.

My doctorate career would not have been the same had it not been for the ability to stop in and chat with Becky Trousil; always a fantastic and supportive sounding board, Becky's perspective in the department as a teacher and a recent PhD student made the hectic times of TAing and writing a thesis a lot easier to handle. Becky, thank you so much for all the time you spent with me and spend with (it seems) hundreds of people a week. I swear you are the hardest working person around here.

Ed Gruberg is another mentor who cannot go unmentioned. If only we had a racquetball court in the lab, so many more questions would have their answers illuminated! Ed is a rare spirit and a joy to interact with. I hope to see you on the court again soon, Ed.

No experimentalist here can get anything done without the shop. Todd Hardt, Tony Biondo, and Denny Huelsman are artists of the highest regard with their machines and tools. Thank you guys so much for explaining what you have and for working out the most ridiculous of designs for what we needed at the time. I still cannot believe how many things we buy have both metric and standard bolt holes. The shop class is one of the best things this department has to offer.

I am convinced nothing would get done around here if not for the amazing office staff. Julia, Allison, Sarah, Tammy, Urma, Trecia, and Jamie: thank you all so much for all that you do (or did) here. It is quite obvious the place would implode without all of you. Thanks for helping with all of the details. Mary, Rita, and Darren should not go unmentioned as without them this department would be a much dirtier and boring place.

It has been a lot of fun working in an incredibly diverse lab group. Thanks Matt, Jing (!!!), Dev, Dihui, David, Daniel for all of the good conversation. I especially want to mention Reza Khanbabaie. Reza taught me the way in the lab; his presence and conversation has been missed.

I think now of my friends with whom I have made it through this process: Seth Bartel, Adam Bauer, Allyson Gibson, Kasey Wagoner, and others. I know that some of you decided it was easier to quit and get an MD (Seth), but that turned out really well because then we could talk about orgo as a nice distraction from one of Ogilvie's Stat-Mech homework sets. I still find it odd that none of us can hang out without at least once bringing up some crazy physics thing we still find hard to believe. We may be mountain biking, canoeing in Lake Superior, playing bridge, playing music, or hiking, and the conversation will always come back to our passions like music or…well, physics. It is great to be surrounded by people who have figured out how to do something they really do love and find fascinating. It is hard to believe that it has been six years. Well, here we all are.

I have had the great fortune in life to have infinitely supportive parents. Words cannot do justice to how much I appreciate your love and support (and food, and explanations) over the years. Thank you guys for always believing in me and supporting me. Bop and Muck (Tom and Betty)—I would not be the person I am without you guys. Thank you for the music, the cards lessons, everything.

Lastly, Ashley, you are my best friend, and I thank you so very much for everything you have put up with in helping me finish this crazy degree. I know that being the wife and partner of a scientist has its moments with the ridiculously late nights of taking data and the proofreading I have asked of you. I can't imagine a better person to be spending my life with. Thank you for your patience and for always believing in me. Now, at last, let's go camping with Oscar.

PREFACE

The simulation in Chapter 4 of this dissertation was coded by Dihui Lai.

Chapter 5 of this dissertation is currently under preparation for publication as a joint paper with Matt Caudill. I performed all of the *in vivo* experiments and Matt Caudill performed all of the *in vitro* experiments.

ABSTRACT OF THE DISSERTATION

Mechanisms of feedback within the visual system

By

Adam Thomas Eggebrecht

Doctor of Philosophy in Physics

Washington University in St. Louis, 2009

Professor Ralf Wessel, Chairperson

Feedback is an ubiquitous feature of neural systems though there is little consensus on the roles of mechanisms involved with feedback. We set up an *in vivo* preparation to study and characterize an accessible and isolated feedback loop within the visual system of the leopard frog, *Rana pipiens*. We recorded extracellularly within the nucleus isthmi, a nucleus providing direct topographic feedback to the optic tectum, a nucleus that receives the vast majority of retinal output. The optic tectum and nucleus isthmi of the amphibian are homologous structures to the superior colliculus and parabigeminal nucleus in mammals, respectively. We formulated a novel threshold for detecting neuronal spikes within a low signal-to-noise environment, as exists in the nucleus isthmi due to its high density of small neuronal cell bodies. Combining this threshold with a recently developed spike sorting procedure enabled us to extract simultaneous recordings from up to 7 neurons at a time from a single extracellular electrode. We then stimulated the frog using computer driven dynamic spatiotemporal

visual stimuli to characterize the responses of the nucleus isthmi neurons. We found that the responses display surprisingly long time courses to simple visual stimuli. Furthermore, we found that when stimulated with complex contextual stimuli the response of the nucleus isthmi is quite counter-intuitive. When a stimulus is presented outside of the classical receptive field along with a stimulus within the receptive field, the response is actually higher than the response to just a stimulus within the classical receptive field. Finally, we compared the responses of all of the simultaneously recorded neurons and, together with data from *in vitro* experiments within the nucleus isthmi, conclude that the nucleus isthmi of the frog is composed of just one electrophysiological population of cells.

TABLE OF CONTENTS

LIST OF TABLES AND FIGURES

Chapter 1

dorsal pallium to the retino-recipient midbrain are not shown. (Modified after Ch. 4 in McIlwain 1996.)

Figure 1.5 011

A slightly more detailed schematic of the collothalamic visual pathway and its cholinergic modulation in the superior colliculus (optic tectum) via the reciprocally connected parabigeminal nucleus (nucleus isthmi). Listed for clarity are the brain areas for reptiles, birds, and mammals. (Modified after Ch. 4 in McIlwain 1996.)

Figure 1.6 013

General frog (*Rana pipiens*) anatomy. **A.** Whole frog brain. The forebrain, or telencephalon, can be seen to the right. The OT are the two large lobes in the middle. Immediately behind the OT is the cerebellum, and behind that is the hindbrain. **B.** A parasagittal schematic of the frog brain. Note that the NI lies directly below the caudal OT. **C.** A schematic detailing the general connectivity of the visual system. B denotes the area of the OT which responds to stimuli within the bilateral region of the visual field. M denotes the region in the OT which responds to stimuli presented into the monocular visual fields. (B and C are adapted from Winkowski et al., 2005.)

Figure 1.7 015

General connectivity in the early visual system of *Rana pipiens*. Four physiologically distinct RGC types project to three well separated layers within layer 9 of the superficial optic tectum. RGC I and II terminate in layers 9A and 9B, RGC III and V terminate in layer 9D, and RGC IV terminates in 9F and part of layer G which lies within layer 8. Glutamate (Glu) is the primary neurotransmitter of the RGC axons. Cell bodies within layer 6 of the OT send narrow dendrites up through layer 9 and synapse with collaterals from multiple RGC axon classes. These cells project to the ipsilateral NI using acetylcholine (ACh) as the neurotransmitter. Separate populations within the NI project to the ipsilateral (II) and contralateral (I & III) OT. The ispilateral projection terminates throughout the superficial OT (dark blue box) but does not appear to projecxt as superficially or as deeply as the contralateral projection (orange boxes). The NI uses ACh as its neurotransmitter and is the primary source for ACh within the OT. The OT also contains wide field neurons with cell bodies in layer 8 and dendrites which broadly ramify throughout layer 9. These project axons out of the OT via layer 7 to other areas of the brain. (Adapted and modified from Szekely et al., 1976; Khalil et al., 1977).

Chapter 2

Chapter 3

have similar sensitivities. 90º corresponds to the superior visual field. 180º corresponds to the nasal visual field. Colors represent different units. All units were recorded simultaneously at one location.

Figure 3.5 096

Delayed response to cessation of movement. White section denotes movement of spot. Colored section denotes the lack of motion. Width of the green section denotes the expected latency of response given the delay these units had when responding to both a screen flash and the commencement of motion. The tan section denotes the continued lack of motion of the spot on the screen. Top trace is a sample raw voltage trace. Below that is the multiunit average firing rate. Below that are the sorted responses showing the 4 trials in raster plots and their respective average firing rates. All scale bars for individual units correspond to 50 Hz. See text for details.

Figure 3.6 098

Timing of the responses to different looming stimuli. **(A)** The response over the three seconds before collision with the looming object. **(B)** The response over the final second of approach. The firing rate is shown in black in Hz. Bin size for firing rate is 30 ms. Red is the object's angular size in degrees. Blue is the angular velocity in degrees per second. All units use the same scale to the left. Time is in seconds.

Figure 3.7 099

Timing of peak in response relative to collision time. Different colors refer to different units. Object diameter over velocity is twice the β value. See text for details.

Figure 3.8 100

Sample response to the start of a looming spot. Black vertical bar at bottom denotes the time of impact. Tan section denotes time after impact. Blue section denotes that the spot has stopped enlarging and its extent is greater than the extent of the multiunit classical receptive field. The stimulus had a β-value equal to 25. White section corresponds to time during looming of spot. Top trace is a sample raw voltage trace. Below that is the multiunit average firing rate. Below that are the sorted responses showing 4of the 10 trials in raster plots and their

Chapter 4

Chapter 5

Figure 5.3 152

Principal component analysis of the cellular properties of NI neurons. **(A)** Ten different measurements taken from each cell are plotted in separate columns. Colored circles represent individual cells. Note for some measurements only 6 or 7 cells are shown. This is due to deterioration of cellular responses for recordings exceeding 20 mins. **(B)** Eigenvalues determined by a principal component analysis of the 6 cells that appear in all 10 columns of A are shown in the inset. The larger figure shows that the first two eigenvalues account for >90% of the data's variance. This motivates the choice to keep only two principal components (eigenvectors). **(C)** Projection of standardized measurements in A onto the principal components corresponding to the largest two eigenvalues in B is distributed about the mean values (standardized to be 0). Thus no discrete clusters are apparent for these 6 cells in the 2-dimensional principal component space.

Figure 5.4 154

Sorted spike shapes and associated ISI distributions. In this penetration, there were 72,563 detected spikes. **(A)** Average spike shape of whole set of spikes (top) and of each cluster. **(B)** Associated ISI distributions for all of the spikes (top) and for each cluster in response to the diffuse illumination steps. Note the lack of refractory period for the whole group of spikes shown by large values at low ISI value. After clustering, none of the clusters displays ISIs under 1ms.

Figure 5.5 155

Probability distributions of the normalized responses of all recorded units to salient features of the responses to visual stimuli. **(A)** Responses to the close approach of a looming spot. **(B)** Responses to the delayed response of the cessation of a moving spot moving superior-inferiorly. **(C)** Responses to the ON step of diffuse illumination. All abscissa are unit less due to being normalized by the total number of spikes fired in response to a given stimulus paradigm by a given unit.

Figure 5.6 156

Projection of principle component scores onto the plane of first two principle components. Note the lack of any clear distinction between possible multiple clusters.

Chapter 1:

INTRODUCTION

"*What we observe is not nature itself, but nature exposed to our method of questioning.*"

--Werner Heisenberg, 1958.

The effects of feedback are profound and ubiquitous within neural tissue. Understanding the roles of feedback along all of the stages of neural processing is of central importance in designing brain interface devices (e.g., cochlear implants, retinal prosthetics), treating disastrous disorders and diseases of the nervous system (e.g. epilepsy, schizophrenia, Alzheimer's), and gaining a full understanding of how brains process and integrate vastly enormous amounts of information in parallel in functionally small periods of time. This project takes a small step in this direction.

As you sit there reading these words, the information contained therein is being decoded by the higher centers of your brain. However, before that happens there is an enormous amount of stuff going on. Your eyes are alternately staring at points on the page and then suddenly shifting to a new spot to fixate; this shift is called a saccade. During the periods of fixation (but not the saccades!), the higher areas of your brain are processing the information being

expelled by the retina. There are photoreceptors within your retina that are capturing the photons, constantly arriving from the page you are reading, and transducing the energy of the photon via a conformational change in a photo-sensitive protein within the photoreceptor. The information which enters your eye is filtered and compressed within the layers of the retina and sent to your brain via the axons of the retinal ganglion cells (RGCs). Absolutely all of the information about the visual world in your brain got there via the RGCs.

Within the retina, there has already been a large amount of feedback contributing to the processing. The horizontal cells, which synapse with the photoreceptors and the bipolar cells, control the sensitivity of your eye via contrast gain control. They regulate your ability to perceive images in a dark or light environment so that you can always discern relative contrasts around a given mean illumination level.

The processing which takes place with the brain occurs on many levels simultaneously (**Fig. 1.1**). What you perceive as 'reading this book' depends profoundly on what is happening with the circuits within the brain, the centers which are connected by those circuits, the neurons within the neural centers, and the molecular and ion channels within those neurons. At each of these levels there exist feedback loops which control the interactions. We are herein concerned with the feedback loops at the levels of individual interacting neurons and populations of interacting neurons; that is, between neural centers.

As we trace the flow of information from the retina back further into the brain in primates, the primary visual pathway flows to the optic chiasm **(Fig 1.2).** In this region, fibers split off, the largest group heading to the lateral geniculate

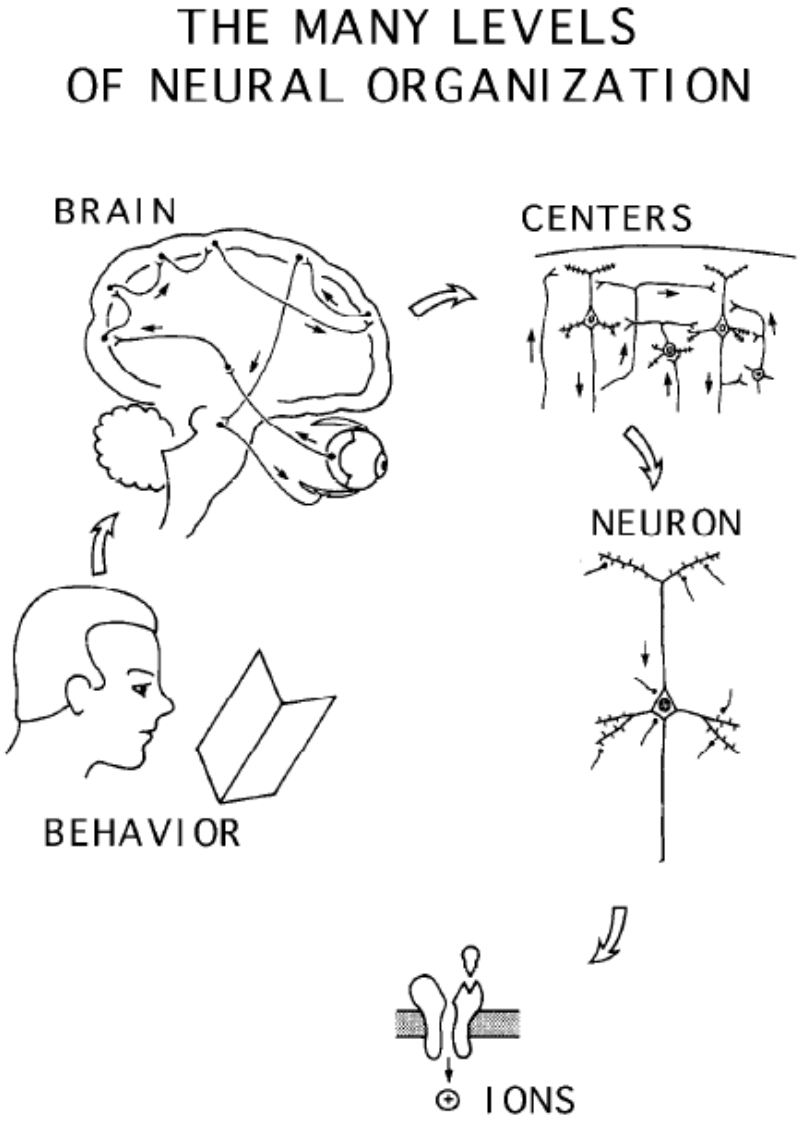

Figure 1.1: Diagrammatic representation of the hierarchy of the organization of the nervous system, from single molecule interactions to behavior. (Modified after Shepherd, 1988).

nucleus (LGN), the visual section of a large mid-brain structure called the thalamus. All of the primary sensory pathways flow through the thalamus en route to the cortex and higher brain centers. The primary visual pathway proceeds from the LGN to the primary visual cortex. After the visual cortex, the information continues on to higher brain centers. However, this explanation has only taken into account the feed forward part of the pathway. Looking at the right side of **Fig. 1.2**, we see that the thalamus receives a projection back from the same section of cortex to which it projected. Further, the number of processes from a projection which is feedback typically drastically outnumbers the amount of feed forward processes (**Fig. 1.3**). Put another way, the number of axon terminals terminating in the thalamus which arise from the cortex drastically outnumber the number of axons which arise from the retina. Similarly, the number of axon terminals which terminate in layer IV of the visual cortex, which are feed forward projections from the LGN, are drastically outnumbered by the number of axon terminals which are either fed back from higher brain centers, or are horizontal feedback projections from other areas of cortex. As a general rule, the number of projections onto a given brain area which are feedback projections appear to always outnumber the feed forward projections (Bullier, 2006).

If we step back from the primary visual pathway in the human, and instead look at the set of projections from the retina to the rest of the brain, which are shared in all amniotes (egg-producing land animals), we see that there are two main radiations: the lemnothalamic and the collothalamic pathways (**Fig. 1.4**).

The primary visual pathway in humans is the lemnothalamic pathway. The collothalamic pathway in humans, and all amniotes, projects to an intermediate nucleus along the path to a part of the thalamus. The intermediate nucleus is in mammals called the superior colliculus (SC), while in birds and reptiles it is called

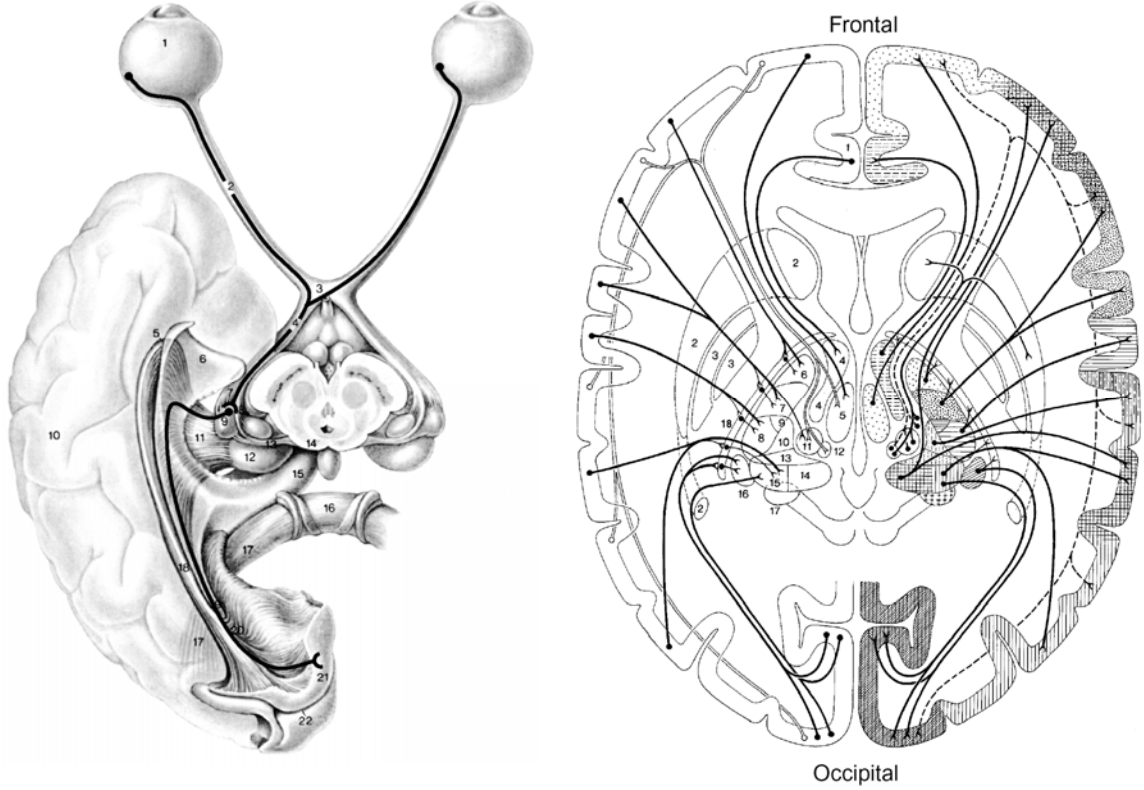

Figure 1.2: LEFT: Ventral view of the primary visual pathway. This pathway proceeds from the retina (1) via the optic nerve (2) to the optic chiasm (3). A subset of the fibers branch off and continue on to the visual sub-section of the thalamus, the lateral geniculate nucleus (9), to the primary visual cortex (21). **RIGHT:** A diagrammatic horizontal section of the human brain showing on the left hemisphere the cortico-thalamic projections and on the right hemisphere the thalamo-cortical projections. Note the ubiquity of feedback throughout the circuitry. (Modified and adapted from Nieuwenhuys et al., 1988.)

the optic tectum (OT). The collothalamic pathway then continues on to a separate section of the dorsal pallium. (Pallium is a very general term referring to an evolutionarily newer section of the amniotic brain which covers the older sections. In mammals, for example, this evolved into the cerebrum and the cortex.) Depending upon the species of amniote, one of these pathways may be much stronger (possess more RGC axons) than the other. For example, in primates and carnivores, the LGN receives far more RGC synapses than the SC. However in reptiles, birds, and a few mammalian species (e.g. the mouse and rabbit) the OT receives far more RGC synapses than the thalamic area (Leamy et al., 2008).

Present in all land animals is an isthmic structure which is reciprocally and topographically connected with the SC/OT (**Fig 1.5**) which does not receive direct retinal input (Butler et al., 2005). This additional structure is also present in amphibians (e.g., frogs) and ray-finned fishes. Oddly, this structure is missing in cartilaginous fishes, indicating that the isthmic structure was not present in the common ancestor to all vertebrates, and thus is an interesting example of parallel evolution.

This isthmic structure (the parabigeminal nucleus (PBN) in mammals or nucleus isthmi (NI) in bird, reptiles, fishes and amphibians) and its relationship to the retino-recipient region with which it connects have been anatomically characterized in a variety of species and it is experimentally accessible *in vivo*, *in vitro*, or both. In addition, in many cases the isthmic structure has been shown to

be isolated from the rest of the brain; that is, the only inputs to the isthmic structure are from the SC/OT. This sets it well apart from the corticothalamic feedback loop, which is highly interconnected with the rest of the surrounding neural architecture and is therefore a non-trivial and complex experimental and

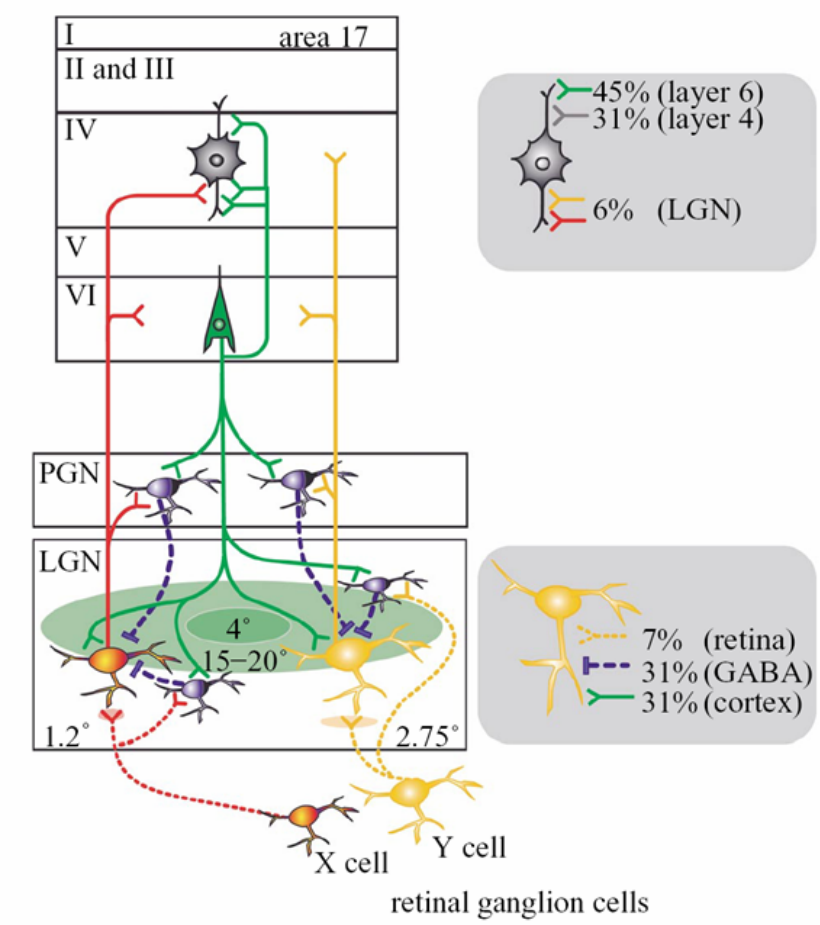

Figure 1.3: Simplified schematic of intrathalamic and cortico-thalamic connections. The top block is the cortex and the bottom block is the visual part of the thalamus. Note the high percentage of feedback in the thalamus compared to the amount of input from the retina. (Modified after Sillito et al., 2003).

theoretical preparation. The accessibility and isolation of the tecto-isthmic system together make it a very attractive feedback loop to study.

The isthmotectal/parabigeminocollicular feedback loop has been studied in a variety of animals. OT/SC neurons project to the ipsilateral NI/PBN which projects back ipsilaterally to the tectum in teleosts (Ito et al., 1982) and birds (Hunt et al., 1977, Wang et al., 2004), or bilaterally in anurans (Gruberg et al., 1978), reptiles (Wang et al., 1983), rats (Linden et al.,1983), cats (Graybiel, 1978), and monkeys (Baizer et al., 1991). In all cases, the NI/PBN displays higher levels of spontaneous activity than the OT/SC. Also, at least a subset of the NI/PBN projection contains a cholinergic feedback to the OT/SC. In some systems there is also a GABAergic component.

In primates and mammals, the PBN is a small nucleus located just caudal ventrally to the SC. Experiments in cats (Sherk, 1979; Cui et al., 2003), rats (Lee et al., 2001) and primates (Sparks, 1986) find that the responses of the PBN are not highly sensitive to specifics of stimulus parameters such as object velocity, size, shape, color, direction of movement. Rather the response appears to be related behaviorally to saccades, the quick eye movements referred to above. The PBN are driven by a subset of SC neurons and project back to the upper layers of the SC where their axon terminals intermingle with a dense collection of excitatory and inhibitory interneurons (Lee et al., 2001). The acetylcholine (ACh) output of the PBN differentially regulates excitatory or inhibitory interneurons. Possibly due to its very small size and awkward location, there have been

comparatively many fewer studies of the PBN and its interactions with the SC than there have been in the NI and its interactions with the OT within the bird, reptile, fish, and amphibian.

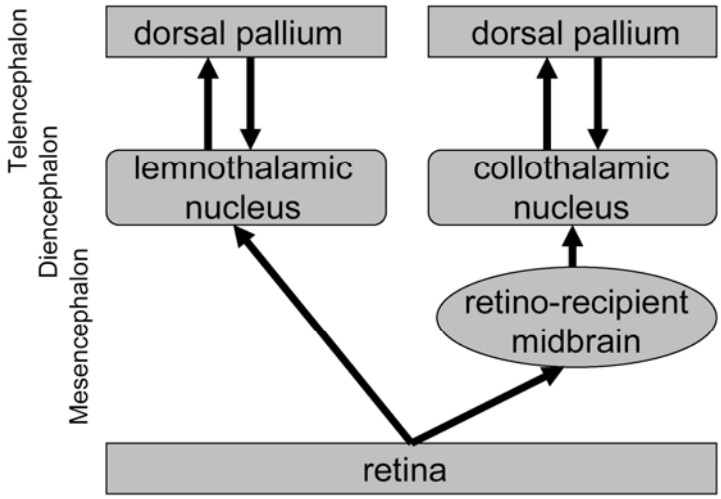

Figure 1.4: A simplified schematic of the lemnothalamic (left) and collothalamic (right) visual pathways from the retina. The superior colliculus (optic tectum) is located within the mesencephalon. The dorsal thalamus is located within the diencephalon. Separate areas of the dorsal pallium within the telencephalon receive inputs from the lemnothalamic and collothalamic regions of the dorsal thalamus. Interactions between the two areas of the dorsal pallium and possible feedback from the dorsal pallium to the retino-recipient midbrain are not shown. (Modified after Ch. 4 in McIlwain 1996.)

The extent of the NI structure depends on the species. In fishes such as teleosts (Williams et al., 1983, Northmore et al., 2003; Gallagher et al., 2005), the NI is a single structure with undifferentiated neurons. The responses of the NI to visual stimuli do not appear to be topographic, though the habituation to repeated stimuli is topographic. Also, the time course of the NI response to visual and

electrical stimuli are longer than the response of the OT, though the cause of this has yet to be elucidated.

In reptiles, the NI is composed of two separate nuclei, a magnocellular nucleus (Imc) composed of large somata and a parvocellular nucleus (Ipc) composed of small cell bodies (Wang et al., 1983; Sereno et al., 1987, George at al., 1999). The Ipc is cholinergic, providing positive feedback, while the Imc is GABAergic, providing a negative feedback loop to the OT. These nuclei also differ in their receptive field sizes and connectivity: The Imc receives a broader input and projects back a broad inhibitory axonal arborization. The Ipc, on the other hand, has a smaller receptive field and projects back to the OT to the same column from which it received a projection. The connectivity is topographic: there is a map of the retina in the OT which is continued in the Ipc and only slightly less so in the Imc. There exits both ipsilateral as well as contralateral isthmo-tectal projections.

Birds have been shown to possess an even greater number of subnuclei within the NI, having not only the Ipc and Imc but also a structure called the Slu and an additional structure called the nBOR which sends feedback directly to the retina (Hellman et al., 2001; Wang et al., 2003). The Slu may receive input from the nucleus pretectalis and so it does not form a closed loop feedback system as do the Ipc and Imc and so will not be discussed further here. The NI has been shown to differentially regulate the receptive fields of OT neurons (Wang, 2003; Marin et al., 2005; Marin et al., 2007), and even coordinate the interplay of

different sensory modalities within the OT of the barn owl (Witten et al., 2006, Maczko et al., 2006). A role of the NI feedback, as realized by the ipsilateral interaction of the positive and negative feedback loops, may be to act as a winner-take-all mechanism by regulating the sensitivities of the OT neurons (Wang 2003; Wang et al., 2005; Maczko et al., 2006; Brandt et al., 2007).

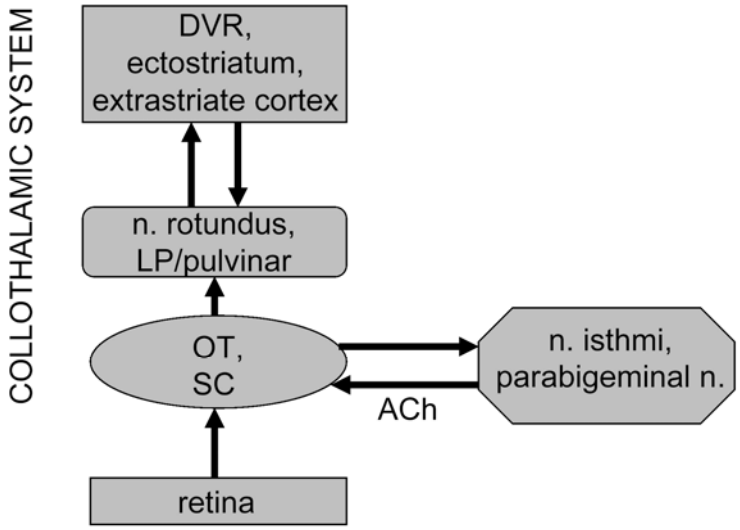

Figure 1.5: A slightly more detailed schematic of the collothalamic visual pathway and its cholinergic modulation in the superior colliculus (optic tectum) via the reciprocally connected parabigeminal nucleus (nucleus isthmi). Listed for clarity are the brain areas for reptiles, birds, and mammals. (Modified after Ch. 4 in McIlwain 1996.)

The case of amphibians is a bit different. While there is only one sub-nucleus to the isthmic structure, as there is in the fishes, the isthmotectal projections are bilateral as in cats, rats, and reptiles (Wiggers, 1998). Also, there are highly conflicting results concerning whether the feedback is inhibitory or excitatory (Wang, 2003). In the salamander, most of the isthmic neurons project

bilaterally (Wiggers, 2003). This is in stark contrast to the frogs where it has been clearly demonstrated that separate collections of isthmic neurons project contralaterally than those which project ipsilaterally (Grobstein et al., 1978; Gruberg et al., 1978; Grobstein et al., 1983; Dudkin et al., 1999; Dudkin et al., 2007). Whether or not these projections arise from physiologically distinct groups of neurons has yet to be fully explained. Due to the differential responses observed in the OT in response to electrical stimulation of the NI and due to the segregation of differently projecting isthmic neurons, it seems natural to hypothesize that there are multiple groups of isthmic neurons, as there are in birds, and that they are clumped close together in the anuran case. The aim of this dissertation is to determine the number of classes of physiological NI neurons and to investigate the time course of the NI response to simple and complex spatiotemporal stimuli.

The general anatomy of the visual system of the frog is shown in **Fig. 1.6**. While there are approximately one million photoreceptors in the frog retina, there are only around half a million RGCs in either retina. The set of RGCs, of which 96% project to the contralateral OT (4% project to the thalamus) have been described as being composed of 4-5 physiologically distinct varieties (Lettvin et al., 1959; Witpaard et al., 1975) based on their responses to visual stimuli. RGC types I and II respond differentially to moving spots (in fact, type II fibers are famous for being the first fibers described as having a highly specific driving stimuli, that is, they are 'fly' detectors! They respond vigorously to small convex

black objects moving haphazardly in the receptive field. If the stimulus is too large, too small, too fast, not moving, or not convex then the response will disappear!). Types III and V have responses which are based on the overall

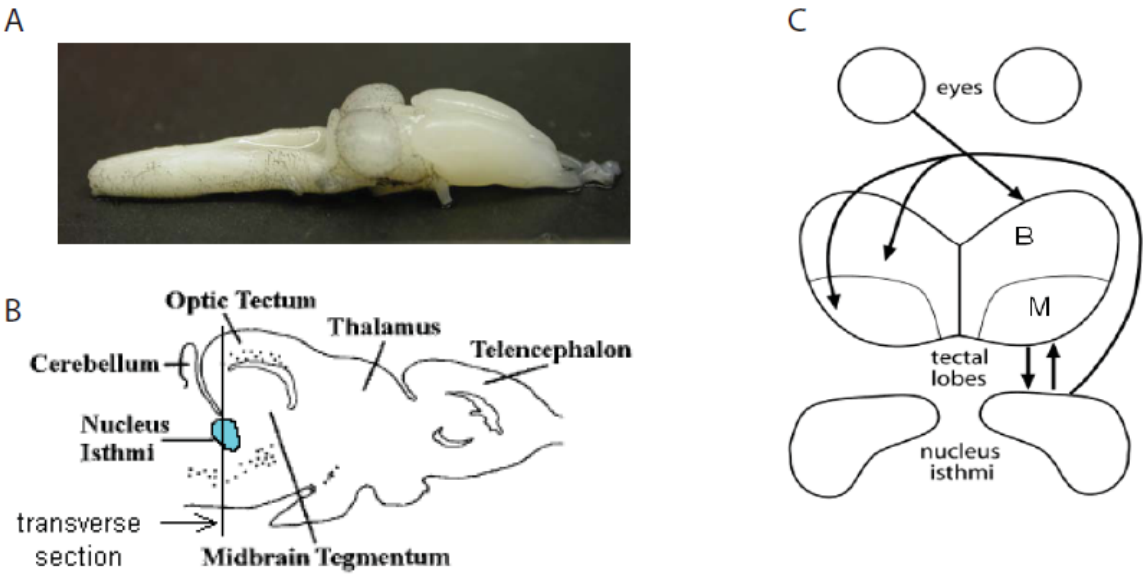

Figure 1.6: General frog (*Rana pipiens*) anatomy. **A.** Whole frog brain. The forebrain, or telencephalon, can be seen to the right. The OT are the two large lobes in the middle. Immediately behind the OT is the cerebellum, and behind that is the hindbrain. **B.** A parasagittal schematic of the frog brain. Note that the NI lies directly below the caudal OT. **C.** A schematic detailing the general connectivity of the visual system. B denotes the area of the OT which responds to stimuli within the bilateral region of the visual field. M denotes the region in the OT which responds to stimuli presented into the monocular visual fields. (B and C are adapted from Winkowski et al., 2005.)

light intensity level; and type IV responds vigorously to a dimming in the light intensity level within its receptive field. This last class is appropriately named the dimming detector. Categorization is further supported by axonal conduction velocities as well as the depth of termination of the axons within the OT (**Fig.**

1.7). Types I and II terminate within the dorsal 50 μm of the OT. Moving ventrally in the superficial OT, there is a lack of RGC axons for approximately 30-50 μm. Following this is a layer of terminating RGC type III and V axon fibers. Below this is another break of around 30-80 μm. Below this is a thick layer of RGC type IV axonal projections. In fact, an electrode can carefully move through the OT in a dorsal-ventral manner and traverse separate sections with clearly different responses. All of the projections from the retina to the OT are topographic. That is, a specific point in visual space corresponds to a specific point on the retina, which in turn corresponds to a specific location on the surface of the OT; this topography is maintained throughout the depth of the OT.

As described above, the OT projects ipsilaterally to the NI. The primary neurons which project to the ipsilateral NI have somata (cell bodies) located mainly in layer 6 of the OT (with a few somata in layers 2, 4, or 8). They are characterized by a narrow dendritic field which ramifies within the superficial layers of the OT, limited to a 50 μm wide column within layer 9 (purple cell in **Fig. 1.7**). These neurons have axons which emanate from the dendritic trunk (as do the Shepherd's crook neurons found within the OT of birds) (Wang et al., 2003; Marin et al, 2005) and leave the OT via the cell free layer 7 of the OT. The axonal fibers travel ventral-caudally to terminate within the NI. Acetylcholine is the neurotransmitter of the tectoisthmic projection. The tectoisthmic projection is also topographic, conserving the point-to-point map which exists within the retina and the OT.

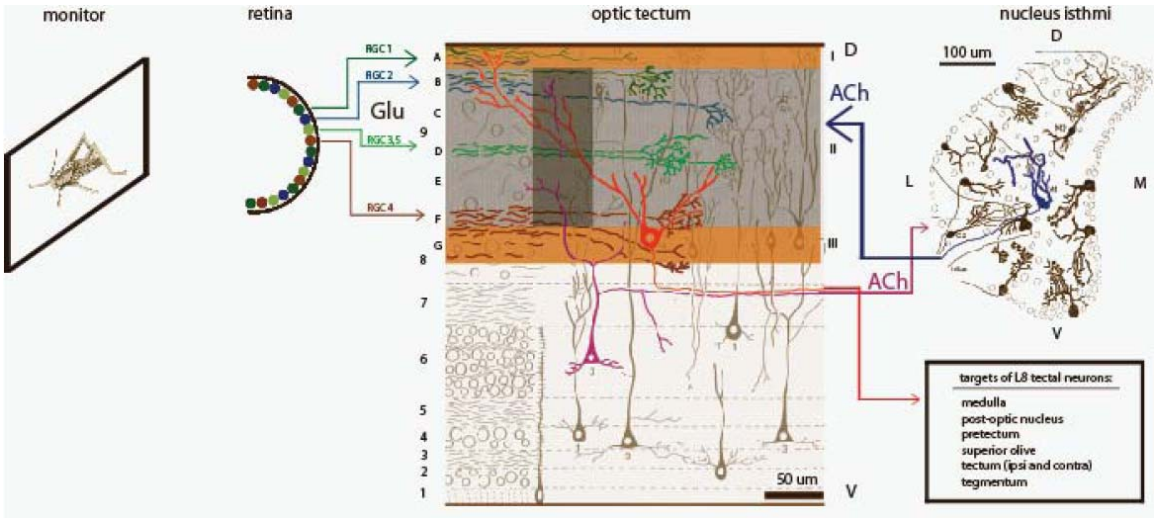

Figure 1.7: General connectivity in the early visual system of *Rana pipiens*. Four physiologically distinct RGC types project to three well separated layers within layer 9 of the superficial optic tectum. RGC I and II terminate in layers 9A and 9B, RGC III and V terminate in layer 9D, and RGC IV terminates in 9F and part of layer G which lies within layer 8. Glutamate (Glu) is the primary neurotransmitter of the RGC axons. Cell bodies within layer 6 of the OT send narrow dendrites up through layer 9 and synapse with collaterals from multiple RGC axon classes. These cells project to the ipsilateral NI using acetylcholine (ACh) as the neurotransmitter. Separate populations within the NI project to the ipsilateral (II) and contralateral (I & III) OT. The ispilateral projection terminates throughout the superficial OT (dark blue box) but does not appear to projecxt as superficially or as deeply as the contralateral projection (orange boxes). The NI uses ACh as its neurotransmitter and is the primary source for ACh within the OT. The OT also contains wide field neurons with cell bodies in layer 8 and dendrites which broadly ramify throughout layer 9. These project axons out of the OT via layer 7 to other areas of the brain. (Adapted and modified from Szekely et al., 1976; Khalil et al., 1977).

As stated above, the projection from the NI back to the OT is bilateral, emanating from separate sets of neurons (Grobstein et al., 1978; Gruberg et al.,

1978; Gruberg et al., 1980; Grobstein et al., 1983; Dudkin et al., 1999; Dudkin et al., 2007). The dorso-rostral part of the NI projects directly back to the ipsilateral OT while the ventro-caudal part of the NI projects, via the optic chiasm, to the contralateral OT. All isthmotectal projections terminate within the superficial OT, but the ipsilateral fibers terminate within layers B through F in layer 9 while the contralateral projection terminates in both the superficial most layers A and B in layer 9 as well as the deepest layer of layer 9, layer G, and slightly down to layer 8. The NI accounts for more than 65% of the non-retinal input into the superficial tectum (Gruberg et al., 1989). The topology is maintained within the projection from the NI to both the ipsilateral and contralateral OT. Within the rostral OT there is a greater amount of feedback from the contralateral NI while in the caudal OT the projection is far greater from the ipsilateral NI (Dudkin et al., 1999). The terminations of the NI axonal projections are not on the same neurons which project to the NI (Gruberg et al., 1994). More about this momentarily.

The nucleus isthmi itself (**Fig. 1.8**) is composed of approximately 8,000 neurons (Gruberg et al., 1978), which have been grouped into five classes based on morphological characteristics after a Golgi staining (Khalil et al., 1977). The morphology of the whole nucleus has been described as having a ‘taco’ shape where the bottom of the taco is the rim cortex (cortex here is used to define an outer cell body dense surrounding area) which projects contralaterally, an anterior non-rim cortex which projects ipsilaterally, and a posterior non-rim cortex

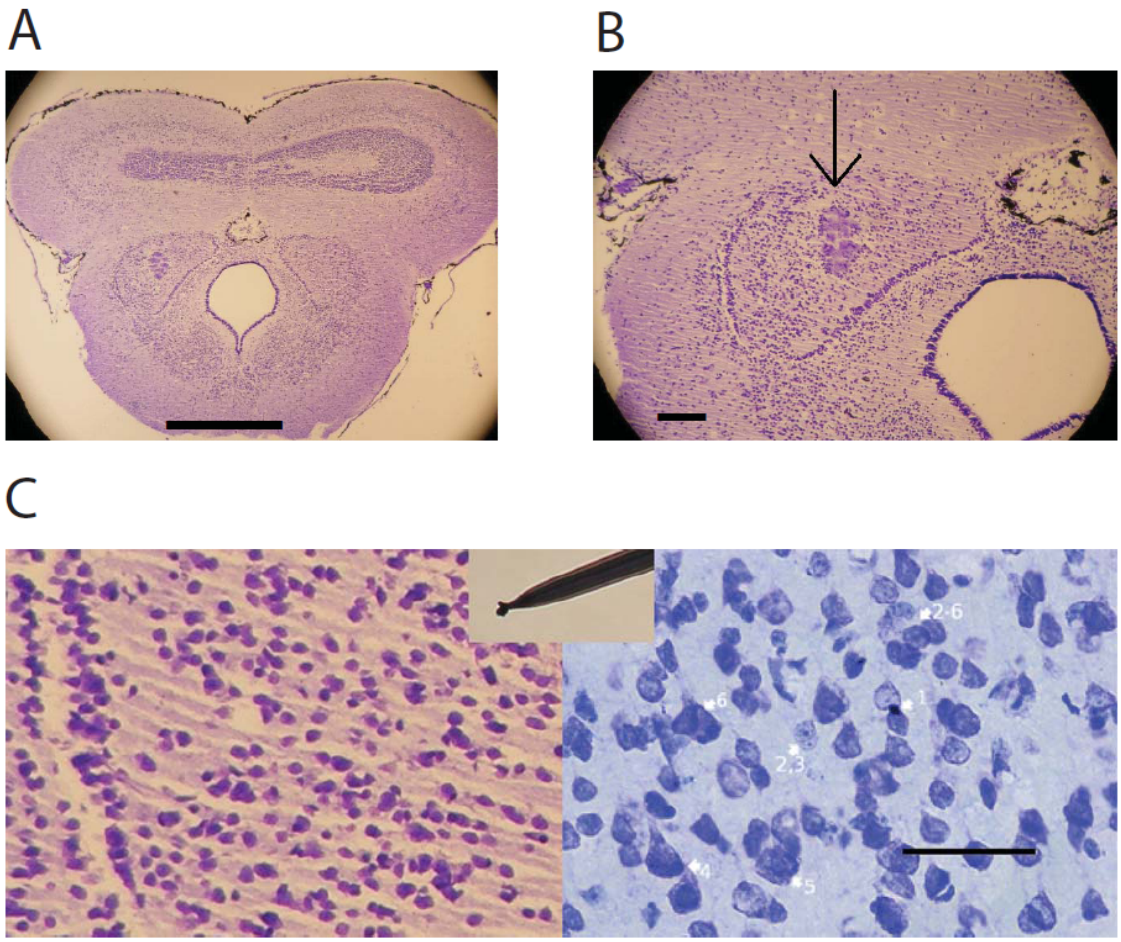

Figure 1.8: Cresyl violet stains of the nucleus isthmi of the frog, Rana pipiens. **(A)** Transverse section as shown schematically in **Fig. 1.6**. Note the layers of the tectum on the dorsal side and the clear outline of the isthmi cortex in the middle of the slice. **(B)** A lesion placed in the middle of the left NI (arrow). **(C) LEFT**: Zoomed image of stain of NI of frog. **RIGHT**: stain of cortical cells in the Rhesus monkey. **CENTER**: an example electrode used for our extracellular recordings. Note plated tip. The NI has densely packed small neurons, posing a challenge for obtaining good signal to noise and for spike sorting algorithms. Scale bars: 1000 μm in (A), 100 μm in (B) and 50 μm in (C).

which projects contralaterally (Grobstein et al., 1983). The caudal region of the NI may also receive inputs from the mesencephalic tegmentum from a small

population (40-45 neurons) of cells (Udin, 1987). There do not appear to be any isthmo-isthmic projections.

Pharmacologically, multiple studies have shown that the NI is the primary, if not the only, source for ACh within the superficial OT (Stevens, 1973; Desan et al., 1987; Sargent et al., 1989; Wallace et al., 1990; Butt et al., 2000; Butt et al., 2001; Yu et al., 2003; Yan et al., 2006). The nicotinic receptors (nAChR) have been found predominantly on presynaptic locations (and, in fact, many are extra-synaptic, up along an axon well before the synaptic site), mainly on RGC axons (Sargent et al., 1989; Titmus et al., 1999), while muscarinic receptors (mAChR) have been found primarily on post synaptic locations within the OT (Butt et al., 2001; Yu et al., 2003). In fact, different types of nAChRs have been shown to be associated with different inputs (Butt et al., 2000), where the nAChRs on the RGC axons have different time courses in their response than other nAChR varieties on other locations which have yet to be fully determined. When the presynaptic nAChRs are activated by ACh there is a higher probability for transmission at the synaptic site (Titmus et al., 1999). Serotonin and substance-P have also been associated with the tecto-isthmic system (Liu, et al., 1995; Malayev et al., 1998; Tu et al., 2000; Debski, 2001) especially in forming and keeping the topographic map from the retina. The maintenance of the topographic map is activity dependent and appears to depend on both the glutamatergic input from the retina as well as the cholinergic input from the NI. While the primary drive of excitatory responses in the OT emanates from the

glutamatergic input from the retina onto both NMDA and non-NMDA glutamate receptors, the modulation of the excitatory drive is controlled by a combination of GABA and ACh (Hickmott et al., 1993).

The presence of GABA in the tectoisthmic system is at present highly controversial. Nearly one third of the whole of tectal neurons are GABA immunoreactive (Antal, 1991). These include a large number of not only axodendritic synapses but also dendrodendritic synapses within the superficial layers of the OT as well as deeper layers. One paper (Pollak et al., 1999) shows that in a close cousin to *Rana pipiens*, *Rana esculenta*, 0.5% of NI neurons stain positive for immunoreactivity. These cell bodies all lay within the anterior non-rim cortex. They also show that the majority of GABAergic axons within the NI arise from elsewhere, probably the tegmentum. It should be noted, however, that in *Rana esculenta*, there have also been reported reciprocal connections between the NI and the superior olive (an auditory structure) (Kulik et al., 1997). Never have I been in the NI of *Rana pipiens* and recorded auditory responses. When leaving lesions in places I did record auditory responses, the lesions were always observed to be outside of the borders of the NI (data not shown). Using double labeling procedures, it was found (Li et al., 2001) that part of the retinal-tectal projection (about 15%) is GABAergic, and that 65% of the ipsilaterally projecting and 62% of the contralaterally projecting NI cells bodies stain positive for GABA. Yet, they claim that only 50% of those neurons labeled in the NI as GABAergic actually project to the OT. They pose the possibilities that the untraceable

neurons went to an inaccessible part of the OT or that the GABAergic NI neurons are actually interneurons within the NI and do not project out of the nucleus. Intra-NI projections are seen in other systems, like the bird (Marin et al., 2005), which are GABAergic. But, as of yet, there is only circumstantial evidence supporting these findings. Another paper (Rybicka et al., 2005) has shown that many isthmotectal fibers terminate on GABAergic interneurons within the OT. The only other direct connection they found was with a few retino-tectal axons. They did not find evidence for GABA within the axons of the isthmotectal axons.

It has been demonstrated that electrical stimulation of the NI can enhance calcium influx by the RGC axons when the NI stimulation precedes the RGC stimulation by 10 ms (Dudkin et al., 1998; Dudkin et al., 2003). This increase in calcium directly increases the likelihood for transmission at the retino-tectal synapse. As stated above, many nAChRs are extrasynaptic on RGC axons. Thus, the feedback from the NI may enhance the RGC signal into the OT via a paracrine mechanism (Titmus et al., 1999; Dudkin et al., 2003; Rybicka et al., 2005).

Experiments using electrical stimuli and ionotophoretic application of neurotransmitter agonists or antagonists have determined that there are at least five types of synaptic connections between the isthmotectal fibers and the dendrites of tectal neurons (Antal et al., 1986; Xiao et al., 1999; Wang, 2003; Hoshino et al., 2006). These results also show that many interactions between the isthmic neurons and the tectal responses are multisynaptic. Complicating the

matter, ACh has been shown to have either an excitatory or an inhibitory affect on the postsynaptic neuron (Lawrence, 2008). Thus, a paracrine puff of ACh from an axonal terminal of a NI afferent may lead to differential responses in different units within the superficial NI.

In response to visual stimuli, extracellularly recorded NI neurons have been broken into two broad classes (Gruberg et al., 1980). One group has a small 3-5º sized receptive field and response similarly to RGC type II neurons. The other group has larger receptive fields, around 7-10º in diameter, and these units respond not only to moving dots but also to diffuse illumination changes. The NI responds to motion in both the ipsilateral and contralateral receptive field (Gruberg et al., 1980; Beauquin et al., 1995; Winkowski et al; 2005). The literature, however, does not comment on the time course of the response within the NI.

Behaviorally, if a NI is lesioned, frogs suffer from a scotoma, or functional blind spot, in the visual field contralateral to the lesion (Gruberg et al., 1991). No matter how much of the NI is lesioned, the scotoma always extends back to the temporal most aspect of the contralateral visual field. The more NI is lesioned, the more of the nasal area of the visual field that the scotoma affects. If an entire NI is lesioned, then the scotoma extends through the entire contralateral hemifield of the visual field. Interestingly, this scotoma only affects the responses to moving stimuli of either predator- (large) or prey- (small) type. The frog is, in fact, capable of jumping through transparent barriers in its visual field if

the entire OT has been removed (and then the NI feedback is a non-issue anyway) (Saltzman et al., 2004). Also, the behavioral responses of the frog are highly asymmetric. If presented with two identical stimuli placed at different locations within the visual field, the frog will choose the most nasal and ground level stimuli (Gruberg, personal communication). It is not yet known from where this asymmetry arises in the connectivity of the tectoisthmic system.

It seems that the vast majority of RGC axons which project to the contralateral OT are only used to drive responses which are important for moving stimuli. That is, it is important for eating food (a frog will not attack a dead cricket, it must be moving) and evading predators. The frog does not use its sight when finding a mate (Gruberg, personal communication). The remaining 4% of RGC axons which terminate in the thalamus are responsible for non-moving aspects of the visual world.

Relating the NI of the frog to its homologues in other systems, it is natural to wonder if the NI is in fact working as a winner-take-all mechanism in the visual system of the frog. Are the connections back to the RGC axons creating a 'spotlight of attention' onto the most salient input presented? How are populations of NI neurons responding to the visual inputs? Are there oscillations in the responses within the tecto-isthmic system as there are in the thalamocortical system (Bal et al., 2000)? Due to the very strong collothalamic projection in the frog compared to the lemnothalamic projection, does the collothalamic projection do many of the same things which the lemnothalamic

projection is thought to do (attention (Reynolds, 2008), oscillatory control (Bal et al., 2000; Schnitzer et al., 2005), winner-take-all (Lee et al., 1999), stimulus response precision (Andolina et al., 2007), analogy (Choe, 2004))?

As a first step in answering these questions, this dissertation is focused on characterizing the temporal aspects of the NI response in the frog to visual stimuli and in determining how many physiological classes of neurons exist within the NI. **Chapter 2** discusses a novel threshold I developed to detect low signal-to-noise spikes within an extracellular voltage recording and how I sort them into separate putative units. This enables us to analyze the responses of multiple units recorded simultaneously to a given visual stimuli. **Chapter 3** discusses the responses of NI neurons to simple stimuli, e.g., diffuse illumination or moving spots. **Chapter 4** discusses the responses within the NI to contextual stimuli, or stimuli with multiple parts. This chapter was highly motivated by Marin's et al. 2005 and 2007 papers on the NI of the bird. **Chapter 5** discusses the number of subclasses of NI neuron within the frog, *Rana pipiens,* based on my data of extracellularly recorded responses to visual stimuli and Matt Caudill's data on intracellular responses measured *in vitro*. **Chapter 6** will provide a conclusion and a set of future directions and questions for this project.

REFERENCES:

Andolina IM, Jones HE, Wane W, Sillito AM. Coritcothalamic feedback enhances stimulus response precision in the visual system. *PNAS*. 2007. **104**: 1685-1690.

Antal M, Matsumoto N, Szekely G. Tectal neurons of the frog: intracellular recordings and labeling with cobalt electrodes. *J Comp. Neurology*. 1986. **246**: 238-253.

Antal M. Distribution of GABA immunoreactivity in the optic tectum of the frog: a light and electron microscopic study. *Neuroscience.* 1991. **42**: 879-891.

Baizer JS, Whitney JF, Bender DB. Bilateral projections from the parabigeminal nucleus to the superior colliculus in monkey. *Exp Brain Res*. 1991. **86**: 467-470.

Bal T, Debay D, Destexhe A. Cortical feedback controls the frequency and synchrony of oscillations in the visual thalamus. *J. Neurosci*. 2000. **20**: 7478-7488.

Beauquin C, Poindessault JP, Gaillard F. Reponses of ipsilateral retino-tectal (type I1) units of the frog (*Rana esculenta*) to moving configurational bars. *Comp. Biochem. Physiol.* 1995. **111**: 561-568.

Brandt SF, Wessel R. Winner-take-all selection in a neural system with delayed feedback. *Biol Cybern*. 2007. **97**: 221-228.

Bullier J. What is fed back? In: *23 Problems in Systems Neuroscience*. Ed: Van Hemmen JL, Sejnowski TJ. Oxford University Press. pp.103-132. 2006.

Butler AB, Hodos W. *Comparative Vertebrate Neuroanatomy: Evolution and Adaptation*. Wiley. 2005.

Butt CM, Pauly JR, Debski EA. Distribution and development of nicotinic acetylcholine receptor subtypes in the optic tectum of *Rana pipiens*. *J. Compar. Neurol*. 2000. **423**: 603-618.

Butt CM, Pauly JR, Wilkins LH, Dwoskin LP, Debski EA. Pharmachology, distribution and development of muscarinic acetylcholine receptor subtypes in the optic tectum of *Rana pipiens*. *Neuroscience*. 2001. **104**: 161-179.

Choe Y. The role of temporal parameters in a thalamocortical model of analogy. *IEEE Transactions on Neural Networks*. 2004. **15**:1071-1082.

Cui H, Malpeli JG. Activity in the parabigeminal nucleus during eye movements directed at moving and stationary targets. *J. Neurophysiol*. 2003. **89**: 3128-3142.

Debski EA. Distribution and regulation of Substance-P related peptide in the frog visual system. *Microscopy Res. and Tech*. 2001. **54**: 220-228.

Desan PH, Gruberg ER, Grewell KM, Eckenstein F. Cholinergic innervations of the optic tectum in the frog *Rana pipiens*. *Brain Research*. 1987. **413**: 344-349.

Dudkin EA, Myers PZ, Ramirez-Latorre JA, Gruberg ER. Calcium signals monitored from leopard frog optic tectum after the optic nerve has been selectively loaded with calcium sensitive dye. *Neurosci. Lett.* 1998. **258**: 124-126.

Dudkin ES, Gruberg ER. Relative number of cells projecting from contralateral and ipsilateral nucleus isthmi to loci in the optic tectum is dependent on visuotopic location: horseradish peroxidase study in the leopard frog. *J. Comp. Neurol*. 1999. **414**: 212-216.

Dudkin EA, Gruberg ER. Nucleus isthmi enhances calcium influx into optic nerve fiber terminals in *Rana pipiens*. *Brain Research*. 2003. **969**: 44-52.

Dudkin EA, Sheffield JB, Gruberg ER. Combining visual information from the two eyes: the relationship between isthmotectal cells that project to ipsilateral and to contralateral optic tectum using fluorescent retrograde labels in the frog, *Rana pipiens*. *J. Comp. Neurol*. 2007. **502**: 38-54.

Gallagher SP, Northmore DPM. Responses of the teleostean nucleus isthmi to looming objects and other moving stimuli. *Vis. Neurosci*. 2006. **23**: 209-219.

George SA, WU GY, Li WC, Wang SR. Dual actions of isthmic input to tectal neurons in a reptile, *Gekko gekko*. *Vis. Neurosci*. 1999. **16**: 889-893.

Graybiel AM. A satellite system of the superior colliculus: the parabigeminal nucleus and its projections to the superficial collicular layers. *Brain Res*. 1978. **145**: 365-374.

Grobstein P, Comer C, Hollyday M, Archer SM. A crossed isthmo-tectal projection in *Rana pipiens* and its involvement in the ipsilateral visuotectal projection. *Brain Research.* 1978. **156**: 117-123.

Grobstein P, Comer C. The nucleus isthmi as an intertectal relay for the ipsilateral oculotectal projection in the frog, *Rana pipiens*. *J. Compar. Neurol*. 1983. **217**: 54-74.

Gruberg ER, Udin SB. Topographic projections between the nucleus isthmi and the tectum of the frog, *Rana pipiens*. *J Compar. Neurol.* 1978. **179**: 487-500.

Gruberg ER, Lettvin JY. Anatomy and physiology of a binocular system in the frog *Rana Pipiens*. *Brain Research.* 1980. **192**: 313-325.

Gruberg ER, Wallace MT, Waldeck RF. Relationship between isthmotectal fibers and other tectopetal systems in the leopard frog. *J Compar. Neurol*. 1989. **288**: 39-50.

Gruberg ER, Wallace MT, Caine HS, Mote MI. Behavioral and physiological consequences of unilateral ablation of the nucleus isthmi in the leopard frog. *Brain Behav Evol*. 1991. **37**: 92-103.

Gruberg ER, Hughes TE, Karten HJ. Synaptic interrelationships between the optic tectum and the ipsilateral nucleus isthmi in *Rana pipiens*. *J. Comp. Neurol*. 1994. **339**: 353-364.

Hellman B, Manns M, Gunturkun O. Nucleus isthmi, pars semilunaris as a key component of the tectofugal visual system in pigeons. *J Comp Neurol.* 2001. **436**: 153-166.

Hickmott PW, Constantine-Paton M. The contributions of NMDA, non-NMDA, and GABA receptors to post-synaptic responses in neurons of the optic tectum. *J. Neurosci*. 1993. **13**: 4339-4353.

Hoshino N, Tsurudome K, Nakagawa H, Matsumoto N. Current source density analysis of contra- and ipsilateral isthmotectal connections in the frog. *Vis Neurosci*. 2006. **23**: 713-719.

Hunt SP, Streit H, Kunzel H, Cuenod M. Characterization of the pigeon isthmotectal pathway by selective uptake and retrograde movement of radioactive compounds and by golgi-like horseradish peroxidase labeling. *Brain Res.* 1977. **129**: 197-212.

Ito H., Sakamoto N, Takatsuji K. Cytoarchitecture, fiber connections, and ultrastructure of nucleus isthmi in a teleost (*Navadon modestus*) with a special reference to degenerating isthmic afferents from optic tectum and nucleus pretectalis. *J Comp Neurol.* 1983. **218**: 270-281.

Khalil SH, Lazar G. Nucleus isthmi of the frog: structure and tecto-isthmic projection. *Acta. Morphol. Acad. Sci. Hung*. 1977. **25**: 51-59.

Khanbabaie R, Mahani AS, Wessel R. Contextual interaction of GABAergic circuitry with dynamic synapses. *J. Neurophysiol.* 2007. **97**: 2802-2811.

Lawrence JJ. Cholinergic control of GABA release: emerging parallels between neocortex and hippocampus. *Trends in Neurosci*. 2008. **7**: 317-327.

Leamy CA, Protti DA, Dreher B. Comparative survey of the mammalian visual system with reference to the mouse. In Eye, Retina, and Visual System of the Mouse. Ed. By Chalupa LM, Williams, RW. MIT Press. Cambridge MA. 2008.. pp. 35-60.

Lee DK, Itti L, Kock C. Braun J. Attention activates winner-take-all competition among visual filters. *Nature*. 1999. **2**: 375-381.

Lee PH, Schmidt M, Hall WC. Excitatory and inhibitory circuitry in the superficial gray layer of the superior colliculus. *J Neuro*. 2001. **21**: 8145-8153.

Lettvin JY, Maturana HR, McCulloch WS, Pitts WH. What the frog's eye tells the frog's brain. *Proceedings of the IRE*. 1959. **47**: 233-258.

Li Z, Fite KV. GABAergic visual pathways in the frog, *Rana pipiens*. *Vis. Neurosci*. 2001. **18**:457-464.

Linden R, Perry VH. Retrograde and anterograde transneuronal degeneration in the parabigeminal nucleus following tectal lesions in developing rats. *J Comp Neurol*. 1983. **218**: 270-281.

Liu Q, Debski EA. Origins of serotonin-like immunoreactivity in the optic tectum of *Rana pipiens*. *J. Compar. Neurol*. 1995. **352**: 280-296.

Maczko KA, Knudsen PF, Knudsen EI. Auditory and visual space maps in the cholinergic nucleus isthmi pars parvocellularis of the barn owl. *J. Neurosci*. 2006. **26**: 12799-12806.

Malayev AA, Debski EA. Serotonin modulates induced synaptic activity in the optic tectum of the frog. *Brain Res.* 1998. **781**: 167-181.

Marin G, Mpodozis J, Sentis E, Ossandon T, Letelier JC. Oscillatory bursts in the optic tectum of birds represent re-entrant signals from the nucleus isthmi pars parvocellularis. *J Neurosci*. 2005. **25**: 7081-7089.

Marin G, Salas C, Sentis E, Rojas X, Letelier JC, Mpodozis J. A cholinergic gating mechanism controlled by competitive interactions in the optic tectum of the pigeon. *J Neurosci.* 2007. **27**: 8112-8121.

McIlwain JT. An introduction to the biology of vision. Cambridge University Press. 1996.

Nieuwenhuys, R., Voogd, J., & van Huijzen, C. The Human Central Nervous System. Berlin . 1988. Heidelberg: Springer-Verlag.

Northmore DPM, Gallagher SP. Functional relationship between nucleus isthmi and tectum in teleosts: synchrony but no topography. *Vis. Neurosci.* 2003. **20**: 335-348.

Pollak E, Lazar G, Gabriel R, Wang SR. Localization and source of GABA aminobutyric acid immunoreactivity in the isthmic nucleus of the frog *Rana esculenta*. *Brain Res. Bull.* 1999. **48**: 343-350.

Reynolds JR. Mapping the microcircuitry of attention. *Nature Neurosci*. 2008. **11**: 861-862.

Rybicka KK, Udin SB. Connections of contralaterally projecting isthmotectal axons and GABA-immunoreactive neurons in *Xenopus* tectum: an ultrastructural study. *Vis. Neurosci*. 2005. **22**: 305-315.

Saltzman H, Zacharatos M, Gruberg ER. Recognition of apertures in overhead transparent barriers by leopard frogs. *Brain Behav. Evol*. 2004. **64**: 11-18.

Sargent PB, Pike SH, Nadel DB, Lindstrom JM. Nicotinic acetylcholine receptor-like molecules in the retina, retinotectal pathway, and optic tectum of the frog. *J. Neurosci*. 1989. **9**: 565-573.

Sereno MI, Ulinski PS. Caudal topographic nucleus isthmi and the rostral nontopographic nucleus isthmi in the turtle, *Pseudemys scripta. J. Comp. Neurol*. 1987. **261**: 319-346.

Shephard GM. The synaptic organization of the brain. Oxford. Oxford University Press. 2004.

Sherk H. A comparison of visual-response properties in cat's parabigeminal nucleus and superior colliculus. *J. Neurphysiol*. 1979. **42**: 1640-1655.

Sillito AM, Cudiero J, Jones HE. Always returning: feedback and sensory processing in visual cortex and thalamus. *Trends in Neuroscience*. 2006. **29**: 307-316.

Sparks D. Translation of sensory signals into commands for control of saccadic eye movements: role of primate superior colliculus. *Physiol. Revs*. 1986. **66**: 118-171.

Stevens RJ. A cholinergic inhibitory system in the frog optic tectum: its role in visual electrical responses and feeding behavior. *Brain Res*. 1973. **49**: 309-321.

Szekely G, Lazar G. Cellular and synaptic architecture of the optic tectum. In *Frog Neurobiology.* Ed. Llinas R, Precht W. 1976. Springer. Verlag, Berlin. Pp. 407-434.

Titmus MJ, Tsai HJ, Lima R, Udin SB. Effects of choline and other nicotinic agonists on the tectum of juvenile and adult *Xenopus* frogs: a patch-clamp study. *Neuroscience*. 1999. **91**: 753-769.

Tu S, Butt CM, Pauly JR, Debski EA. Activity-dependent regulation of Substance-P expression topographic map maintenance by a cholinergic pathway. *J. Neurosci*. 2000. **20**: 5346-5357.

Udin SB. A projection from the mesencephalic tegmentum to the nucleus isthmi in the frogs *Rana pipiens* and *Acris crepitans*. *Neuroscience*. 1987. **21**: 631-637.

Wallace MT, Ricciuti AJ, Gruberg ER. Nucleus isthmi: its contribution to Tectal acetylcholinesterase and choline acetyltransferase in the frog *Rana pipiens*. *Neuroscience*. 1990. **35**: 627-636.

Wang SR, Yan K, Wang YT, Jiang SY, Wang XS. Neuroanatomy and electrophysiology of the lacertilian nucleus isthmi. *Brain Research*. 1983. **275**: 355-360.

Wang SR. The nucleus isthmi and dual modulation of the receptive field of tectal neurons in non-mammals. *Brain Res. Rev*. 2003. **41**: 13-25.

Wang Y, Major DE, Karten HJ. Morphology and connections of nucleus isthmi pars magnocellularis in chicks (*Gallus gallus*). *J Comp. Neurol*. 2004. **469**: 275-297.

Wang Y, Luksch H, Brecha NC, Karten HJ. Columnar projections from the cholinergic nucleus isthmi to the optic tectum in chicks (*Gallus gallus*): a possible substrate for synchronizing tectal channels. *J Comp. Neurol*. 2005. **494**: 7-35.

Wiggers W. Isthmotectal connections in plethodontid salamanders. *J. Comp. Neurol*. 1998. **395**: 261-272.

Williams B, Hernandez N, Vanegas H. Electrophysiological analysis of the teleostean nucleus isthmi and its relationships with the optic tectum. *J. Comp. Physiol*. 1983. **152**: 545-554.

Winkowski DE, Gruberg ER. Superimposed maps of the monocular visual fields in the caudolateral optic tectum in the frog, Rana pipiens. *Vis. NeuroSci.* 2005**.** **22:** 101-109.

Witpaard H, ter Keurs HEDJ. A reclassification of retinal ganglion cells in the frog based on tectal endings and response properties. *Vis. Res*. 1975. **15**: 1333-1338.

Witten IB, Bergan JF, Knudsen EI. Dynamic shifts in the owl's auditory space map predict moving sound location. *Nature Neuroscience*. 2006. **9**: 1339-1445.

Xiao J, Wang Y, Wang SR. Effects of glutamatergic, cholinergic and GABAergic antagonists on Tectal cells in toads. *Neuroscience*. 1999. **90**: 1061-1067.

Yan X, Zhao B, Butt CM, Debski EA. Nicotine exposure refines visual map topography through an NDMA receptor-mediated pathway. *Euro. J. Neurosci.* 2006. **24**: 3026-3042.

Yu CJ, Debski EA. The effects of nicotinic and muscarinic receptor activation on patch-clamped cells in the optic tectum of *Rana pipiens*. *Neuroscience*. 2003. **18**: 135-144.

Chapter 2:

ON SPIKE SORTING WITH A NOVEL THRESHOLD AND SUPERPARAMAGNETIC CLUSTERING

ABSTRACT:

I will describe a complete unsupervised method for detecting and sorting spikes within a neural recording. The method utilizes a novel empirically derived threshold for detecting the spikes and uses the noise characteristics of the recording site to optimize the clustering procedure. The method uses the coefficients from a multi-resolution wavelet decomposition, which localizes the relevant characteristics of the spike, to characterize each unitary potential. Then a superparamagnetic clustering algorithm outputs not only the cluster memberships but also the total number of clusters present within the data. Due to the combination of the empirically derived threshold, optimization procedure, and the wavelet decomposition this method is highly robust even within a low signal-to-noise environment. Its speed allows for early implementation while searching for an ideal location to record. The threshold described will be compared to other common thresholds.

INTRODUCTION:

Understanding how brains process information requires a multi-leveled analysis of brain activity: from the workings of proteins up through the activity of systems of neurons and nuclei and how this symphony of activity correlates with behavior. Extracellular recording from neural tissue is a powerful and important tool in elucidating neural activity at the single neuron and neural systems levels. Often the recording electrode is placed at a location within neural tissue containing multiple units which are responding to a given stimulus. The true power of extracellular recordings can thus only be fully realized if the set of action potentials detected by the recording electrode(s) can be sorted into a set of putative neurons, or units, with individual physiological response characteristics.

An extracellular electrode with an impedance between 50 - 500 kΩ at 1 kHz can pick up signals from as far away as 80 μm (circle in **Fig. 2.1**) (Quiroga et al., 2009). Within that volume there may be multiple units responding to the stimuli, spontaneously firing, or contributing to some other internal or uncontrolled neural process. Some units are close enough to the electrode that their spike shape is well above the noise level (colored units in **Fig. 2.1**). Without sorting the recorded spikes into clusters and correlating those spike trains with the stimuli, the information gained from the recording is incomplete and can be misleading.

The necessary steps in any spike sorting procedure are as follows: (1) detection of spikes, (2) obtaining the relevant distinctive features of the individual spike shapes, and (3) clustering these features into a set of putative neurons.

Each phase of this procedure contains subtleties which can be highly affected by the signal-to-noise ratio (SNR) of the recording.

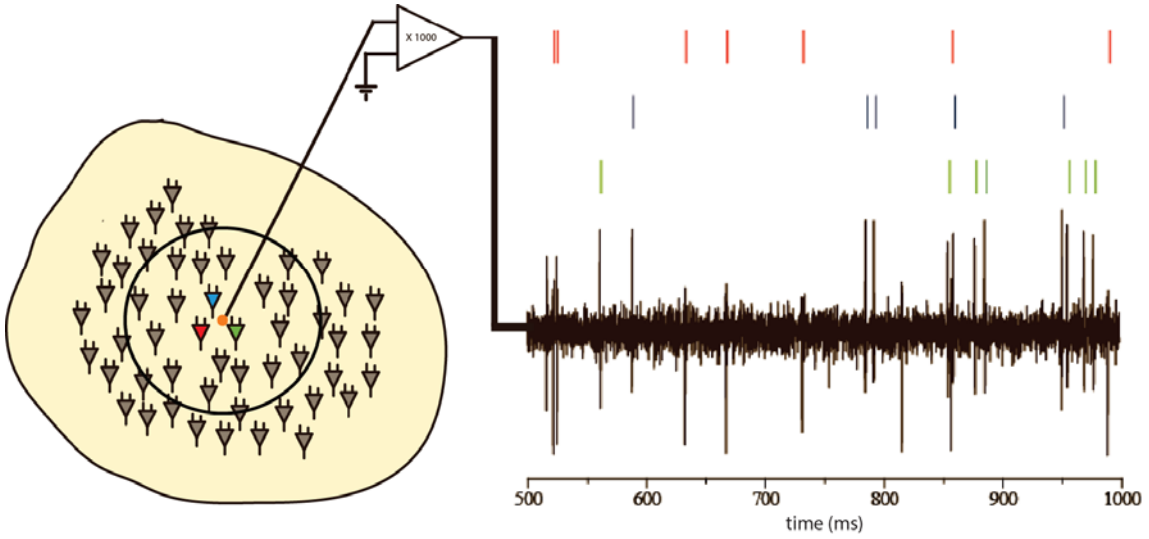

Figure 2.1: Extracellular recording within neural tissue. On the left is a schematic of neural tissue with distant units contributing to inseparable noise (grey) and closer units contributing to large SNR spikes (colored units). The plated extracellular electrode can detect signals up to around 80 μm away from the tip (black circle). The signal is amplified and high-pass filtered to reveal a multi-unit signal. With proper spike-sorting procedures the spike shapes can be sorted and multiple raster plots can be constructed from a single recording.

Typically, the detection phase is accomplished by a threshold in the voltage or derivative of the voltage (Meister et al., 1994; Lewicki, 1998; Kim et al., 2000; Pouzat et al., 2002; Quiroga et al., 2004; Marin et al., 2005; Mtetwa et al., 2006). If one is merely interested in recording from only units with the maximal SNR value and this value is very high (say, greater than 5) then this poses no great problem. However, in a typical extracellular recording there may be more units which are closer to the noise level which may be of use to the experimenter,

especially if one is interested in correlations of activity throughout the local neuronal population.

The set of distinctive features of the spike shapes which are necessary for spike sorting is also highly dependent upon the noise level. With a high SNR one may use a reduced set of characteristics such as the amplitude and width of the spike (Meister, Pine, Baylor, 1994; for example), but with a larger relative contribution to the spike shape by noise, these features may prove to be insufficient to properly describe the spike shape. The clustering method itself poses a very difficult problem as this is a fully unsupervised situation where one never truly knows how many putative units are contributing to the recording (**Fig. 2.1**) nor does one know each unit's extracellular spike profile (Brown et al., 2004). A low SNR environment invariably adds lots of noise to the clusters within the parameter space making most clustering methods nearly untenable.

In this chapter, I describe a completely automated method for spike sorting which is robust down through a low SNR level. This algorithm uses the data itself to obtain an ideal threshold for spike detection by taking into account the distribution of voltage values within the recording. It then uses the noise itself to optimize the feature extraction as well as the clustering procedure. The algorithm utilizes wavelets as the distinctive characteristics. Wavelet coefficients localize the most relevant features of the spike shapes, such as high frequency peaks and valleys, as well as low frequency after-hyperpolarizations, and are less sensitive to noise than other characteristic measures such as reduced

feature spaces or the recorded spike shape itself. The algorithm uses a superparamagnetic clustering method which is fast and quite robust down to a low SNR level. I will describe in detail each step in the algorithm with accompanying mathematical background where necessary. I will then test the novel threshold with artificial data sets with varying SNR and compare its performance with other commonly used methods. This procedure works well with single electrodes, but is easily extended for work with multiple electrodes (Gray et al., 1995; Du et al., 2009). In fact, the more information is available, the better the sorting can become (Pouzat et al., 2002).

METHODS:

Proper spike sorting must take into account three separate issues: (I) detection, (II) acquiring distinctive features of the spikes, and (III) sorting the spike shapes using some clustering method which takes into account these features (**Fig. 2.2**).

Following the works of others (Meister et al., 1994; Lewicki, 1998; Sahani et al., 1997; and Pouzat et al., 2002) I incorporate four working assumptions:

1. The spike shapes of a given neuron, or unit, are constant,
2. The spikes and the surrounding noise are statistically independent,
3. The spikes and the noise sum linearly,

4. The noise statistics tend to a Gaussian distribution as recording time approaches infinity.

The first assumption we know to be not absolutely true, as many neuron's spike shapes change during a burst, for example, but it is an important assumption for any spike sorting routine. The assumption is useful as long as the variance in spike shape from one unit is smaller than the variance in average spike shape between different units. The second and third assumptions are also very common in all spike sorting routines. The fourth assumption is supported by the central-limit theorem, and though no recording goes on for an infinitely long time, I will show that this is a reasonable assumption.

Data Generation:

Once a spike is detected (see below) a 64-point vector is constructed of the voltages that make up the spike shape with an offset so the peak in the slope of the spike occurs in sample number 20. The spikes are aligned in this way, rather than lining them up to the peak in the voltage itself because the initial voltage deflection in a spike shape typically has the steepest slope and is the most salient feature in a spike shape. The magnitude of the voltage is more prone to being offset by the noise. Also, if the spike shape is tri-phasic then sometimes the first peak will be larger and other times the second peak will be larger. This can lead to severe problems in clustering the spike shapes due to

poor alignments. The vector points to a location in a 64-dimensional event space.

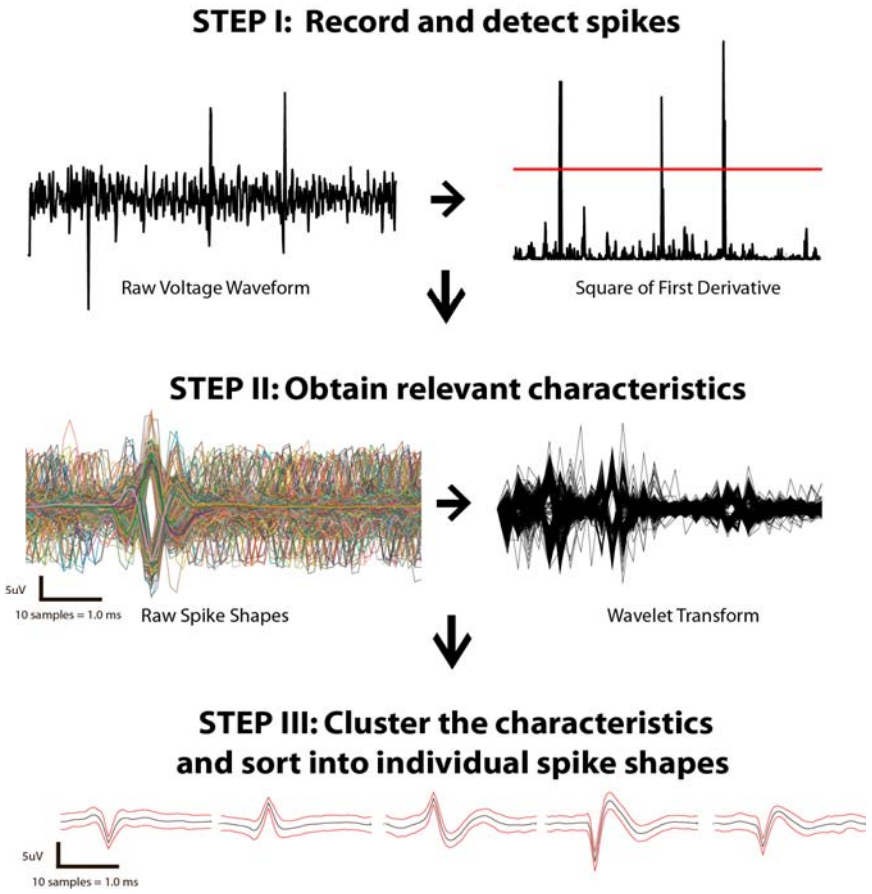

Figure 2.2: Outline of the three stages of spike sorting**.** Step one incorporates obtaining the voltage waveform and high-pass filtering of the signal if necessary. Then a threshold is determined by the data itself and applied to the square of the first derivative (red line). In step two, the spike shapes are extracted from the data and a wavelet transform is performed on the spike shapes to obtain an ideal set of characteristics for clustering. Last, in step three, the sets of wavelet coefficients are clustered using a superparamagnetic clustering algorithm and the shapes are segregated into distinct sets corresponding to putative units within the neural tissue.

If assumption (1) above is correct, and there is no noise in the recording, then all spikes from a given putative neuron point to the same exact point in the event space. In fact, assumption (1) above does not hold when a unit fires many spikes in a short burst. When this happens, the spike shapes produced trace out a line or a manifold in the 64-dimensional parameter space. The main point here is that the variance among the spike shapes arising from a given unit is assumed to be much smaller than the difference between the spike shape from this given unit and a spike shape from another unit within range of the recording electrode. However, due to noise, the spike vectors from a given unit will point to a cloud whose covariance mirrors that of the underlying noise plus the covariance given by the manifold traced out by the collection of noiseless spikes.

The signal to noise ratio (snr) is of a single detected spike is herein defined as:

$$snr = \frac{P_{SPIKE}}{P_{NOISE}} \equiv \frac{\frac{1}{N_{SPIKE}} \sum_i \left(x_i - \mu_s\right)^2}{\frac{1}{N_{NOISE}} \sum_j \left(x_j - \mu_N\right)^2} = \frac{\sigma^2_{SPIKE}}{\sigma^2_{NOISE}},$$

where, P is the power of the noise or spike, x is a segment of voltage, i corresponds to an index of the spike shape, j corresponds to an index in the noise trace, N_{SPIKE} is the number of points in the spike shape, defined to be 64 as described above, N_{NOISE} is the length of the concatenated noise traces (see below), μ_s is the mean amplitude of the spike shape, μ_N is the mean amplitude

of the noise, and σ^2 is the variance. Due to the highly variable shapes of spikes it is inappropriate to use the square of the peak-to-peak of a given spike shape as the power of the spike. Two spike shapes may have highly differing widths but may still have the same peak-to-peak value. Due to their highly differing widths one shape may be much easier to detect, thus they should not each have the same snr value. Using the full 64-sample window is an arbitrary choice but it allows for consistency across a widely varying set of spike shapes and returns reasonable values for snr. To obtain the SNR for a given voltage trace we average the snr values of all detected spikes.

Constructing artificial spike trains:

Following standard methods (Quiroga et al., 2004; Letelier et al., 2000), I constructed artificial data sets to test the thresholding and spike sorting procedure. While more complex and detailed methods have been proposed (Smith et al., 2007), the method herein contained matches with the statistics and spectra of real data voltage traces (**Fig. 2.4**). The data generation has two main steps: making the underlying noise, composed of a combination of background spikes and white noise, and making and placing the primary spikes.

All spikes are modeled directly from real spikes recorded within the frog (see **Chapter 3**) or turtle (Saha, personal communication) and are similar in width and overall shape to spikes seen in other systems. We generated 36 different model spikes (**Fig. 2.3**).

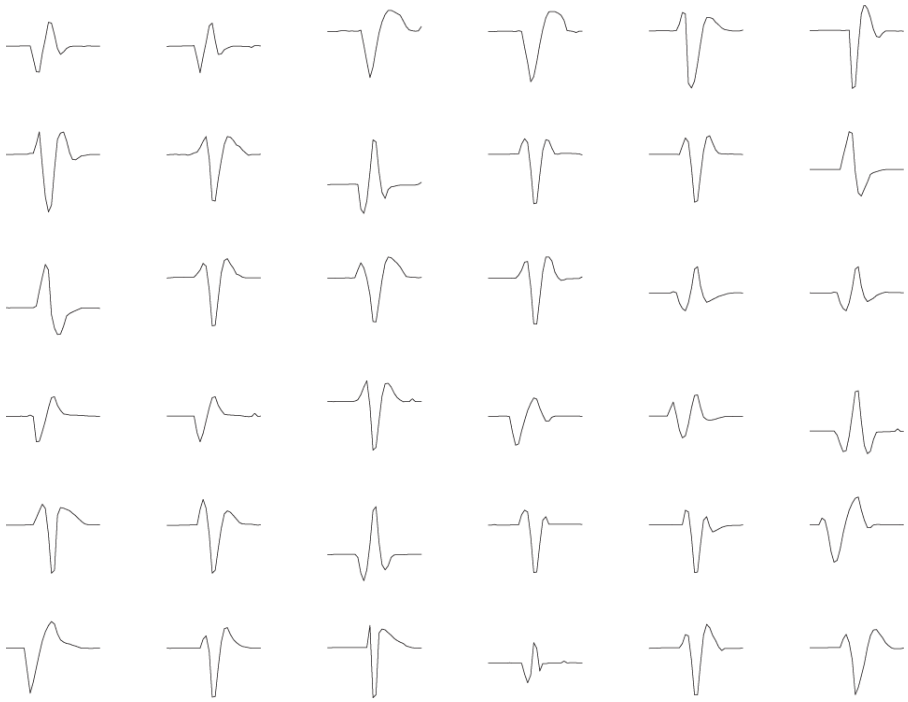

Figure 2.3: Spike shapes used to form noise and large SNR spikes in artificial voltage traces.

As mentioned above, to match the statistics of background noise from actual neurological recordings, the noise must be composed of two different components: small amplitude background spikes, and Gaussian white noise. Physically, a small amplitude background spike arises from the activity of neurons a moderate distance from the recording electrode (in **Fig. 2.1**, the black neurons which still reside within the circle surrounding the electrode). The white noise arises from activity of neurons a greater distance away from the recording electrode (outside of the circle in **Fig. 2.1**) as well as other sources of background noise: electronic noise in the circuit, and small extracellular transients within the neural tissue. As mentioned in assumption (4) above, the

statistics of these transients tend towards a Gaussian distribution as recording time approaches infinity.

The underlying noise was generated in a two-step process. First, at every time step there exists a probability that a background spike will be inserted as part of the underlying noise. This probability is defined as the fullness, F. When a background spike is inserted, a spike shape is chosen from the model set with equal probability and the power of the inserted spike (as defined above) is chosen from a Gaussian distribution with zero mean and a standard deviation of one. The spike shapes are 30 times steps in length. Second, white noise is added to the voltage at each time step. The amplitude of the added noise for a given time step is taken from a Gaussian distribution with zero mean and a tunable standard deviation parameter called the whiteness, W.

Tuning the two parameters, F and W, allowed me to match the power spectrum of our synthetic noise to that of actual recorded biological noise. If F is too low, the power spectrum is too flat (too white) to be relevant for biological noise. If W is set too low there are not enough contributions in the high frequency region of the power spectrum (**Fig. 2.4**). F and W have been empirically determined to be: F = 0.4, W = 2.2.

The noise was normalized to have unit standard deviation. Primary spikes were then inserted independently based on a Poisson spike train with an instantaneous average firing rate unique to each spike shape. A 2-ms refractory

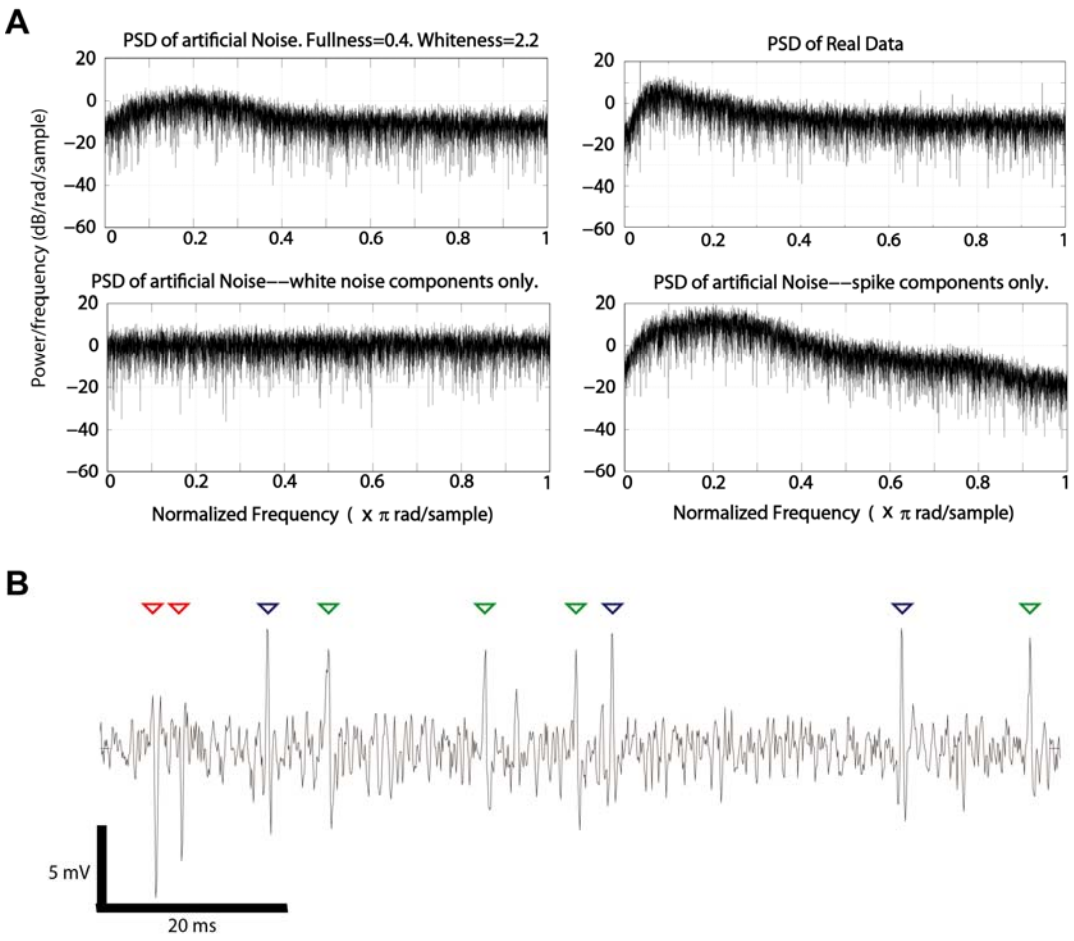

Figure 2.4: Constructing artificial spike trains**. (A)** Power spectral density (PSD) of an artificial voltage trace (top left) and of a voltage trace recorded from the nucleus isthmi of the frog (top right). The frequencies have been normalized to the Nyquist frequency (f_N) which is equal to half the sampling rate. Note the flatness of both spectra above 2000 Hz. This is achieved through the inclusion of pure white noise (lower left). Whereas the bump at lower frequencies is achieved via the inclusion of small amplitude spike shapes (power spectrum of noise generated by only spike shapes in lower right). The particular size of the bump is driven by the average firing rate of large SNR spikes, and there is a 1/f falloff between about 500 Hz and 2000 Hz. **(B)** A sample artificial trace at SNR of 3. The colored triangles mark the placement of different spike shapes.

period was enforced for each unit (spike shape type). The power of an inserted spike was not necessarily the same between different units. The signal-to-noise ratio of the whole voltage trace (SNR) was determined according to the power (as defined above) of the lowest-power spike included (after including additive noise) divided by the power of the underlying noise:

$$SNR = \frac{P_{smallest-spike}}{P_{noise}}.$$

Artificial voltage traces were constructed which had seven different SNR's (1.5, 2.0, 3.0, 4.0, 5.0, 10.0, 20.0) and 20 average multi-unit firing rates (5, 10, 15, 20, …, 95, 100 Hz), and varying degrees of overlap of spike shapes and spike shape similarity. Because the artificial trains are stochastic in nature, 100 trains were constructed for each set of parameters when testing the thresholding or clustering (see below).

Two additional parameters were taken into account when creating the artificial spike trains: the number of different primary spike shapes to be included within the trace, and the level of similarity between the primary spike shapes. As stated above, when placing spike shapes into the noise, there is a flat probability distribution from which to choose a spike shape. Any number of any of the spikes in the bank of spike shapes could be used. When constructing the artificial voltage traces I used three different spike shapes for the primary spike shapes. Using a larger number of spike shapes does not affect the quality of

detection by any of the tested thresholds (data not shown). The level of similarity between the primary spike shapes was quantified by the following process.

First, the each spike shape was normalized to have a power (as defined above) equal to unity. The mean was then subtracted off of each spike shape. A symmetric 36X36 matrix was constructed to quantify the dissimilarity between all pairs of spike shapes. This measure of dissimilarity was defined by:

$$Dissimilarity_{i,j} = \frac{1}{N}\sqrt{\sum_{k=1}^{N}\left(x_{k,j} - x_{k,i}\right)^2},$$

where N is the length of the spike shape, here equal to 30 as shown above, and $x_{k,j}$ is the k^{th} component of the j^{th} spike. Basically, the dissimilarity matrix collects the norms of the differences of all spike shape pairs. The maximum element in this matrix gives the two most dissimilar spike shapes, corresponding to spikes n and m. I then multiplied the n^{th} and m^{th} rows together, element by element. The maximum element in the resulting vector is the spike shape which is most dissimilar to the first two spike shapes. Starting with an arbitrary spike shape and following in this fashion, it is possible to order all remaining spike shapes by level of mutual dissimilarity to the set of spikes which have already been chosen.

Creating artificial spike trains with sets of spike shapes which vary in their degrees of dissimilarity to each other did not in any way affect the results of the tests on different thresholds. While they did alter the relative percentages of

false classifications among either the K-means or the superparamagnetic clustering algorithms, the latter algorithm always out performed K-means clustering (data not shown).

I: SPIKE DETECTION

Determining the threshold:

A very common method for detecting spikes is to set a single threshold in the voltage trace. This method can be compromised by low-frequency high-amplitude noise and it may miss negative-polarity spikes entirely. While this can work very well with a well-isolated unit in a large SNR environment, it can miss spikes which are closer to the noise level when recording from neural tissue with a large density of active units. In order to detect spikes of any polarity, and to detect spikes as close as possible to the noise level, I developed a threshold determined by the data itself to apply to the square of the first derivative of the voltage trace. A sample artificial voltage trace is shown in **Fig. 2.5A**.

First, the entire voltage trace is smoothed by convolving it with a Gaussian that is of a similar width as a typical spike for our system; in our case that is a Gaussian of half-width 0.6 ms. Second, the two-sided first derivative (see below) is calculated and the probability distribution function (PDF) of the first derivative values is constructed.

Numerically, a two-sided derivative is equivalent to convolving the voltage trace with a three point function, [1 0 -1], and removing the edge artifacts. This

two-sided derivative is more accurate than a one-sided regular derivative. The PDF is obtained by creating a set of bins corresponding to the range of the values in the first derivative of the smoothed data. Each bin width is typically set to one thousandth of the range from the minimum first derivative value to the maximum first derivative value. Each time the first derivative has a value which

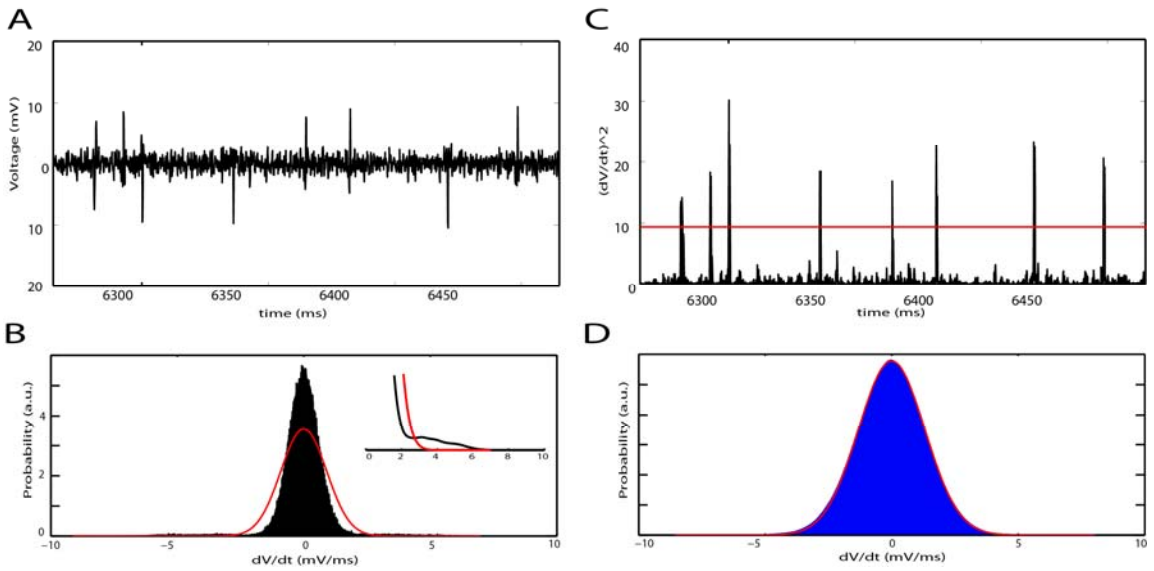

Figure 2.5: Determining the threshold. **(A)** A raw artificial voltage trace. **(B)** The PDF for the first derivative values is shown in black. The associated Gaussian distribution is shown in red (see text for details). **Inset**: The envelope for the PDF is shown in black. The value where the PDF for the data equals the Gaussian distribution is taken as the threshold. **(C)** The threshold is squared and used on the square of the first derivative to detect spikes of any polarity**. (D)** The PDF for the remaining noise trace after the spikes have been removed is in blue. The associated Gaussian distribution is shown in red. Note that the PDF of the noise matches closely the associated Gaussian.

falls into a bin the number within the bin is increased by one. The PDF is normalized by dividing by the total number of points so that the integral of the

PDF over all possible values is 1. The distribution has a given mean, μ, and standard deviation, σ, which is used to construct a Gaussian distribution, $N(\mu,\sigma)$, that has the same mean and standard deviation as the data:

$$N(\mu,\sigma) = \frac{1}{\sigma\sqrt{2\pi}} e^{-\frac{1}{2}\left[\frac{\left(\frac{dV}{dt}-\mu\right)}{\sigma}\right]^2},$$

(**Fig. 2.5B**). The threshold is taken to be the point where the Gaussian distribution equals that of the data's distribution and at higher first derivative values dips below the PDF of the data. Above this point, there is a higher probability that the value belongs to the data than to a Gaussian distribution. Thus, due to assumption (4) above, it is more likely that the high value corresponds to a spike rather than to the underlying noise.

The PDF of the first derivative is nearly Gaussian but has a great degree of kurtosis (**Fig. 2.5B**). Kurtosis, γ_2, is the fourth standardized moment of a distribution is given by:

$$\gamma_2 = \frac{\mu_4}{\sigma^4} - 3,$$

$$\mu_4 = \frac{1}{N}\sum_i (x_i - \mu)^4,$$

where σ is the standard deviation of the distribution, μ is the mean of the distribution and μ_4 is the fourth moment of the distribution. Kurtosis describes

the peakedness of the distribution. A Gaussian distribution has zero kurtosis. If a distribution has a high kurtosis then the center is very peaked and the tails are longer owing to infrequent extreme values. In the example shown, the kurtosis of the data is 10.385 while that of the noise after removing the spikes is 0.394 (see **Fig. 2.5D**). Above the threshold there are significantly more extreme values in the data, which correspond to the presence of spikes.

The threshold is squared and applied to the square of the first derivative so that both spike polarities are included (**Fig. 2.5C)**. Spike times are taken to be when the square of the derivative peaks immediately following the threshold crossing. A vector, S, is created for each spike which incorporates 64 voltage samples aligning the spike time to sample number 20 of the vector. The 20^{th} sample is chosen as the alignment point because there is more information in the spike shape after the peak than before it. These 64-dimensional vectors will be the basis for our spike sorting. Alternatively, one can use a separate threshold determined from the positive crossing of the PDFs and a negative threshold from the left side of **Fig 2.5B**. I chose to use the one threshold for simplicity. In practice they lead to nearly identical results.

Thresholding the square of the first derivative also increases the SNR between spikes and noise. The ratio of the power of the spikes to that of the noise in the voltage trace are far below those of the ratio of the square of the first derivative to the baseline noise around the peaks in that function (**Fig. 2.5C**). Thus, using this function widens the SNR gap allowing more spikes to be

detected. The times between spikes in the voltage trace are taken to be noise. The noise of a voltage trace can be analyzed by concatenating these noise segments together. A probability distribution of the voltage values in the noise (**Fig. 2.5D**) has a kurtosis near zero. The concatenated noise has a distribution very similar to a Gaussian distribution. In fact, it is significantly more Gaussian than the distribution of values which included the spikes. Thus, our fourth assumption, that the underlying noise is roughly Gaussian, is valid.

Overlapping spikes pose a unique problem (see, e.g. **Fig. 2.9)**. It is common to program a 'dead time' into the detection code so that not all local minima of a spike shape are considered as separate spikes. This dead time is typically taken to be around 1 ms. For example, I use a 64-point window for a spike shape corresponding to 6.4 ms. I use a dead time window of 0.7 ms after a spike peak is detected to ensure that the algorithm moves beyond all of the local extrema in the spike shape before detection resumes.

Note that following assumption (1) above, a given unit's spike vectors will all point to the exact same point, or manifold, in the event space. It is the noise which spreads out the point, or manifold, to a cloud in event space, thus complicating any clustering algorithm. If the noise is purely Gaussian this cloud will be a hyper-sphere, because the noise in each direction will be uncorrelated. By transforming the covariance of the underlying noise to that of Gaussian white noise one can optimize the data for the clustering routine. This process is called noise whitening.

Noise Whitening:

The noise sections of the voltage trace are close to being Gaussian but they are not Gaussian. Following standard methods (Pouzat et al., 2002; Duda et al., 2006) the noise can be whitened, providing a transformation matrix, W, used to whiten the spike vectors. Whitening the vectors is equivalent to uncorrelating the variance due to noise within the spike shapes and can aid in optimizing the sorting procedure (Bankman et al., 1993).

First, the autocorrelation (AC) of the concatenated noise traces is calculated after subtracting off the mean. The longer the section of noise, the smoother the autocorrelation will be. Next, a Toeplitz matrix (Grenander et al., 1958) of the first 64 samples of the autocorrelation of the noise is created, which has the form, $AC_{i,j} = AC_{i-1,j-1}$. For example, if the autocorrelation vector, AC, has three elements, the Toeplitz matrix takes this form:

$$T_{AC} = \begin{pmatrix} AC_i & AC_j & AC_k \\ AC_j & AC_i & AC_j \\ AC_k & AC_j & AC_i \end{pmatrix}.$$

The whitening transformation matrix, W, is chosen so that the variance due to noise is uncorrelated across dimensions, i.e. the autocorrelation of the whitened noise will be the identity matrix. In other words,

$$T_{AC}{}^{-1} = W^T W ,$$

where W can be found via a Choleski decomposition (Pouzat et al., 2002; Brandt, 1999). W is then used to whiten the spike shapes.

II: FEATURE EXTRACTION

Wavelet analysis:

There are many useful sources for a good explanation of the wavelet transform (see, e.g. Mallat, 1989; Strang, 1993; Burrus et al., 1997; Letelier et al., 2000; Hulata et al., 2002). I will only give a brief description here. The discrete wavelet transform (DWT) is a mapping of a 1-dimensional, finite energy (square integrable: $f(t) \in L^2$) function, $f(t)$, onto a 2-dimensional time-frequency space. Correlating the signal with wavelets of different size extracts details of the signal at multiple scales. Arranging these correlations in a hierarchical scheme is called multiresolution decomposition (Mallat, 1989; Cui, 1992; Letelier et al., 2000; Quiroga, 2004). The multiresolution decomposition localizes high (spike) or low (after-hyperpolarization) frequency contributions in time rather than using a sum of infinitely long frequency components as does a Fourier transform (Strang, 1993; Letelier et al., 2000). The transform utilizes wavelets which form an orthonormal basis of square-integrable functions which are each derived from a "mother wavelet," $\Psi(t)$, chosen for the particular task at hand. Due to their basic form, I use the Daubechies-1, or Haar, mother wavelet (Chui, 1997; Burrus et al, 1998; Quiroga, 2004; Press et al., 2007), though a number of mother wavelets can give reasonable results. I could instead use a wavelet which looks like a

typical spike, such as a Daubechies-8 (Letelier, 2000), but this assumes a given form for the spikes. The Haar wavelet is the most general.

The Haar mother wavelet is defined by:

$$\Psi(t)=\begin{cases}1, & 0\le t<\frac{1}{2}\\ -1, & \frac{1}{2}\le t<1\\ 0, & otherwise\end{cases}.$$

For the DWT, the mother wavelet does not have to be given in a closed form, but it must generate, via the following equation, an orthogonal, dyadic, non-redundant mapping onto time-frequency space (Meyer, 1993). The wavelets spanning the space are shifted and dilated versions of the mother wavelet:

$$\varphi_{j,k}(t)=\frac{1}{2^{\frac{j}{2}}}\Psi\left(2^j t-k\right),\qquad k=0\rightarrow N-1,\quad j\rightarrow 1:\log_2(N).$$

The scaling index, j, changes the behavior of the wavelet in frequency space. The translation index, k, shifts the wavelet along the time axis. The data vector, S, is 64 samples long, thus k runs from 0 to 63 and j can run from 1 to 6, and N =64. Since the wavelets form a complete basis, a linear combination can be used to describe any waveform:

$$f(t)=\sum_{j,k}c_{j,k}\varphi_{j,k}(t).$$

As in Fourier analysis, the coefficients can be found by taking the dot product of the original signal with the associated wavelet:

$$c_{j,k} =< \varphi_{j,k}(t) |\ f(t) > .$$

Where, for real valued functions,

$$< A(t) |\ B(t) > \equiv \sum_{i}^{N} [A(i) \cdot B(i)].$$

In multiresolution decomposition, high- and low-pass quadrature mirror filters (QMF) are generated from the chosen wavelet basis and used to deconstruct the original signal in a pyramidal hierarchical scheme (Press et al., 1993; Cui, 1997; Burrus et al., 1998; Letelier et al., 2000). This scheme uses an iterative matrix multiplication of the signal vector with a series of filter matrices to obtain the $c_{j,k}$'s. The QMF matrices are constructed so that they treat the signal as if it were periodic with wrap-around boundary conditions. This results in circulant rectangular matrices with half the number of rows as columns. Multiplication with these matrices performs a convolution with the input as well as down-samples the input vector by a factor of two. Using the Haar basis, the high- (HP) and low-pass (LP) QMFs are of the form (respectively):

$$HP_j = \frac{1}{\sqrt{2}} \begin{vmatrix} 1 & 1 & 0 & 0 & \cdots & 0 \\ 0 & 0 & 1 & 1 & \cdots & 0 \\ \vdots & & & \ddots & & \vdots \\ 0 & 0 & 0 & \cdots & 1 & 1 \end{vmatrix}, \qquad LP_j = \frac{1}{\sqrt{2}} \begin{vmatrix} 1 & -1 & 0 & 0 & \cdots & 0 \\ 0 & 0 & 1 & -1 & \cdots & 0 \\ \vdots & & & \ddots & & \vdots \\ 0 & 0 & 0 & \cdots & 1 & -1 \end{vmatrix},$$

where there are n-rows and $\frac{n}{2}$-columns where $n = \frac{N}{2^j}$, where, recall, that j is the scaling index, and N is the length of the original data vector, S (Press et al., 1993; Cui, 1997). Each row contains two filter coefficients from the Haar basis, shifted to the left two positions from the row above it. The rest of the values in the matrices are equal to zero.

The hierarchical algorithm proceeds as follows: The original data vector, S, is multiplied by each of the filters:

$$HP_1 * S = d_{-1}, \quad LP_1 * S = a_{-1},$$

where the, '$*$,' denotes matrix multiplication, and d_{-j} is the output vector from the high-pass filter which holds detailed information of the input vector over the frequency range $\left[\frac{f_N}{2^j}, \frac{f_N}{2^{j-1}}\right]$, where f_N is the Nyquist frequency. The output of the low-pass filter a_{-j} holds approximate information about the original signal over the frequency range $\left[0, \frac{f_N}{2^j}\right]$. The subscript of the output vectors reflects the level of the hierarchical algorithm. The output vector from the high-pass filter also contains exactly the coefficients $c_{j,k}$ described above for level j. The values of k are given by the indices of the vector d_{-j}.

The next stages of the algorithm multiply the approximation vector a_{-j} by the j^{th} -level matrices for the high-pass and low-pass filters:

$$HP_j * a_{-(j-1)} = d_{-j}, \quad LP_j * a_{-(j-1)} = a_{-j},$$

to obtain the next level in the decomposition. This recursive procedure continues until $j = j_{MAX} = \log_2(N)$. This DWT procedure calculates the 'wavelet spectrum' of N $c_{j,k}$ coefficients for each temporal vector, S (Letelier et al., 2000). The whole procedure is represented graphically in **Fig. 2.6.**

The full range of coefficients $c_{j,k}$ which fully describe the original signal can be collected together from the lowest set of the decomposition:

$$c_{j,k} = \left\{ \vec{a}_{-j_{MAX}}, \vec{d}_{-j_{MAX}}, \vec{d}_{-(j_{MAX}-1)}, ..., \vec{d}_{-1} \right\}.$$

The algorithm can be halted at any level of the decomposition to create this vector of $c_{j,k}$'s which fully describes the original signal's information. It is these $c_{j,k}'s$ that are used as the distinctive features of the spikes.

While one could use the spike shape as a whole, the wavelets allow the spike shape itself to be non-stationary; the transform picks out the most salient features of the spike shape. Also, because the coefficients are specific in time and frequency, the noise, which is typically high in frequency, will play much less of a role in determining the magnitude of the coefficients. For example, if a neuron fires repeatedly within a few milliseconds in a burst, it is well known that the latter spikes are of a smaller amplitude but very similar in overall shape. The

set of wavelet coefficients for these slightly differing spikes arising from the burst will be very similar and show less variability than the spike themselves.

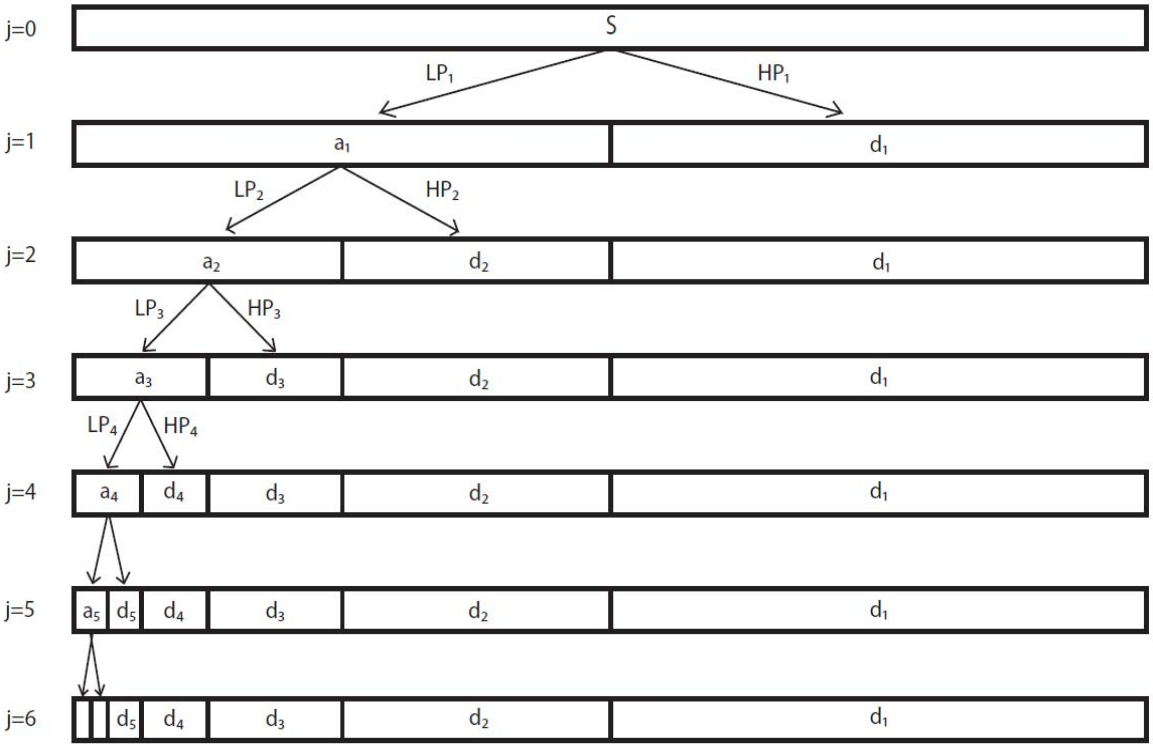

Figure 2.6: Schematic representation of the multiresolution decomposition algorithm. The raw signal, S, is simultaneously filtered through a high-pass, HP_1, and a low-pass filter, LP_1. The detailed output from the high-pass filter is saved. The approximation coefficients from the low-pass filter are passed onto the next level of filtering. See text for details.

The coefficients may not all have the same variability between spikes (**Fig. 2.7**). To lower computation time, it is determined which coefficients are likely to provide the most aid in separating clusters. Rather than simply choose those which have the highest variance, the Kolmogorov-Smirnov (K-S) test can be used to lower the dimensionality (Press et al., 1992; Quiroga et al., 2004). For

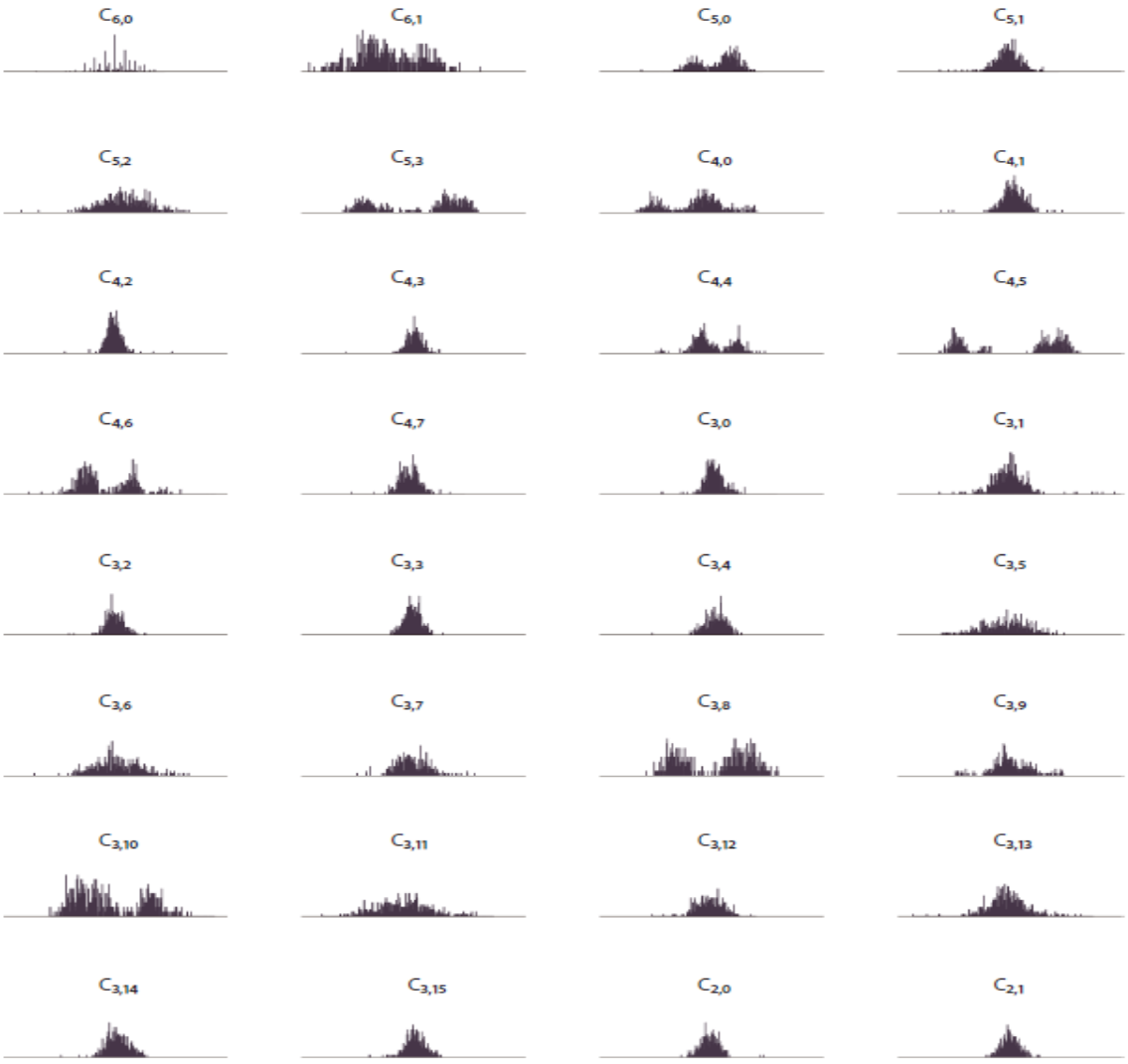

Figure 2.7: Distributions of 32 of the wavelet coefficient magnitudes of the given spike shapes.

each given coefficient, a cumulative distribution function (CDF) is constructed. Then a CDF from an associated Gaussian with the same mean and standard deviation (Ncdf) is constructed:

$$CDF(x) = \int_{-\infty}^{x} pdf(x')dx',$$

$$Ncdf(x) = \int_{-\infty}^{x} \frac{1}{\sigma\sqrt{2\pi}} e^{-\frac{1}{2}\left[\frac{(x'-\mu)}{\sigma}\right]^2} dx',.$$

Taking the maximum of the absolute value of the difference between these two cumulative distributions gives a quantitative measure of how non-uni-Normal the distribution of values is:

$$KS = \max\{abs[CDF(x) - Ncdf(x)]\}.$$

In other words, this test gives a measure of how poorly the distribution can be described by a single Gaussian. The 15 coefficients with the highest K-S values are chosen for the clustering, thus lowering the dimensionality and computational expense of the following algorithm.

III: CLUSTERING

For the clustering algorithm, I am modifying a procedure proposed by Marcelo Blatt and others (Blatt et al., 1996; Blatt et al., 1997) for general classification issues, and specialized for spike sorting by Rodrigo Quiroga (Quiroga et al., 2004). This procedure is superparamagnetic clustering. Superparamagnetic clustering partitions data based on the local structure of the data utilizing neighboring interactions based on an implementation of the Potts model (Wu, 1982; Wang et al., 1990). Because of the novelty and physical basis of this algorithm, I will present in full detail how it works and why this method is

more ideally suited for spike sorting than more traditional methods such as K-means clustering (Duda et al., 2006).

The goal of any clustering procedure is to find a partition in a D-dimensional parameter space that separates data, $\vec{x}_i$, into clusters such that the patterns contained within the clusters are more similar to themselves than to the patterns in the other clusters. It is assumed that the parameter space is a metric space where the dissimilarity between points can be measured, as opposed to a non-metric space, e.g. a space defining a set of apple colors being red, yellow, or green. Once this metric space has been set there is defined a measure of dissimilarity d_{ij} between points:

$$d_{ij} = \left| \vec{x}_i - \vec{x}_j \right| .$$

There are two main approaches to partitional clustering: parametric and non-parametric (Blatt et al., 1997; Duda et al., 2006). Parametric approaches assume some type of *a priori* knowledge of the underlying structure of the data, e.g. the clusters can all be described by a mean with a Gaussian distribution of points in the multivariate space. These assumptions are typically incorporated into a global criterion. An 'ideal' partition of the data is obtained by maximizing (or minimizing) this criterion. Typical examples of this approach are variance minimization, maximal likelihood, Gaussian mixtures, or K-means (Duda et al., 2006). These methods can be computationally expensive and there is no guarantee that the method does not get stuck in a local minimum of the criterion.

A major drawback of these methods is that the number of clusters in the data must be assumed beforehand. Then the criterion for the given number of cluster centers is extremized. In spike sorting neural data, there is no *a priori* way to determine how many units are contributing to the spikes present in the voltage trace. Bayesian methods have been proposed for determining the most likely number of clusters (see, for example, Pouzat et al., 2000). However, these methods can be computationally very expensive when clustering a large number of spikes and may not deal very well with non-Gaussian distributions within the data, as comes about with spikes occurring during a burst.

If no *a priori* information can be assumed about the structure of the data, it may be more useful to use a local criterion and adopt a non-parametric approach to build clusters around high density regions of the data (Blatt et al., 1996). A non-parametric approach which has been shown to work quite well for the case of spike sorting is superparamagnetic clustering. This approach is realized as a Monte Carlo implementation of the Potts model, a generalization of the Ising model of magnetism.

In the Ising model, magnetic spins are placed on a regular lattice. The spins can take a value of +/-1. The spins can interact with their nearest neighbors via some interaction energy J. The Hamiltonian for this system (without an external magnetic field) is:

$$H\left[\{s\}\right]_{ISING} = -J\sum_{\langle i,j\rangle} S_i S_j$$

where S_l are the spin values and '$\langle\ldots\rangle$' denotes only summing over nearest neighbors.

The Potts model generalizes the parameters allowing for any of q configurations for an individual spin. Again, the spins may interact via an interaction energy but now only spins with the same configuration interact with one another:

$$\mathrm{H}\left[\{s\}\right]_{Potts} = -\sum_{\langle i,j\rangle} J_{ij}\delta_{s_i s_j} \ .$$

where, again, '$\langle\ldots\rangle$' denotes only summing over neighbors, $\delta_{m,n}$ is the Kronecker delta function where $\delta_{m,n} = 1$ only if $m = n$, where, $m, n = 1,\ldots,q$. The interaction energy, J_{ij} ,is defined such that more weight is given to data points which are closer in the parameter space. Because local interactions are assumed to dominate, the interaction energy does not need to be calculated for all points, only points which are neighbors to each other. Neighbors are defined by points which share a common Voronoi tessellation boundary with each other (Bowyer, 1981; Watson, 1981) (**Fig. 2.8**). A fast algorithm for determining the tessellation in a high dimensional space was developed by Barry Joe (Joe, 1989).

A length scale is defined for the model by the average nearest neighbor distance a which is governed by the high density regions and is less than the

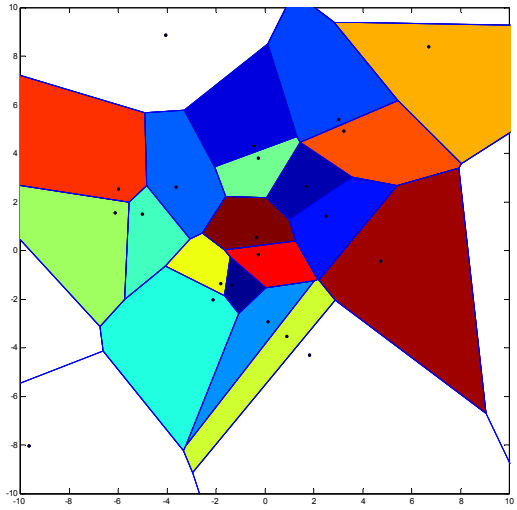

Figure 2.8: An example Voronoi tesselation**.** Points within a colored boundary are closer to the dark spot in the boundary than any other. Dark spots which share a common boundary are by definition nearest neighbors.

typical distance between points in the low density regions. Defining the average number of nearest neighbors as K, the interaction energy J_{ij} is given by:

$$J_{ij} = \begin{cases} \frac{1}{K}\exp\left[-\frac{\left\|\vec{x}_i - \vec{x}_j\right\|^2}{2a^2}\right], & \text{if } \vec{x}_i \text{ and } \vec{x}_j \text{ are neighbors} \\ 0 & \text{otherwise} \end{cases}$$

Once this is computed for all neighbors, an initial random state $s = 1,\ldots q$ is assigned to each data point $\vec{x}_i$. Then M Monte Carlo iterations are performed where a spin is chosen at random to be changed to a new state. The number of iterations is typically set to 1000. If a nearest neighbor's state is in the same

initial state, then there exists a probability that it will also change state. If it changes, then its nearest neighbors are also subject to the same probability of flipping. Thus, rather than flipping individual spins one at a time as is done in a Metropolis algorithm (Hastings, 1970), entire islands of spins are flipped with each step. This significantly increases the speed of the algorithm. This method of flipping is known as the Wolf algorithm (Wolf, 1989, Quiroga et al., 2004). The probability for flipping a neighboring spin is given by:

$$p_{ij} = 1 - \exp\left[-\frac{J_{ij}}{T} \delta_{S_i S_j} \right],$$

where T is the temperature. The M iterations are run for a series of temperatures, typically from 0.01 to 0.40 increments of 0.01. For each temperature the magnetization m and the susceptibility χ are determined by:

$$m = \frac{\left(\frac{N_{\max}}{N} \right) q - 1}{q - 1},$$

$$\chi = \frac{N}{T} \left[\left\langle m^2 \right\rangle - \left\langle m \right\rangle^2 \right].$$

where N_{MAX} is the size of the largest cluster. Cluster membership is determined by the spin-spin correlation function $\left\langle \delta_{S_i S_j} \right\rangle$ which must be above a given threshold Θ.

A sample distribution of data which cannot be properly described by a Gaussian mixture is given in **Fig. 2.9A**. The susceptibility χ shown in **Fig 2.9B** determines the state of this system. At low temperatures, fluctuations of the magnetization are small, therefore the susceptibility is small and the system is in a ferromagnetic phase where the entire system behaves as one class due to the flipping probability described above. At very high temperatures, the spins are all flipping independently regardless of their interactions thus the susceptibility is

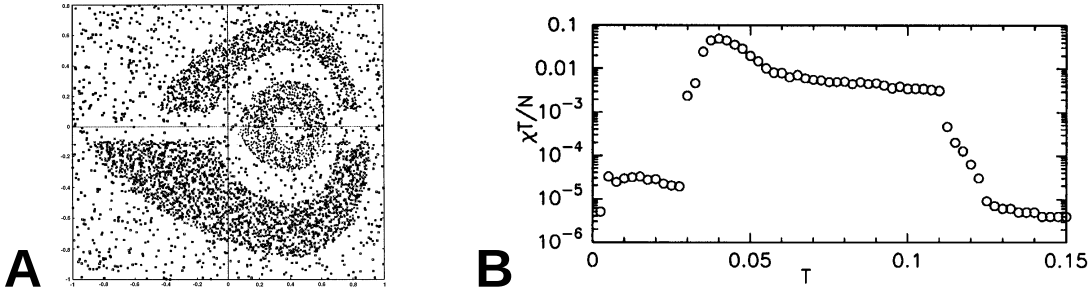

Figure 2.9: **(A)** Data distributions which cannot be parametrized by a mean with a surrounding distribution. **(B)** Susceptibility density of data in (A). Note the presence of the three phases. See text for details. Both adapted from Blatt et al., 1996.

very low as well. This is the paramagnetic region. At intermediate temperatures, only those spins which are grouped together will change their spins together; each cluster behaves as its own magnet. This phase is the superparamagnetic phase and is observed by a spike in the susceptibility when raising the temperature. After the spike, the susceptibility stays at a high level until it suddenly undergoes a transition to the paramagnetic phase (**Fig. 2.9B**). Once the superparamagnetic phase has been localized, the clusters are assigned.

This algorithm is quite robust to varying thresholds, q values, and the number of nearest neighbors K used. I use: $q = 20, K = 15, \Theta = 0.5$. Typically, q needs to be higher than a reasonable maximum number of clusters within the data, but low enough so as to not slow down the algorithm. The threshold Θ could be between 0.1 and 0.9 and will still yield very similar results.

A very attractive part of his algorithm is that it finds and outputs the number of clusters. It also works quite well with varying cluster sizes. Typically, if there are clusters present of drastically different sizes, or if some clusters arise as sub-clusters of a larger cluster, there will be multiple spikes in the susceptibility. The temperature used for the actual classification is typically the temperature immediately following the last spike in the susceptibility before the final plateau. The temperature at which the classifications are made can be tuned when necessary, though I have found that it works very well being minimally supervised.

It is very important to perform additional checks on the output of the sorting algorithm. For example, all spiking units have a refractory period after each spike. This is always of order a couple of milliseconds, though in certain circumstances it can fall to around a millisecond. Thus, it is always advisable to construct inter-spike interval (ISI) distributions for the clustered spikes. These ISI distributions are a good quick check to ensure that the algorithm is not grouping separate clusters into a single cluster. If the ISI distribution is not zero below a couple of milliseconds, then there is a high probability that multiple clusters have

been combined together. An ISI distribution for a well separated cluster should exhibit no intervals below one or two milliseconds. A look at the autocorrelation of the resulting spike train will also provide a good check. The autocorrelation computes the time-like correlations within the spike train. It should also have values equal to zero for time lags between zero and one or two milliseconds. Finally, it is good to check the results of the clustering with a plot of the mean spike shape +/- its standard deviation. If the standard deviation is not flat across the whole of the spike shape then there is a high probability that multiple clusters were combined and the algorithm should be re-run (as it is stochastic) or its parameters tweaked a little bit.

RESULTS:

Spike Detection:

The detection method was tested with artificial spike trains over a range of seven different signal-to-noise levels, SNR's, (1.5, 2, 3, 4, 5, 10, and 20) and 20 different multi-unit average firing rates (MUAFR) ranging from 5 Hz up to 100 Hz. For each SNR/MUAFR pair, 100 unique spike trains were stochastically generated to obtain good statistics. **Fig. 2.10** shows two examples of such spike trains. Each was generated with three distinct spike shapes which are marked with the colored triangles in the plots. Notice how upon inspection it is not trivial that there are only three spike shapes present. Also note that even at this

moderate MUAFR there is a significant probability for an occasional overlap of spike shapes (see **Fig. 2.10B** at time point 2000) (Lewicki, 1998).

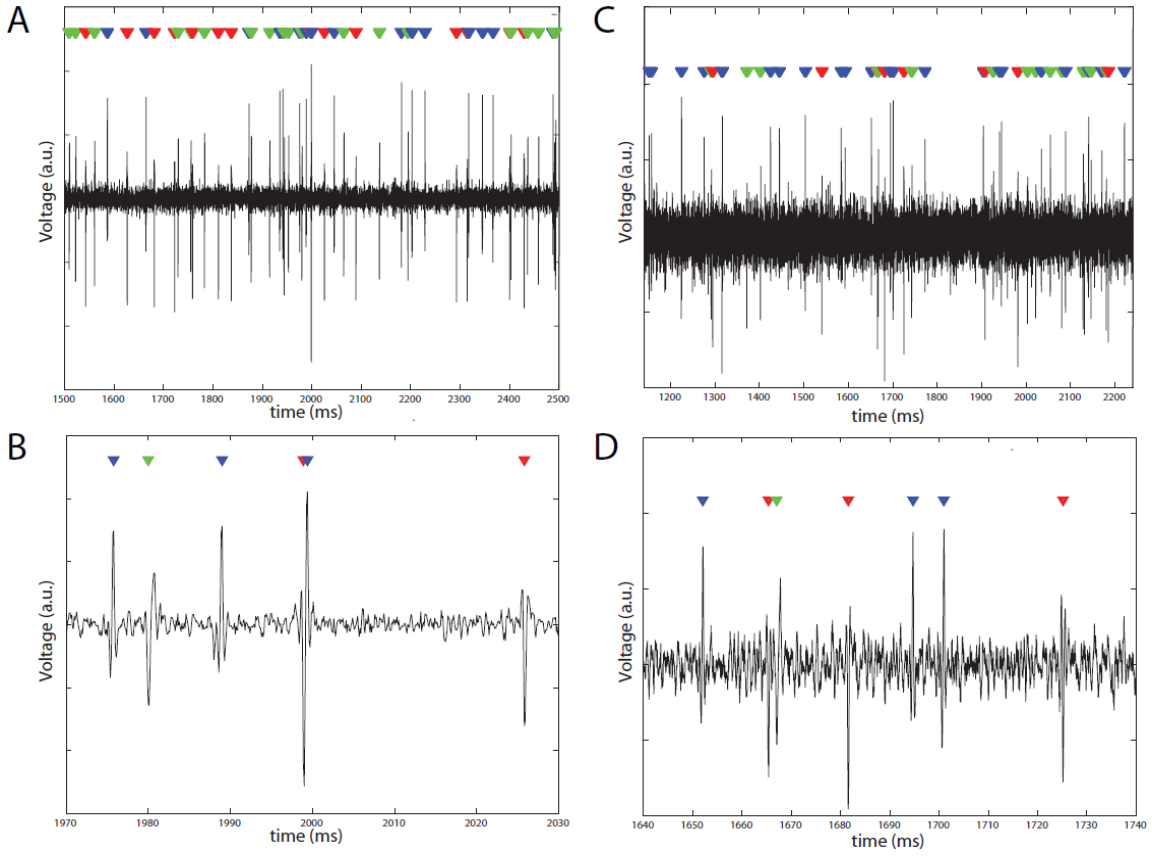

Figure 2.10: Example artificial spike trains. (**A**) SNR=5, MUAFR=50. (**B**) Zoom in of plot in (A) showing a superposition of spike shapes. (**C**) SNR=2, MUAFR=50. (**D**) Zoom in of plot in (C) displaying more spike shape overlap. Times in all plots are in milliseconds and voltages are in arbitrary units. Colored triangles denote different classes of spike shapes.

Figure 2.11 summarizes the percentages of detected false positives and false negatives resulting from using various types of thresholds tested with each MUAFR tested and it shows 4 of the tested SNR's. For all plots, the percentage values were determined relative to the actual number of spikes present in the

recording. Thus, if there were 20% false positives, that means that the number of false positives equaled one fifth of the number of actual spikes present in the recording. SNRs of 5, 10, and 20 are left out of the figure for clarity; the results for these high SNR values mirrored those obtained for an SNR of 4. Each color corresponds to a different SNR. Our method was tested along with other common methods: a threshold proposed recently (Quiroga et al., 2004), labeled 'Quiroga,' and a more typical threshold taken from the literature (for example, Pouzat et al., 2002), labeled, 'Classic.' These thresholds are given by:

$$THRESHOLD_{Quiroga} = 4 \times median\left\{\frac{abs[x]}{0.6745}\right\}$$
$$THRESHOLD_{Classic} = 3 \times SD[x],$$

where 'x' is taken to be the whole voltage trace, and 'SD' is the standard deviation. Typically, these two thresholds are set in the raw voltage trace, but they were also tested with the first derivative of the voltage trace to directly compare with our method. There was no improvement in the results (data not shown).

For all threshold varieties, very few of the detected spikes were false positives for SNR greater than or equal to four (**Fig. 2.11**). The classic threshold, set as a multiple of the standard deviation of the whole voltage trace, suffers from a small percentage of false positives at low MUAFR over most of the SNR values. Quiroga's threshold, based on a multiple of the median value of the whole voltage trace, exhibits hardly any false positives in its detected spikes for

the whole range of SNRs and MUARFs tested. My threshold is based on the relationship between the distribution of first derivative values of the voltage trace to a Gaussian distribution of the same mean and standard deviation. This threshold does have a significant number of false positives in the set of detected spikes at very low SNRs when the MUAFR is low. Note that the number of false positive detections falls off steeply as the MUAFR increases. Even though the

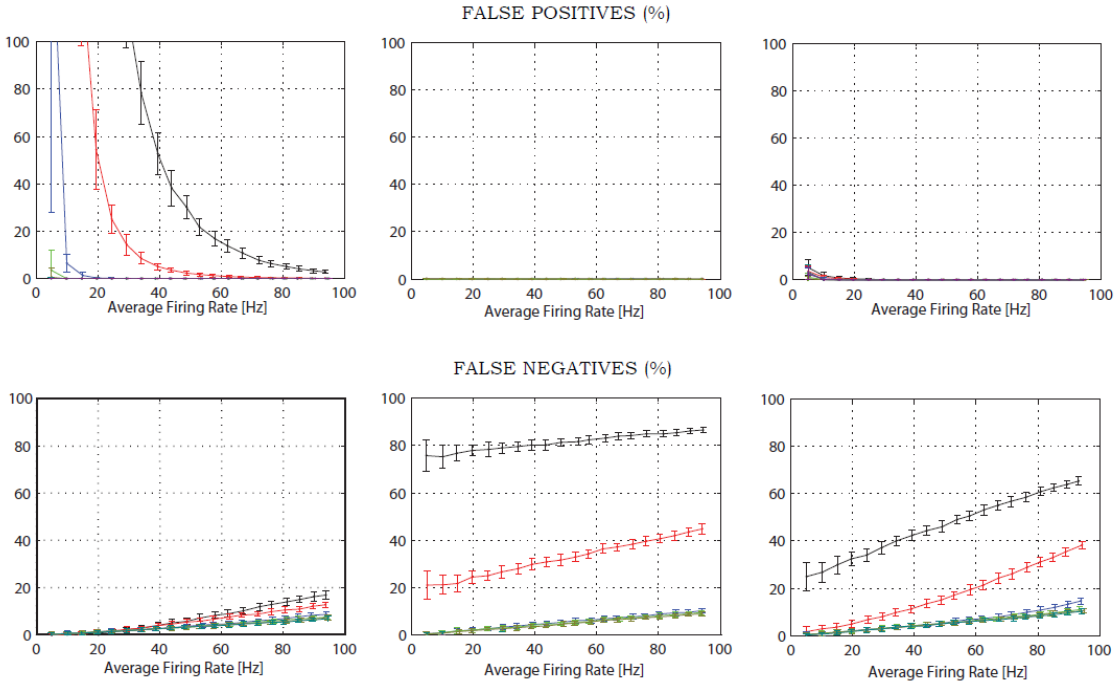

Figure 2.11: False positives and false negatives for various types of thresholds. **LEFT**: My threshold from Fig. 6. **CENTER**: Quiroga's threshold. **RIGHT**: the classic threshold. Results are based on 100 trials averaged for each MUAFR and SNR pair. SNR values: Black=1.5. Red =2. Blue =3. Green =4. Percentages are relative to the number of actual spikes present in the recording (hence, false positives can be higher than 100%).

number of false positives can be high for low SNR and low MUAFR, these 'noise-spikes' will not pose a great problem for the analysis of the spike trains. The reason why is that the 'noise-spikes' will become clustered together away from the clusters of the actual spikes during the superparamagnetic clustering procedure. When in doubt, it always wise to perform the above-mentioned tasks to check the quality of the clustering. The goal of this threshold is to detect all spikes present and then filter out the noise rather than miss some spikes at the early detection phase.

The false negatives are the spikes which were present in the voltage traces but were not detected by the set threshold. The classical threshold works very well for high SNR values (blue and green traces) over a wide range of MUAFRs. However, at SNR at or below 2 (red and black, respectively) the percentage of missed spikes is high. For example, at a MUAFR of 80 Hz and an SNR of 2, the classic threshold misses nearly one-third of all spikes present. The results are even worse for a lower SNR. Quiroga's threshold also suffers from very few false negatives (center of **Fig. 2.11**). In fact, his proposed threshold does even better than the classic threshold at moderate to high SNR values. The rise in false negatives as the MUAFR is increased is less steep for Quiroga's threshold than for the classic. However, at and below a SNR of 2 the numbers of false negatives actually rises much worse than the classic threshold; Quiroga's threshold overestimates the best threshold for spike detection thus leading to very few false positives but also leading to many false negatives.

My threshold does not miss many spikes at low SNR levels, and in fact detects a far better percentage than the other two thresholds tested here. As the MUAFR is raised, the percentage of missed spikes steadily rises with a low slope, as there are when using the other thresholds. The percentage of missed spikes is no worse for my method than with the others. In fact, as the SNR level deteriorates, my method still detects those spikes which have a SNR very close to the noise level. Even at a SNR as poor as 1.5, my threshold does not break down as the others do. For a recording with a MUAFR of 80 and a SNR of 2, my threshold misses around 10% of the spikes present in the recording. The classic threshold misses nearly one-third and Quiroga's threshold fails to detect 40% of the spikes present in the voltage trace.

DISCUSSION:

I described in this chapter a complete and unsupervised method for spike sorting. The threshold is determined by the statistics of the recording site. The clustering method is fast and robust to varying cluster shapes and sizes. This algorithm is ideally suited for helping determine where to place an extracellular electrode while recording in neural tissue. Ideally one likes to be in a location where there is easily separable multiunit activity which is responding to the stimulus of interest. With this method, one can place the electrode in the neural tissue and record for a few minutes the responses to a stimulus. The responses can then be sorted so that the experimenter can see how many units he or she is recording and how different their spike shapes are. Ideally, one likes to be in a

location where the spikes arising from different units are as differently shaped as possible. The shape of a spike is dependent upon where the recording electrode is placed relative to the unit and where the spike is generated (Chung et al., 1970; Quiroga, 2009). Thus, with some careful maneuvering, one can be recording from the same set of units and still maximize the differences between the spike shapes.

Spike sorting is of utmost importance in any extracellular recording. Even if one is sure that there is only one large SNR unit responding to the stimuli, putting the collection of spike shapes through a classification algorithm will ensure that there are not more units present which are close to the electrode and responding in a similar fashion. It has been shown that in many systems neighboring neurons respond in similar ways due to shared inputs and overlapping receptive fields (REFS).

It is informative to look at the thresholding results at a moderate MUAFR, for example 70 Hz. This is the MUAFR that is used in Quiroga's paper on his use of the superparamagnetic clustering where he describes the results of both his clustering and his threshold detection (Quiroga et al., 2004). At this MUAFR, my method suffers from around seven extra spikes per second at the lowest SNR. In a SNR=1.5 trace it is very challenging to notice the spikes by eye. Quiroga's threshold detects very few false positives. Turning now to the false negatives, or spikes which are present in the recording but are not detected by the threshold, my threshold will miss, on average, around seven spikes per second again at

most SNR's. Both Quiroga's and the classic threshold suffer greatly at poor SNR. In fact they miss between 20-40% of all spikes, which is quite unacceptable. At moderate to high SNR, all three detection thresholds do quite well.

In assumption (1) above it was stated that we assume that each spike from a given neuron looks identical (without noise), or, put another way, points to the same location in the 64-dimensional parameter space. The noise spreads out the set of points corresponding to a set of spikes from a given unit into a cloud whose distribution can be described by the covariance of the noise. Additionally, due to bursting, the shape of a given unit's spikes will have an inherent variability which will trace out some manifold in parameter space. These factors compound each other and force us to abandon our strict interpretation of our first assumption. Rather, it is better to state that each unit will produce spikes which, when taking into account the noise and variance due to bursting, are more similar to each other than to spikes from other neurons but whose distribution cannot be assumed to be multivariate Gaussian in nature. Thus, it makes more sense to look for locally high density regions in the data as the non-point-like centers of the clusters. This method of superparamagnetic clustering is based on the nearest neighbor interactions, which we limit by defining K above, and so it does not assume that clusters have a low variance, a Gaussian distribution, or are non-overlapping (Quiroga et al., 2004).

In summary, I presented here a new threshold, based on the statistics of the data, which detects a larger percentage of spikes present in neural traces than other thresholds which are currently in common use. I demonstrated that the false positives which are detected by this threshold can be discarded after clustering. The clustering method is a modification of a recently proposed algorithm which uses the local structure of the data to non-parametrically cluster the spike events into groups corresponding to individual units in the neural tissue as well as a cluster of noise and non-separable spike event superpositions.

ACKNOWLEDGEMENTS:

I am very indebted to David Morton for many fruitful discussions about the algorithms and aid in the computations.

REFERENCES:

Bankman IN, Johnson KO, Schneider W. Optimal detection, classification, and superposition resolution in neural waveform recordings. *IEEE Trans on BioMed Eng.* 1993; **40**: 836-841.

Bevington PR, Robinson DK. Data Reduction and Error Analysis for the Physical Sciences. New York NY: McGraw-Hill. 1992.

Blatt M, Wiseman S, Domany E. Data clustering using a model granular magnet. *Neural Computation*. 1997. **9:** 1805-1842.

Blatt M, Wiseman S, Domany E. Superparamagnetic clustering of data. *PhysRevLett.* 1996. **76:** 3251-3254.

Bowyer A. Computing Dirichlet tessellations. *Comput J.* 1981. **24**: 162-166.

Brown EN, Kass RE, Mitra PP. Multiple neural spike train data analysis: state-of-the-art and future challenges. *Nat.NeuroSci*, 2004; **7**: 456-461.

Burrus CS, Gopinath RA, Guo H. Introduction to Wavelets and Wavelet Transforms: A Primer. Upper Saddle River, NJ: Prentice Hall. 1998.

Chung SH, Raymond SA, Lettvin JY. Multiple meaning in single visual units. *Brain,Behav,Evol.* 1970. **3:** 72-101.

Chui CK. Wavelets: A Mathematical Tool for Signal Analysis. Philadelphia, PA: *SIAM.* 1997.

Csicsvari J, Hirase H, Czurko A, Buzsaki G. Reliability and state dependence of pyramidal cell-interneuron synapses in the hippocampus: an ensemble approach in the behaving rat. *Neuron*. 1998. **21**: 179-189.

Du J, Riedel-Kruse IH, Nawroth JC, Roukes ML, Laurent G, Masmanidis SC. High-resolution three—dimensional extracellular recording of neuronal activity with microfabricated electrode arrays. *J. NeuroPhysiol.* 2009. **101 :**1671-1678.

Duda RO, Hart PE, Stork DG. Pattern Classification. New York : Wiley-Interscience. 2006, pp. 34, 124-128, 526-537.

Gray CM, Maldonado PE, Wilson M, McNaughton B. Tetrodes markedly improve the reliability and yield of multiple single-unit isolation from multi-unit recordings in cat striate cortex. *J. Neurosci Meth.* **63:** 43-54.

Grenander U., Szeg¨o G., Toeplitz Forms and Their Applications, University of Calif. Press, Berkeley and Los Angeles, 1958.

Hastings W.K. Monte Carlo sampling methods using Markov chains and their applications. *Biometrika*. 1970. **57**: 97-109.

Hulata E, Segev R, Ben-Jacob E. A method for spike sorting and detection based on wavelet packets and Shannon's mutual information. J.NeuroSciMeth., 2002; **117**: 1-12.

Inglis A., Cruz L., Roe D. L., Stanley H. E., Rosene D. L., & Urbanc B.. Automated identification of neurons and their locations, *Journal of Microscopy,* Vol. 230, Pt 3 2008, pp. 339–352.

Joe B. Three-dimensional triangulations from local transformations. *SIAM J. Stat. Comput.* 1989. **10:** 718-741.

Kim KH, Kim SJ. Neural spike sorting under nearly 0-dB signal-to-noise ratio using nonlinear energy operator and artificial neural-network classifier. *IEEE Trans. On BioMed Eng*. 2000; **47**: 1406-1411.

Letelier JC, Weber PP. Spike sorting based on discrete wavelet transform coefficients. *J. Neurosci Meth*, 2000; **101**: 93-106.

Lewicki MS. A review of methods for spike-sorting: the detection and classification of neural action potentials. *Network*, 1998; **9**: 53-78.

Mallat SG. A theory for multiresolution signal decomposition: the wavelet representation. *IEEE Trans on Pattern Anal and Mach Intel*, 1989; **11**: 674-693.

Marin G, Mpdozis J, Sentis E, Ossandon T, Letelier JC. Oscillatory bursts in the optic tectum of birds represent re-entrant signals from the nucleus isthmi pars parvocellularis. *J. Neuroscience*. 2005. **30:** 7081-7089.

Meister M, Pine J, Baylor DA. Multi-neuronal signals from the retina: acquisition and analysis. *Journal of Neuroscience Methods.* 1994*;* **51**: 95-106.

Mtetwa N, Smith LS. Smoothing and thresholding in neuronal spike detection. *Neurocomputing*, 2006; **69**: 1366-1370.

Pouzat C, Mazor O, Laurent G. Using noise signature to optimize spike-sorting and to assess neuronal classification quality*. J. Neuroscience Methods*, 2002; **122**: 43-57.

Press WH, Teukolsky SA, Vetterling WT, Flannery BP. Numerical Recipes: The art of Scientific Computing, Third Edition. Cambridge: Cambridge University Press. 2007.

Quiroga RQ. What is the real shape of extracellular spikes? *J. NeuroSci Meth.* 2009. **177:** 194-198.

Quiroga RQ, Nadasdy Z, Ben-Shul Y. Unsupervised spike detection and sorting with wavelets and superparamagnetic clustering. *Neural Computation*, 2004; **16**, 1661-1687.

Quiroga RQ, Panzeri S. Extracting information from neuronal populations: information theory and decoding approaches. *Nature Neuroscience*, 2009; **10**, 173-185.

Sahani M, Pezaris JS, Andersen RA. Extracellular recording from adjacent neurons. I: a maximum-likelihood solution to the spike separation problem. *Soc NeuroSci. Abstr.* 1997. **23:** 1546.

Smith LS, Mtetwa N. A tool for synthesizing spike trains with realistic interference. *J.Neurosci.Meth*. 2007; **159**:170-180.

Strang G. Wavelet transforms versus Fourier transforms, *Bull.Amer.Math.Soc*., 1993; **28**: 288-305.

Wang S., Swendsen R.H. Three state anti-ferromagnetic Potts models: A Monte Carlo study. *Phys. Rev. B.* 1990. **42**: 2465 – 2474.

Watson D.F. Computing the n-dimensional Delaunay tessellation with application to Voronoi polytopes. *Comput J*. 1981. **24**: 167-172.

Wolf, U. Comparison between cluster Monte Carlo algorithms in the Ising spin model. *Phys Lett. B*. 1989. **228:** 379-382.

Wu F.Y. The Potts model. *Reviews of Modern Physics*. 1982. **54**: 235-268.

Chapter 3:

ON LONG TIME CONSTANTS IN THE RESPONSES OF NEURONS WITHIN THE NUCLEUS ISTHMI OF THE FROG, *RANA PIPIENS*

ABSTRACT:

The nucleus isthmi (NI) is a compact midbrain structure within non-mammalian vertebrates that provides direct topographic feedback to the optic tectum, the primary destination of sensory efferents. I herein describe the temporal responses of units within the NI of the northern leopard frog, *Rana pipiens*, to dynamic visual stimuli. The frogs were visually stimulated with computer driven simple stimuli. Recordings were taken extracellularly within the NI and spike-sorted to obtain simultaneous recordings of individual units. The responses displayed long delays not readily explainable by the latency of response to the stimulus, nor predictable based on the temporal characteristics of the stimuli. Implications on attention in the frog visual system and on the effects of the feedback on the stream of visual information will be discussed.

INTRODUCTION:

The nucleus isthmi (NI) of the frog, *Rana pipiens*, is a visual center which receives input solely from the ipsilateral optic tectum (OT) (Gruberg et al., 1980; Wang 2003). Some units within the NI project feedback to the same topographic location within the ipsilateral OT from which it received input and a separate set of isthmic neurons project to the contralateral OT, also to the same visuotopic location (Dudkin et al., 2007). There are thus two topographic visual maps within the NI. The NI provides the sole cholinergic projection to the superficial layers of the optic tectum (Desan et al., 1987; Wallace et al., 1990). It has been shown that the feedback projections to the ipsilateral OT are not to the same neurons from which the NI received a projection (Gruberg et al., 1994).

Behaviorally, the nucleus isthmi has been shown to be necessary for the frog to respond to moving stimuli (Gruberg et al., 1991), though the frog can recognize non-moving objects without the OT or NI (Ingle, 1973; Saltzman et al., 2004). Much work has been done describing the responses of the NI units to visual stimuli (Gruberg et al., 1980; Winkowski et al., 2002; Wang, 2003), though the temporal aspects of the responses have yet to be elucidated. The temporal aspects of the responses of the NI may have a profound impact on the nature of feedback. It may act as a winner-take-all mechanism (Lee et al., 1999; Marin et al., 2007; Brandt et al., 2007), direct attention (Reynolds, 2008), control oscillations (Bal et al., 2000), precision to stimuli (Andolina et al., 2007), or other aspects in which temporal parameters in feedback may play a key role (Funke et al., 1997; Bair et al., 2001; Choe, 2004).

In this chapter, I will report the temporal responses of the NI to simple visual stimuli. The stimuli consist of diffuse illumination steps, and moving and looming spots. All responses are recorded extracellularly. The voltage traces are spike sorted allowing me to simultaneously record the responses of multiple units. The responses displayed nontrivially long time constants which are not easily explained by the time course of the stimulation.

METHODS:

Surgery and Preparation:

Adult leopard frogs (2-6 cm from snout to vent, 20-40 gram body weight; Hazen's animal farm, Alburg, VT) were anesthetized by immersion in an aqueous solution of 0.2% 3-amniobenzoic acid, commonly referred to as MS-222, (Sigma Chemical Co., St. Louis) in dechlorinated tap water. Once the frog was fully anesthetized, realized by observing that the buccal breathing motions had ceased, a flap of skin measuring about 1 cm side-to-side and 2 cm along the axis of the frog was removed from just behind the eyes to expose the skull which lies directly above the optic tectum, cerebellum, and the rostral part of the hindbrain. A rectangular patch of the exposed frontal parietal bone of the skull was removed with a Dremmel equipt with a 1 mm spherical bit. A small incision was made into the dura mater, a thin membrane covering the optic tectum, and subadjacent arachnoid allowing the electrode direct access to a 1 cm^2 section of the OT or NI underneath. Cotton was placed within the mouth of the frog to push the eyes up

into the same configuration as an awake and responsive frog. The frog was wrapped in cheese cloth and the cheese cloth was pinned to a sturdy section of foam core insulation. The head was supported 1 cm above the rest of the body and a rod was placed in the mouth and secured to the support to ensure a rigid holding of the frog. The frog was kept moist with a solution of 0.02% MS-222 in aquarium water dripped onto the cheese cloth. In addition, to ensure immobilization during recording, the frog was periodically given an injection of 0.03 ml (per 20 grams body weight) solution of d-tubocurarine chloride (3 mg/ml; Sigma Co., St Louis) into the dorsal lymph sac.

The frog was secured to a rotatable stage for optimal alignment with the recording electrodes and the stimulating monitor. The entire rig was situated within a Faraday cage with a hole cut in the side for the frog to be able to see the visual stimulation monitor. The faraday cage was covered in an opaque black conductive cloth to seal out all ambient light which was not emanating from the stimulation monitor. All surgical procedures were approved by the Washington University Animal Care Facility and were in accordance with the National Institutes of Health and Society for Neuroscience guidelines.

Extracellular recordings:

Borosilicate glass electrodes (A-M Systems, Everett, WA) were filled with Cerrolow-136 (as described in Dowben & Rose, 1953) and electroplated with gold and platinum to obtain an impedance between 50 kΩ - 0.5 MΩ. The signal

was amplified by a gain factor of 1,000 and filtered between 10 - 5,000 Hz with an A-M Systems 1800 amplifier. The signal was connected to a Tektronix TDS 210 oscilloscope and a speaker (AM Systems 3300) and monitored in real time. The signal was sent to the computer via a BNC 2090 A/D board (National Instruments, Austin, TX), and acquired via LabVIEW (National Instruments, Austin, TX) with a sampling rate of 10 kHz and stored for off-line analysis. All data is analyzed off-line in MATLAB (Mathworks) with custom or built-in routines that are available upon request.

The raw voltage signal was smoothed by passing it through a band-pass filter between 300 and 5000 kHz formed with a 4-pole Butterworth filter. Spike events were detected using the threshold previously described (Eggebrecht, 2009). Briefly, the probability distribution of points in the first derivative of the voltage trace is subtracted from the associated Gaussian distribution having the same mean and standard deviation. The positive and negatives values of the zeros of this difference are set as the positive and negative thresholds in the first derivative, respectively. The entire set of recordings from a given electrode placement is used to properly determine this threshold. The detected spike events are then sorted using a superparamagnetic clustering algorithm (Quiroga et al., 2004). The sorting method removes false positives from the set of spikes and checks clustering with the interspike interval distributions.

The electrodes were placed into the frog's left OT with an electric micromanipulator (MP 285, Sutter Instruments). Activity was briefly recorded in

the superficial OT to ensure that the frog was healthy and responsive. The coordinates of the midline of the OT and the caudal pole of the OT were used to determine where to place the electrode for the penetration to the NI. The NI was reliably located between 100 - 1000 μm lateral of the midline, 25 - 200 μm rostral to the caudal pole, and 1050 - 1600 μm ventral to the dorsal surface of the OT (depending on the size of the frog). An incorrect positioning of the electrode was clear if there were auditory responses at a depth where NI responses were expected. If this was the case, the electrode was brought back to the surface and repositioned relative to the caudal pole and midline. Proper placement within the NI was checked by the varying of the receptive field to placement of the electrode: the receptive fields recorded within the NI will move temporal-nasally when the electrode progresses dorsal-ventrally (Gruberg et al., 1978; Gruberg et al., 1980; Winkowski et al., 2002). Microelectrode locations were verified by an electrolytic lesion (-5 μA DC for 5 sec) at the recording site and visualized after fixing the tissue.

Histology:

After the recording session, the frog was anesthetized with the 0.3% MS-222 solution and perfused through the conus arteriosus with a 0.7% NaCl solution followed by a fixative (75 ml 95% ethyl alcohol, 5 ml glacial acetic acid, 5 ml 37% formalin, 15 ml distilled water). The brain was removed and dehydrated through a graded set of alcohol solutions and cleared in cedarwood oil overnight. The brain was embedded in paraffin wax and sectioned transversely (thickness, 15

μm). Serial sections were floated onto distilled water covered albumen/ glycerol coated slides and dried thoroughly overnight on a slide warmer (at 40ºC). The paraffin was dissolved in xylene (Sigma Co., St. Louis). The sections were hydrated, stained with cresyl violet (Sigma Co., St. Louis), then dehydrated and coverslipped.

Visual stimulation:

Once the electrode was properly placed within the NI, the stage was rotated to place the axis of the frog parallel to the stimulation monitor (Samsung 244T LCD monitor: contrast ratio of 1000:1, 24", 1920 X 1200 resolution, 500 cd/m^2 maximum brightness). The frog's right eye was placed facing the monitor at a distance of 6". The receptive fields were mapped out with a laser pointer, or via the computer monitor with a white box on a black background or a black box on a white background each controlled by a mouse. The center of the monitor was aligned with the center of the frog's multi-unit receptive field. All stimuli were presented monocularly to the right eye.

The visual stimulation was presented via the Presentation software package (Neurobiological Systems, Seattle, WA) with custom built routines. The exact timing of the visual stimulus was reported in Presentation and checked with a photodarlington (aimed at the center of the electrically recorded multi-unit receptive field) which sent a signal to the acquisition program. The flicker rate of the monitor was on the order of tens of microseconds. This was two orders of

magnitude faster than stimuli which the frog can respond to and did not interfere with the responses of the neural units from which we were recording.

We presented three main visual stimulations: one-dimensional diffuse illumination flashes, moving spots, and looming spots. The diffuse illumination stimuli consisted of five seconds of a fully bright white screen followed by five seconds of a fully dark screen. This protocol was repeated five times per trial. The moving spot stimuli consisted of a spot appearing static on the screen in one of eight symmetric positions around the visual field. The spot was either 2º or 15º in diameter. After three seconds, the spot moved straight across the visual field center to the opposite location at an average speed of 10 deg/s. The spot then sat motionless on the opposite side of the screen for an additional 4 seconds before the trial ended.

The looming spot is a bit more subtle. We followed the general protocol of Gabbiani et al., 1999 and Sun et al., 1998. The spots were enlarging dark discs on a white background designed to simulate an object approaching the frog on a collision course with constant velocity. The responses to light discs on a dark background were qualitatively very similar and will not be discussed. The time course of the angular size of the spot subtended on the frog's retina is the variable of interest that characterizes the approaching stimuli. Let x denote the position of the spot with respect to the eye of the frog, where $x = 0$ at the time of collision and $x > 0$ on approach. If we define $t = 0$ as the moment of collision

and let $t < 0$ before the collision, then an object on approach with a constant velocity is defined by the equation:

$$x(t) = v \bullet t\,,$$

where v is defined to be negative since it is approaching the origin. The angular size of the object at the retina is given by:

$$\theta(t) = 2 \bullet \tan^{-1}\left(\frac{R}{vt}\right),$$

where R denotes the object's half-size. The half-size on the screen, $l(t)$, is:

$$\tan\left(\frac{\theta(t)}{2}\right) = \frac{l(t)}{d},$$

where d is the actual distance from the screen to the frog's eye. Recall that for our set-up, d =6 cm. The motion of the spot on the retina of the frog can most compactly be expressed by the ratio, β, of the spot's half-size to its apparent approach velocity:

$$\beta = \frac{R}{v}.$$

Note that two different objects, one with twice the size and twice the approach velocity as the other, will have the same value of β, which is in units of time.

We tested the response of the NI with β values of 25 ms and 115 ms. These correspond to a prey-like object of full-size 50 mm (like a cricket, a favored

delicacy for a frog) or a predator-like object of full-size 230 mm (such as a bull frog) moving towards the frog at 1 m/s, or a large hawk measuring 1,610 mm and approaching at 14 m/s.

Data Analysis:

The extracellular recordings were all filtered off-line to separate any local field potential (LFP) components from the high frequency action potentials. The LFP, or low-pass, band was formed by filtering the raw signal between 10 and 300 Hz. The high frequency part used to detect spikes was formed by filtering the raw signal between 300 and 5000 Hz. Spikes were detected and sorted as described above in **Chapter 2**. Average firing rates were formed by binning the spike times into bins of 1 ms, averaging over trials, and convolving with an alpha function equal to:

$$F_{\alpha}(t) = \frac{t}{e^2} e^{-\left(\frac{t}{e}\right)},$$

chosen so that the integral from zero to infinity is equal to one, and so that reasonable firing rates result. This function has a width at half-maximum approximately equal to 11 ms. An alpha function was chosen rather than a Gaussian for the smoothing function to conserve causality; smoothing with a Gaussian spreads the response into both the forward and backwards directions in time; thus it appears that the response actually precedes the stimulus!

Smoothing with an alpha function avoids this problem and retains the actual delay time from visual stimuli to isthmic response.

RESULTS:

Diffuse Illumination

The steady state behavior of units within the NI contains a level of spontaneous activity around 2.23 ± 1.28 Hz ($\mu \pm SD$). In a light environment the level of spontaneous activity (4.78 ± 2.32 Hz) is slightly higher than when in a dark environment (1.68 ± 1.06 Hz). When the frog is presented with strong changes in diffuse illumination, the response is quite different for ON or OFF stimuli (**Fig.3.1**). The top of the figure shows a sample extracellular voltage trace recorded within the NI to first a step up in diffuse illumination (blue to white) followed five seconds later by a strong drop in diffuse illumination (white to blue; time course of illumination change is shown in red bar at bottom of figure). After 50 trials it is clear that the non-trivial time course of the response is highly reproducible.

In response to the ON step (white section in **Fig. 3.1**), all units display a very strong burst of firing lasting less than 100 ms. Following this is more than a second of a response which is lower than the spontaneous average firing rate. On many individual trials this period of no response lasts nearly 1,500 ms. Following this tacit period all units exhibit a strong second wave of activity. For some units this activity reaches less than half of the peak in firing rate immediately following the ON step (units 4 and 5), while for others the second

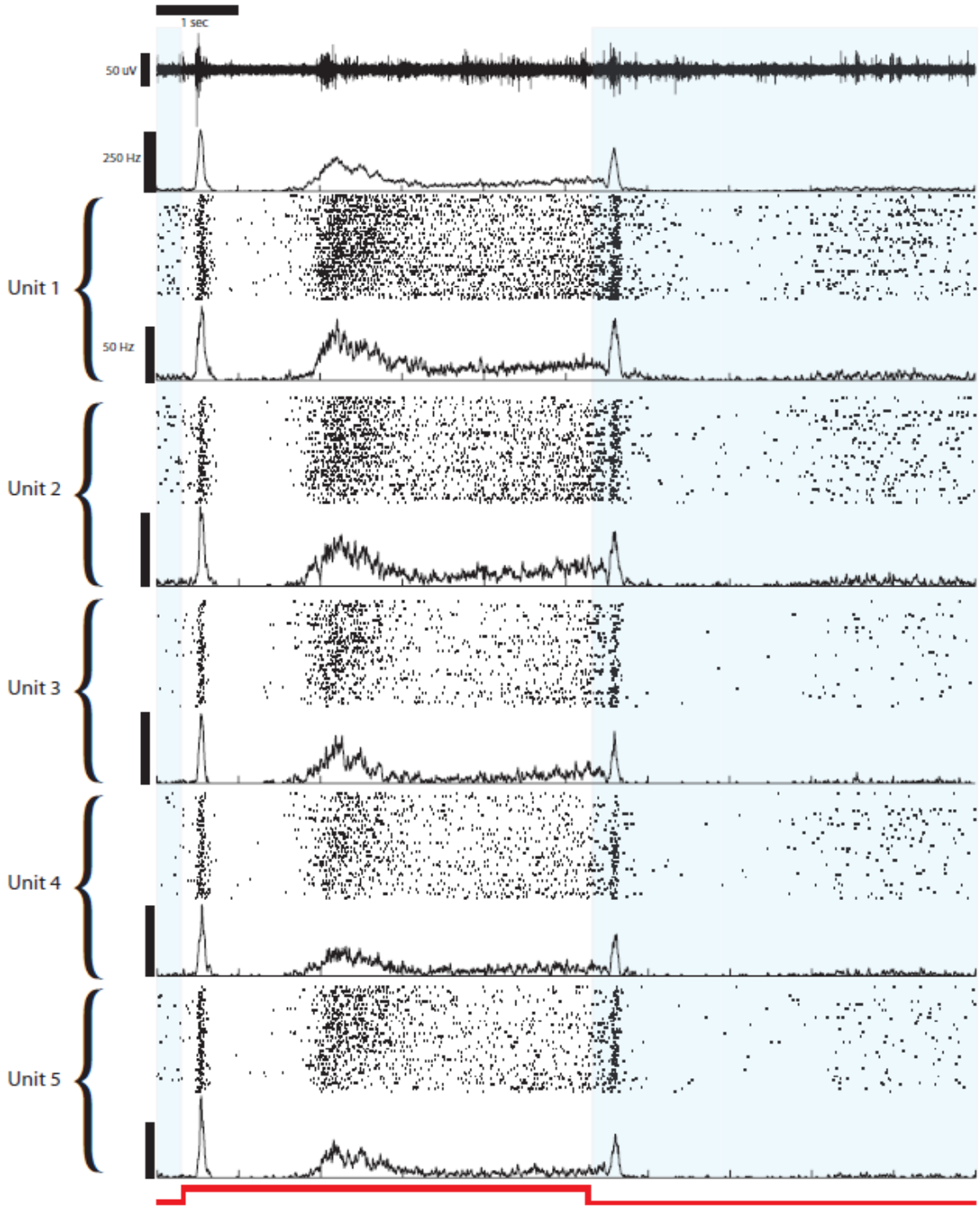

Figure 3.1: Response within the NI to diffuse illumination flashes. Blue section denotes dark environment. White section denotes bright environment. The steps

are 5 sec in length. The red step at the bottom shows the time course for the bright environment and dark environment. There are 50 repetitions of the stimulus. Top trace is a sample raw voltage trace. Below that is the multiunit average firing rate. Below that are the sorted responses showing the 50 trials in raster plots and their respective average firing rates. All scale bars for individual units correspond to 50 Hz. See text for details.

wave of activity reaches a firing rate nearly equal to the initial response (units 1 and 2). This second wave of activity lasts over a second for most units. Note than in some units the second wave of activity actually contains an oscillation in the level of the response (units 3 and 5) with a width of approximately 0.3 seconds. Following this, the activity falls again to spontaneous levels but then resurges yet again in a third, though less strong, wave of activity. This third wave of activity settles back down to the level of spontaneous activity in around 2 seconds (data not shown). Thus, in the NI the response to an ON step contains three waves of activity. The first is very strong and very short, followed by a long period of very low response. The second is also strong but lasts over a full second, with no period of silent activity following. The third wave is a moderate response which returns to the original background level after a few seconds.

In response to the OFF step (blue section in **Fig. 3.1**), units within the NI exhibit a strong initial response which is not as strong as the initial response to the ON stimulus. Following this is a period of low activity. There is no secondary wave of activity in the response to an OFF step. Around one to two seconds following the strong response, the activity returns to the background level. Note

that the latencies for the response to an ON and an OFF step in background illumination are approximately equal and are around 80-120 ms.

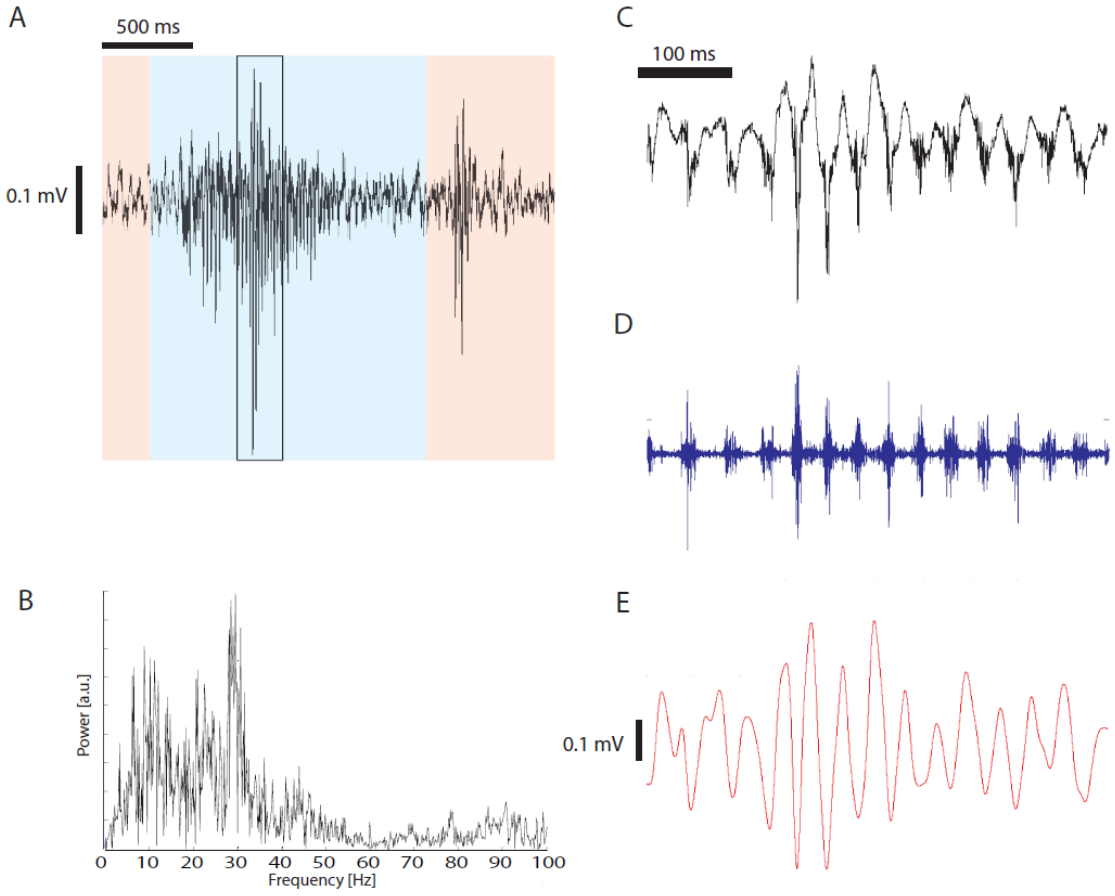

Figure 3.2: Response within the OT to ON and OFF steps of light. (**A)** Raw extracellular recording in OT in response to on OFF step (blue) and an ON step (tan). The OT had only one phase of responses to both ON and OFF stimuli, thus both are shown on a shorter time scale for clarity. **(B)** FFT of data in (A). Note strong peaks around and under 10 Hz and 30 Hz. **(C)** Expansion of section of raw trace within box in (A). Note the presence of periodic bursting. **(D)** Data in (C) passed through a high-pass-filter of frequencies 800-4,000 Hz. **(E)** Data in (C) passed through a low-pass filter of frequencies 10-80 Hz. Scale bare shown in (E) corresponds to all (C), (D), and (E). See text for details.

The primary input to the NI is from the OT. Yet the response within the OT has a very different time course (**Fig. 3.2 A**). The blue section shows the response to an OFF step while the tan section shows the response to an ON step. The response to the OFF step is driven by the RGC type IV axons (the dimming detectors) and has a longer time course than the response to the ON step. Note that there is no secondary wave of activity within the OT in response to either an ON or an OFF step. Also, note that the response to an OFF step is of a longer time course than the isthmic response. A Fourier transform (FFT) of the response in the OT shows a small peak around 3 Hz, some strong peaks around 8-11 Hz, 22-25 Hz, and around 28-32 Hz (**Fig. 3.2 B**). The higher frequency oscillations can be more clearly seen in a detailed in look at the response (**Figs. 3.2 C-E**). **Figure 3.2D** shows the high frequency components of the response by filtering the raw response between 800 and 4,000 Hz. Notice that the spikes are occurring during clearly defined periods with a bursting period of about 30-40 ms, corresponding to the peaks in the FFT centered around 30 Hz. **Figure 3.2E** shows the local field potential in the OT found by filtering the raw signal between 10 and 80 Hz. Note that the spikes in **Figure 3.2D** all occurred during local minima of the local field potential shown in **Figure 3.2E**.

Moving Spot

The response in the NI to moving spots is qualitatively similar regardless of the direction of the movement of the spot. Shown here (**Fig. 3.3**) is the response to a black 15º spot moving in the nasal-temporal direction on a white background.

Responses to a white spot on a dark background are qualitatively similar and are not shown. The tan section denotes that the spot has not yet started its movement. When the white section starts, the spot begins to move across the center of the multiunit receptive field. Note the strong initial response to the commencement of motion. The latency in the response to the beginning of movement is equal to the latency seen above for the initial response to an ON or an OFF step in diffuse illumination, around 80-120 ms. While there is a large difference in the strength of response between the different units, they all responds vigorously to the beginning of the movement and their responses to the steady movement across the visual field are higher than the spontaneous activity.

Trials were also conducted with a 2º spot. The only differences between the responses to a 15º and a 2º moving spot are the firing rate and the direction sensitivity. The firing rate is higher for the larger spot but the time course of all aspects of the response are similar. The direction sensitivity is higher for the larger spot **(Fig. 3.4**), though direction sensitivity was not seen in all units. For a given electrode placement, if any units had some directional preference, then all units had roughly the same level of directional sensitivity. The directional preference observed in **Fig. 3.4** is for a stimulus starting in the superior-nasal part of the visual field moving inferior-temporally.

The most interesting part of the NI response to moving spot actually occurred after the spot stopped moving (**Fig. 3.5**). As before, the white section

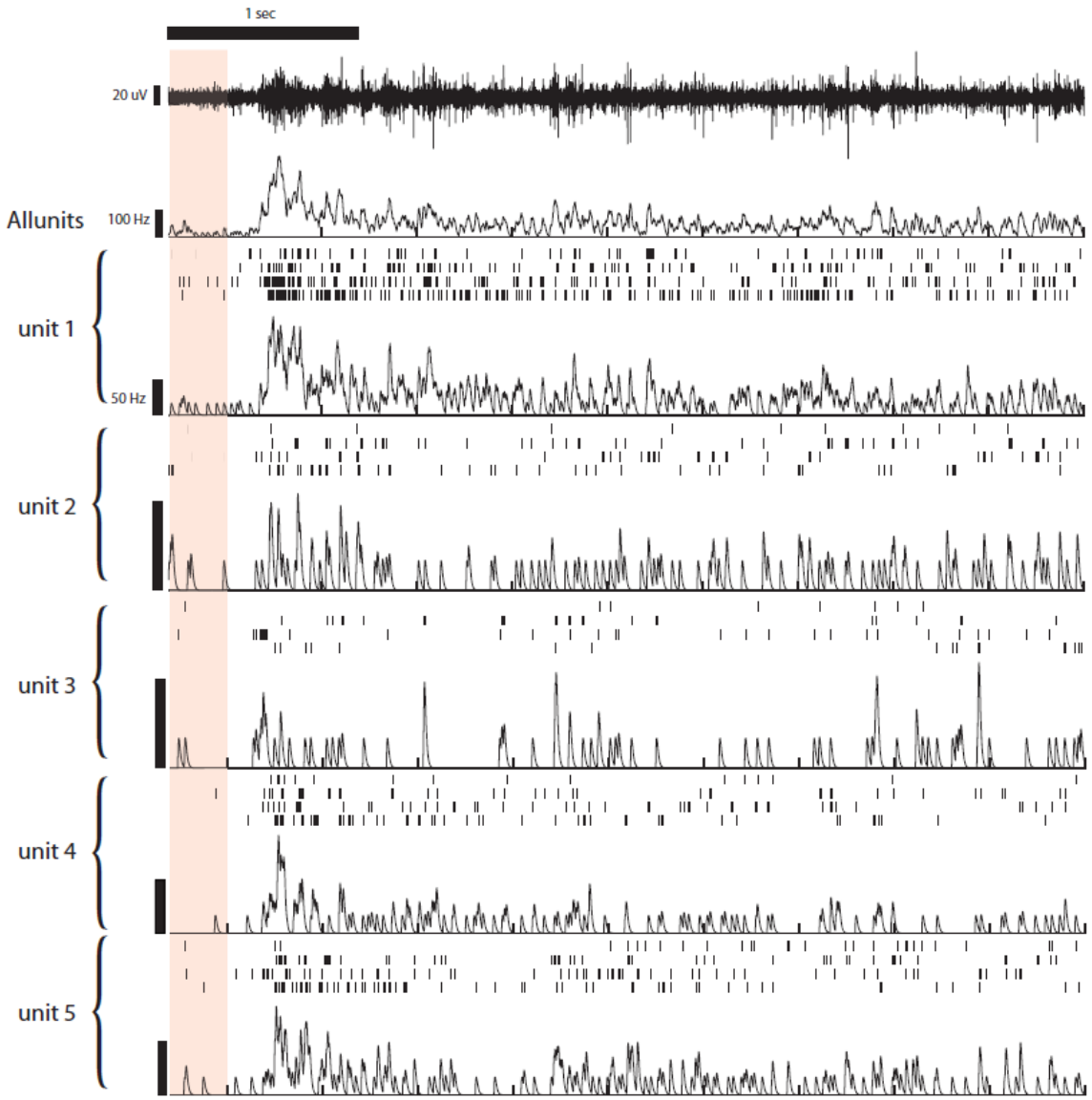

Figure 3.3: Sample response to the start of a moving spot. Tan section denotes that the spot is stationary. The stimulus used was a 15º spot moving nasal-temporally. White section corresponds to time during spot movement. Top trace is a sample raw voltage trace. Below that is the multiunit average firing rate. Below that are the sorted responses showing the 4 trials in raster plots and their respective average firing rates. All scale bars for individual units correspond to 50 Hz. See text for details.

denotes the motion of the spot. The colored section denotes the spot is not moving. The green section represents the usual response latency as determined by the responses to the ON and OFF steps and to the start of motion. Note that there is no strong response at the right edge of the green area where it is expected. Rather, the firing rate stays higher than the spontaneous level for all

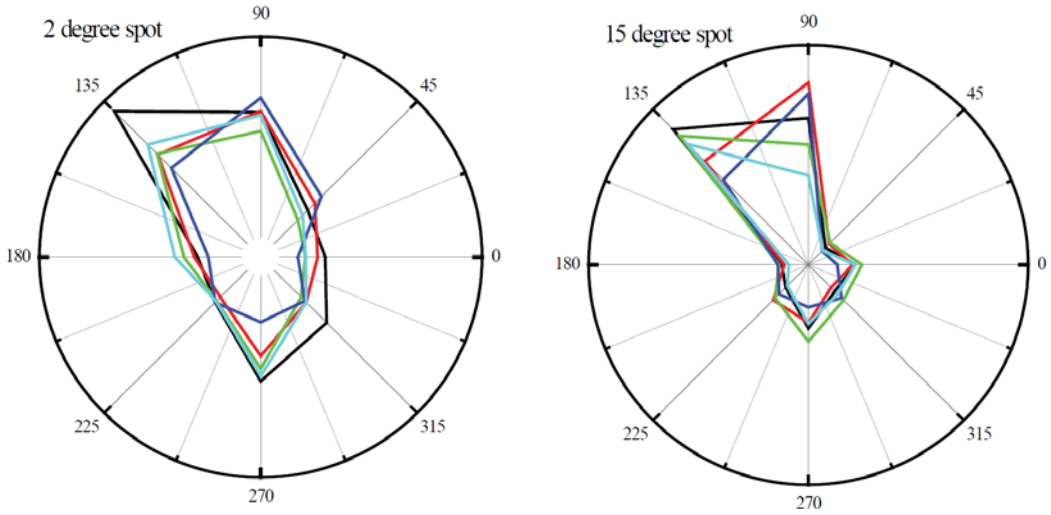

Figure 3.4: Directional sensitivity to a moving spot. Polar plots of the relative response strengths across all simultaneously recorded units in a given penetration. Note that the sensitivity is slightly higher for the larger spot. Also note that all units have similar sensitivities. 90º corresponds to the superior visual field. 180º corresponds to the nasal visual field. Colors represent different units. All units were recorded simultaneously at one location.

units for nearly 1,700 ms until there is a sudden rise in activity. It is important to note that nothing occurred during this time. When the spot stopped moving, it sat within the multiunit receptive field. No immediate response to the cessation of movement was observed for any spot size or for any of the eight tested movement directions. Yet, there is this delayed response to the cessation of the

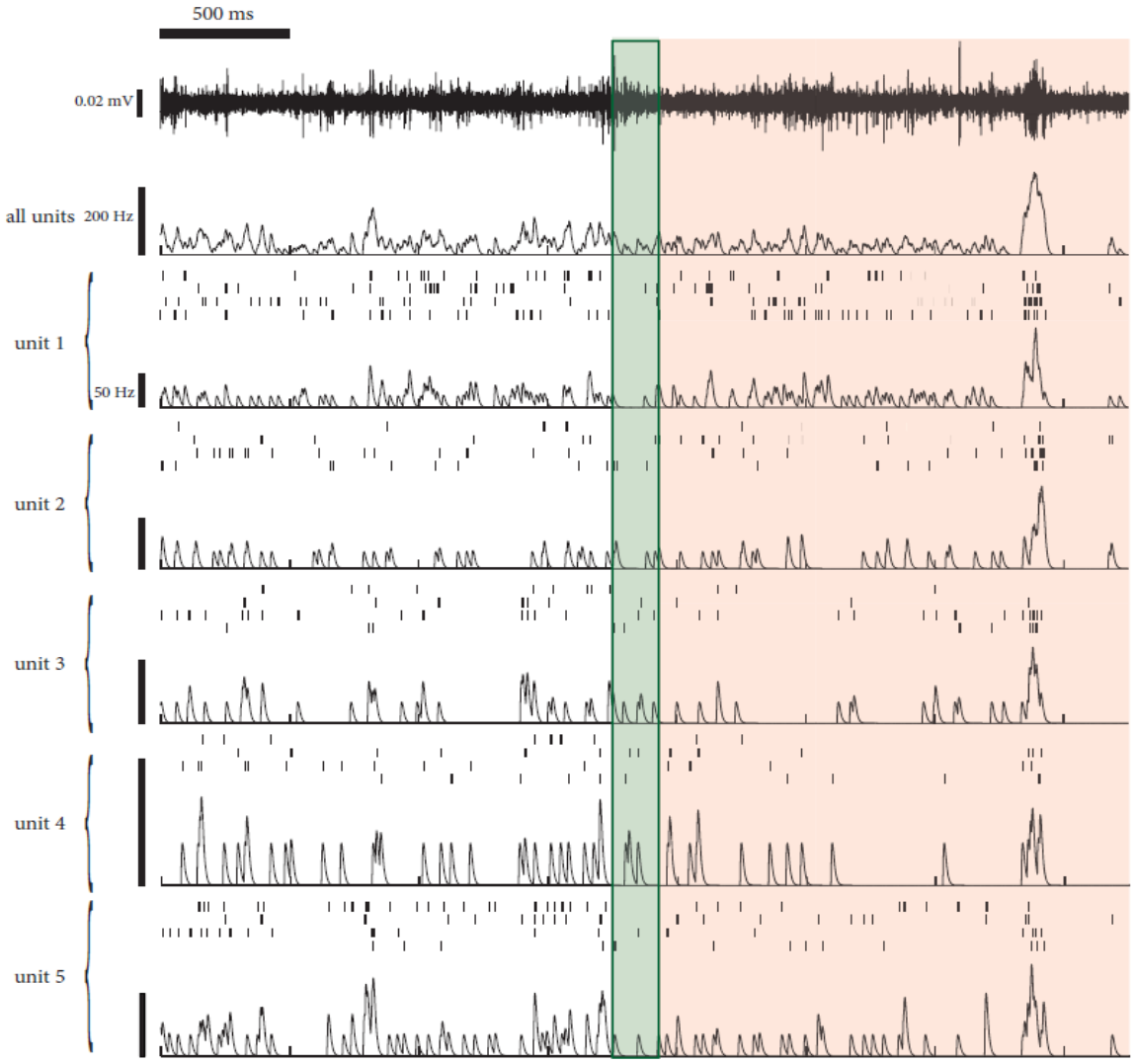

Figure 3.5: Delayed response to cessation of movement. White section denotes movement of spot. Colored section denotes the lack of motion. Width of the green section denotes the expected latency of response given the delay these units had when responding to both a screen flash and the commencement of motion. The tan section denotes the continued lack of motion of the spot on the screen. Top trace is a sample raw voltage trace. Below that is the multiunit average firing rate. Below that are the sorted responses showing the 4 trials in raster plots and their respective average firing rates. All scale bars for individual units correspond to 50 Hz. See text for details.

motion of the spot which takes nearly 1,700 ms to come about. Note that not every unit responded at this point on every trial (see units 3 and 4 in the fourth trial (fourth from the bottom).

Looming Spot

The responses of units within the NI to a looming object are more diverse than to a moving dot or to a diffuse illumination step (**Fig. 3.6**). Some units (units 1, and 5) produced a significantly large firing rate nearly half a second before the collision. The response of these units then dropped significantly before again peaking around the moment of impact. Recall that units within the NI all have a latency of response of between 80-120 ms. Thus, for the response to peak at the time of collision implies that the unit, or the inputs to the unit, had already calculated the trajectory of the looming stimuli. More evidence for this possibility is seen in the response of unit 2. Note that the peak in its response is at or slightly after the moment of collision, whereas other units peak before the collision time (**Fig. 3.7**). It has been shown that the responses of looming sensitive neurons may correlate with variety of different aspects of the stimulus parameters (Hatsopoulos et al., 1995; Sun et al., 1998; Gabbiani et al., 2005). Some responses correlate with the time to impact, others to the angular size (red line in **Fig. 3.6**) others to the angular velocity (blue line in **Fig. 3.6**) of the leading edge of the spot, and others to non-linear combinations of the angular size and the angular velocity. Time-to-impact neurons will begin their primary response at the same moment before the collision is expected regardless of the velocity of

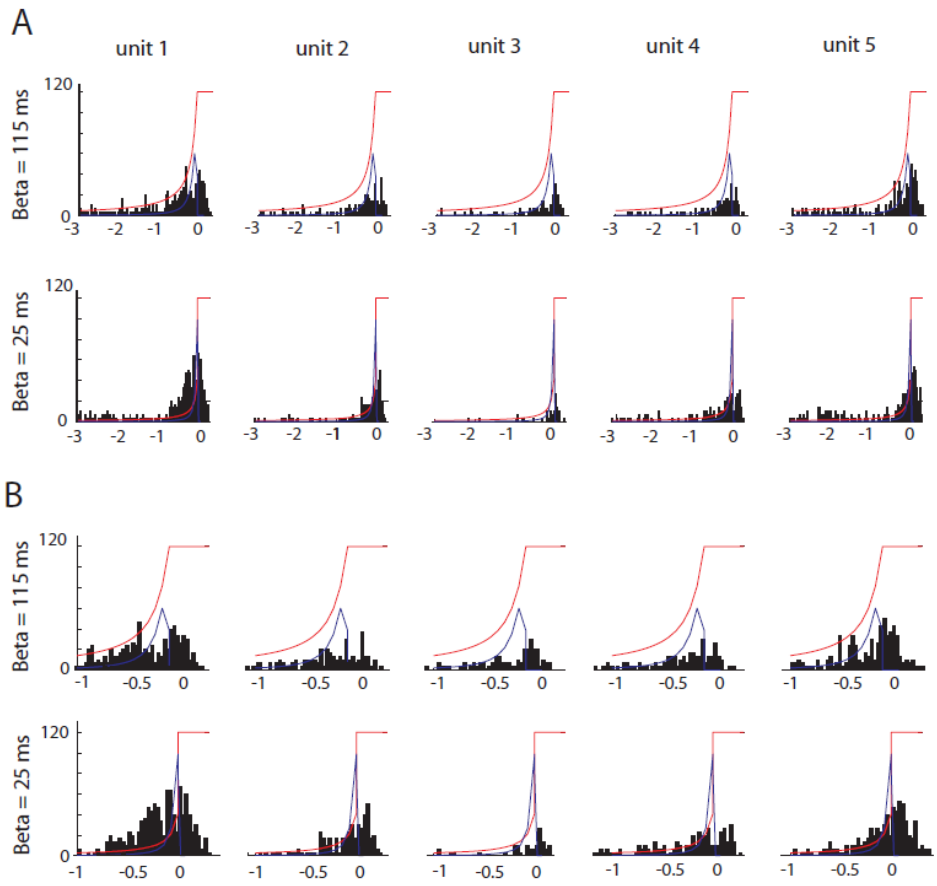

Figure 3.6: Timing of the responses to different looming stimuli. **(A)** The response over the three seconds before collision with the looming object. **(B)** The response over the final second of approach. The firing rate is shown in black in Hz. Bin size for firing rate is 30 ms. Red is the object's angular size in degrees. Blue is the angular velocity in degrees per second. All units use the same scale to the left. Time is in seconds.

the object. Recall that we used β values equal to 25 ms and 115 ms. If these values are for the same object, then the 25 ms value corresponds to an object travelling at 4.6 times faster than the object with β=115. Thus, if an object is responding to a threshold crossing in object size or object angular growth rate, then the response should begin earlier for a slower object. Unit 2 may be a unit

whose onset is determined by the time to impact. Unfortunately, not enough β values were tested to test for trends in these data to test for these possibilities.

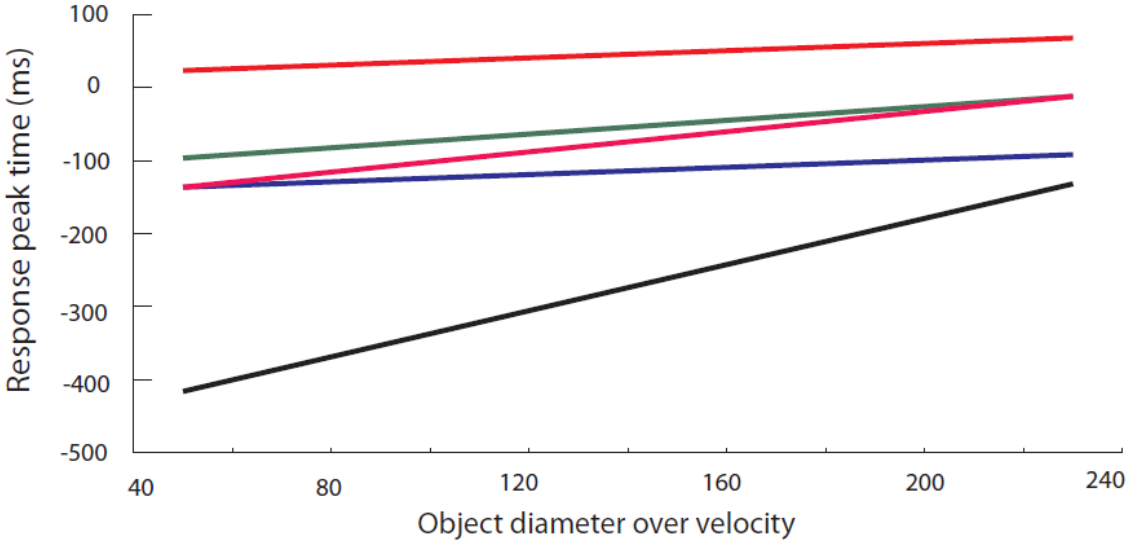

Figure 3.7: Timing of peak in response relative to collision time. Different colors refer to different units. Object diameter over velocity is twice the β value. See text for details.

Zooming in further (**Fig. 3.8**), it is apparent that the responses are quite complicated in the time domain. The responses of units 1, 2, 4, and 5 all appear to peak nearly 200 ms before impact, drop off severely for nearly 50 ms, only to surge back to an overall peak as the object nears collision. Unit 3 peaks in its response 42 ms before collision. Unit 4 actually peaks after the collision. The responses of units 1 and 5 appear to have three primary lobes of activity. These imply some underlying oscillation in the activity of the inputs as was seen in the responses to other stimuli above. This oscillation may be described by the time course of the stimulus. The frame rate of the looming spot was 15 Hz

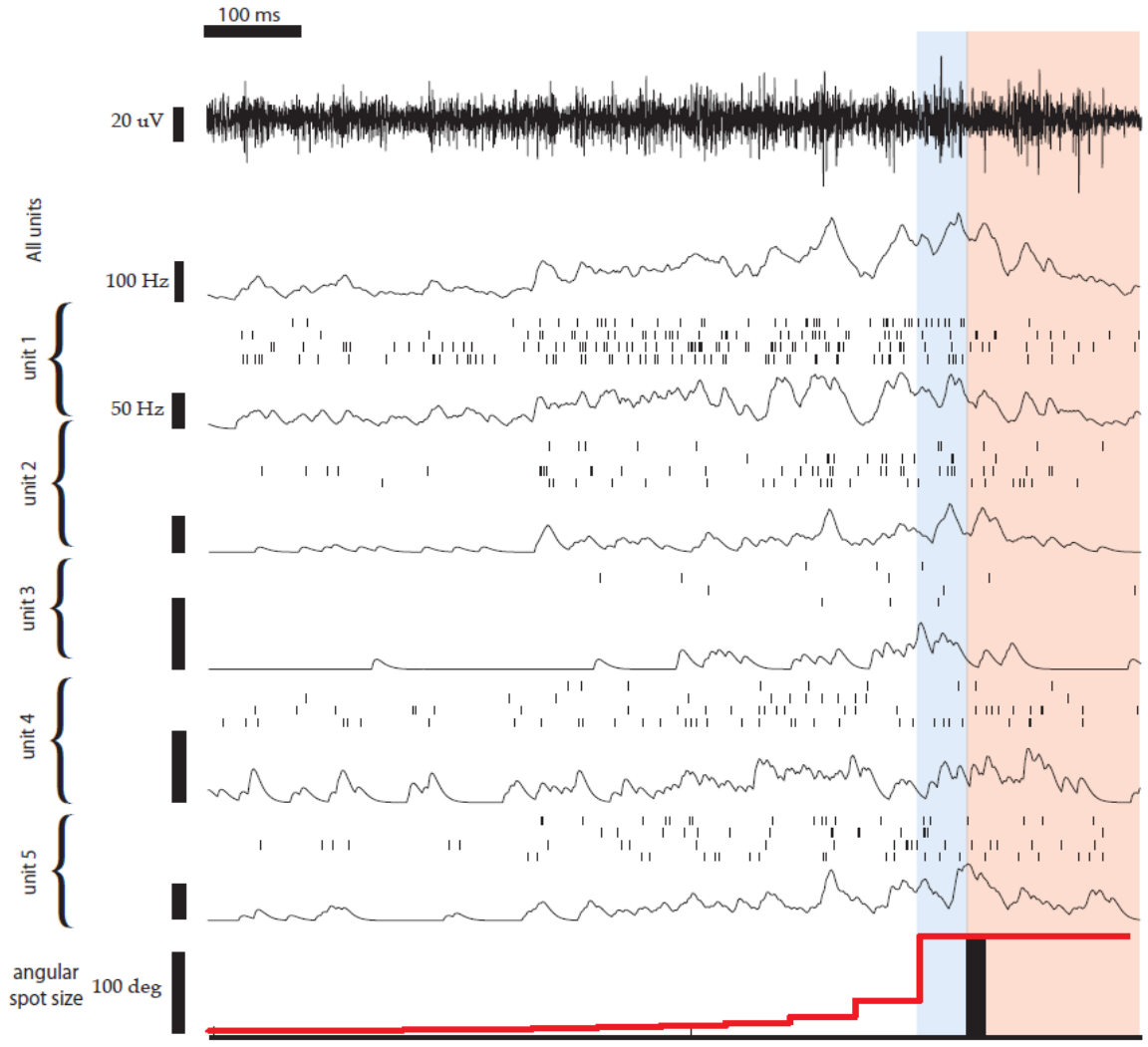

Figure 3.8: Sample response to the start of a looming spot. Black vertical bar at bottom denotes the time of impact. Tan section denotes time after impact. Blue section denotes that the spot has stopped enlarging and its extent is greater than the extent of the multiunit classical receptive field. The stimulus had a β-value equal to 25. White section corresponds to time during looming of spot. Top trace is a sample raw voltage trace. Below that is the multiunit average firing rate. Below that are the sorted responses showing 4of the 10 trials in raster plots and their respective average firing rates. All scale bars for individual units correspond to 50 Hz. See text for details.

corresponding to a frame presentation time of 66.66 ms. This time matches the period of oscillations in the responses of these units. Because of the speed of the approaching object, during the last moments of approach the spot size grows very fast causing the final frames of approach to look more discontinuous than the rest of the stimulus. Thus, it is highly possible that these oscillations are due to the discontinuous nature of the stimulus. They may be in response to the sudden darkening of the screen due to the much larger spot size, or due to jumps in the spot size. A set of control experiments was run in which the whole screen illumination magnitude was progressively changed with the same time course of the looming spot to test if the response was due to the illumination changes or due to the spot size increasing. The oscillations discussed here were not present in the responses to the progressive steps in illumination (data not shown). Thus, it is likely that the oscillations are due to the discontinuous jumps in the size of the spot or in the discontinuous location of the edges of the spot.

DISCUSSION:

I found that the responses of units within the NI have very long time constants in comparison to the time course of the stimuli. This long time course of the response is not seen at the level of the superficial OT. Two of the responses stick out as especially surprising: the secondary wave of activity in response to an ON step in diffuse illumination which follows a 1,500 ms gap in activity, and the 1,700 ms delayed response to the cessation of movement of a moving spot.

While other systems have shown a long and temporally complex response to a diffuse illumination step (Lu et al., 1995; Funke et al., 1997; Worgotter et al., 1999) the nearly two seconds of suppressed response seen here does not appear to be described in the literature. Long delay times have been described within the retina of the rabbit and salamander (Roska et al., 2001; Roska et al., 2006), though these seem to be due to lateral inhibitory interactions. A long delay of a few seconds (Chung et al., 1970) was observed in the dimming detectors of the frog, though this was in response to strong drops in luminosity. There was no such long term behavior in the NI units in response to the OFF step in luminosity.

There are two possibilities for the long period of silent activity and the secondary wave of activity: intrinsic cellular mechanisms and interactions, or network interactions.

Many neurons display lower activity after a strong burst of spiking activity; however, these silent periods are typically around tens to even hundreds of milliseconds long. Periods of quiescence like these are caused by habituation of ion channels which usually recover on shorter time scales. Thus, it seems unlikely that the tacit response is due to intrinsic aspects of the cellular properties.

The other possibility is that network activity caused the silent period and the sudden resurgence. After recovering from a period of hyperpolarization, as

could be caused by a strong inhibitory input, it is normal for a neuron to fire a few spikes. However, the secondary wave of activity is long lasting, nearly two seconds in length. As shown above, in response to an ON step of illumination, there is no secondary activity in the superficial layers of the OT. Could the inhibitory input be arriving from somewhere else? It is possible that there are inputs to the NI which arise from the OT which were not recorded within the superficial OT. Some neurons have been shown to project to the NI which have somata in layers 2 or 4 of the OT. A possible projection from the tegmentum has been described (Udin, 1987) which is composed of a small number of neurons (40 or so). The NI has stained positive for GABA (Li et al., 2001) but it appears inconclusive as to whether or not these locations are in cell bodies of neurons which project to the OT.

The NI in the turtle and the bird all have multiple nuclei. One subnucleus, the Ipc, projects ACh back to the OT in a topographic manner. The other subnucleus, the Imc, projects GABA non-topographically to the OT as well as the Ipc. Thus, it is reasonable to hypothesize that the neurons which may act as the Imc are actually within the NI of the frog along with the neurons which play the part of the Ipc. The NI has already been shown to be cholinergic and it projects back to the OT in a topographic manner. Yet, neither the ipsilateral nor contralateral projection of the NI is nontopographic. There is a possibility that there are intra-isthmic connects in the frog, but as of yet, there is no supporting evidence of this. Some studies have demonstrated that there are gap junctions

(direct electrical connections) between some isthmic neurons within the frog (Wang, 2003; Caudill, personal communication) as there are in the NI of the fish (Northmore, 2003). However, these gap junctions serve to increase the likelihood of simultaneous responses in the NI, but do not explain the long time behavior seen here.

The other surprising result is the delayed response to the cessation of motion of a moving spot. Some units have been previously described in the OT as 'newness' or 'sameness' units (Lettvin et al., 1961). However, the responses seen here in the NI were not observed in early trials within the OT (data not shown). In addition, in his seminal papers of the 1970's (Ingle, 1973; Ingle, 1975) Ingle notes, respectively, that there are multiple pathways for visual information, and that the attention of the frog must be controlled or driven by the tectal system or an element within that system. The units which Lettvin and Ingle found all had longer time constants in their responses and their driving stimulus were very complex. It is possible that a small number of units within the OT, such as those described within these papers, could be driving the delayed responses seen here in response to the stopping of motion. Even so, the long time of the delay is still very puzzling. Assuming a synaptic delay between any two members of a neural circuit of around 10 ms and a conduction time of 100 ms (a very long conduction delay if the spike is not traversing a long distance), there have to be many neurons in the circuit and more than 13 interactions for a single circuit to take nearly 1,500 ms to respond. It is well known that brains

have a global connectivity architecture which can be described by small world and scale-free models (Watts et al., 1998; Clark et al., 2003). These models show that any one neuron is connected to any other neuron in just a few steps, far fewer than 13. Thus, unless a local oscillatory loop is excited by this stimulus, stays active for the nearly two seconds during which there is no change in the NI response, and then suddenly transmits information to the NI unit that something has changed about the stimulus, it is unlikely that the behavior seen here is not intrinsic to the OT or NI.

As for the looming stimuli, there is some evidence that the various responses may correlate with different parameters of the approaching object. Unfortunately, more work will need to be done over a wider variety of β values to be able to determine if within the NI there are units responding to time to impact, or the angular size of the object, or the angular velocity, or to combinations of these parameters. Units have been described in other systems (Hastopoulos et al., 1995; Sun et al., 1998; Gabbiani et al., 1999; Gabbiani et al., 2005) with responses which correlate with a range of parameters of looming stimuli. The results of the present study seem to show that the set of NI responses do appear to be correlated with different aspects of the looming stimuli, but more data is needed. Also, it is unclear as to whether they are themselves responding to the stimuli, or just being driven by OT units which are responding to the stimuli and then sending their output to the NI.

The temporal aspects of a feedback loop profoundly impact the functional implications for the feedback loop (Brandt et al., 2007). This study has shown that the temporal aspects of the NI response display very long time constants. This is a further step in elucidating how the NI feedback to the visual circuitry within the superficial OT affects the processing of visual information. The differing responses to looming stimuli may imply that there is some feature extraction occurring within the isthmi which focuses more greatly its affects within the OT (Gabbiani et al., 1996). The NI could be focusing a beam of attention in the superficial OT controlling the network (Marin et al., 2007). This coupled with the asymmetries seen in the anatomical feedback connections (Dudkin et al., 1999) is strong evidence that the NI–OT system is working as a winner-take-all mechanism. The NI projections may not be forming synapses directly onto tectal projection neurons, as was implied by some papers (Wang et al., 2003), but rather releasing the ACh via a paracrine mechanism in the superficial OT (Rybicka et al., 2005). This affects not only the RGC input to the OT, but also affects the responses of the plethora of interneurons within the superficial OT, most of which are GABAergic. Also, ACh has been shown to differentially affect the postsynaptic neuron (Antal et al., 1986); the effects may be either inhibitory or excitatory depending on the cellular properties of the postsynaptic cell. This leads indirectly to the excitatory as well as inhibitory action of NI stimulation onto OT responses as seen previously (Antal et al., 1986; Hoshino et al., 2006).

REFERENCES:

Andolina IM, Jones HE, Wane W, Sillito AM. Coritcothalamic feedback enhances stimulus response precision in the visual system. *PNAS*. 2007. **104**: 1685-1690.

Antal M, Matsumoto N, Szekely G. Tectal neurons of the frog: intracellular recordings and labeling with cobalt electrodes. *J Comp. Neurology*. 1986. **246**: 238-253.

Bair W, Zohary E, Newsome WT. Correlated firing in macaque visual area MT: time scales and relationship to behavior. *J Neurosci*. 2001. **21**: 1676-1697.

Brandt SF, Wessel R. Winner-take-all selection in a neural system with delayed feedback. *Biol Cybern*. 2007. **97**: 221-228.

Choe Y. The role of temporal parameters in a thalamocortical model of analogy. *IEEE Trans on Neural Nets*. 2004. **15**: 1071-1082.

Chung S, Raymond SA, Lettvin JY. Multiple meaning in single visual units. *Brain Behav Evol.* 1970. **3**: 72-101.

Clark, J.W., Eggebrecht, A.T., The small world of the nobel nematode Caenorhabditis elegans. In: da Providencia, J., Malik, F.B. (Eds.), Condensed Matter Theories. 2003. vol. 18, Nova Science Publishers, Hauppauge, NY..

de la Rocha J, Doiron B, Shea-Brown E, Josic K, Reyes A. Correlation between neural spike trains increases with firing rate. *Nature*. 2007. **448**: 802-806.

Desan PH, Gruberg ER, Grewell KM, Eckenstein F. Cholinergic innervations of the optic tectum in the frog *Rana pipiens*. *Brain Research*. 1987. **413**: 344-349.

Dowben RM, Rose JE. A metal-filled microelectrode. *Science* 1953. **118:** 22-24.

Dudkin EA, Sheffield JB, Gruberg ER. Combining visual information from the two eyes: the relationship between isthmotectal cells that project to ipsilateral and to contralateral optic tectum using fluorescent retrograde labels in the frog, *Rana pipiens*. *J. Comp. Neurol*. 2007. **502**: 38-54.

Dudkin ES, Gruberg ER. Relative number of cells projecting from contralateral and ipsilateral nucleus isthmi to loci in the optic tectum is dependent on visuotopic location: horseradish peroxidase study in the leopard frog. *J. Comp. Neurol*. 1999. **414**: 212-216.

Funke K, Worgotter F. On the significance of temporally structured activity in the dorsal lateral geniculate nucleus (LGN). *Preog in Neurobio*. 1997. **53**: 67-119.

Gabbiani F, Metzner W, Wessel R, Koch C. From stimulus encoding to feature extraction in weakly electric fish. *Nature*. 1996. **384**: 564-567.

Gabbiani F, Krapp HG, Laurent G. Computation of object approach by a wide-field, motion sensitive neuron. *J Neurosci*. 1999. **19**: 1122-1141.

Gabbiani F, Cohen I, Laurent G. Time-dependent activation of feed-forward inhibition in a looming sensitive neuron. *J. Neurophysiol*. 2005. **94**: 2150-2161.

Gruberg ER, Udin SB. Topographic projections between the nucleus isthmi and the tectum of the frog, *Rana pipiens*. *J Compar. Neurol.* 1978. **179**: 487-500.

Gruberg ER, Lettvin JY. Anatomy and physiology of a binocular system in the frog *Rana Pipiens*. *Brain Research.* 1980. **192**: 313-325.

Gruberg ER, Wallace MT, Caine HS, Mote MI. Behavioral and physiological consequences of unilateral ablation of the nucleus isthmi in the leopard frog. *Brain Behav Evol*. 1991. **37**: 92-103.

Gruberg ER, Hughes TE, Karten HJ. Synaptic interrelationships between the optic tectum and the ipsilateral nucleus isthmi in *Rana pipiens*. *J. Comp. Neurol*. 1994. **339**: 353-364.

Hatsopoulos N, Gabbiani F, :Laurent G. Elementary computation of object approach by a wide-field visual neuron. *Science*. 1995. **270**: 1000-1003.

Hoshino N, Tsurudome K, Nakagawa H, Matsumoto N. Current source density analysis of contra- and ipsilateral isthmotectal connections in the frog. *Vis Neurosci*. 2006. **23**: 713-719.

Ingle D. Two visual systems in the frog. *Science*. 1973. **181**: 1053-1055.

Ingle D. Disinhibition of tectal neurons by pretectal lesions in the frog. *Science*. 1973. **180**: 422-424

Ingle D. Focal attention in the frog: behavioral and physiological correlates. Science. 1975. **188**: 1033-1035.

Lee DK, Itti L, Kock C. Braun J. Attention activates winner-take-all competition among visual filters. *Nature*. 1999. **2**: 375-381.

Lettvin JY, MAturana HR, Pitts WH, McCulloch WS. Two remarks on the visual system of the frog. in Sensory Communication. Cambridge Massachusettes. The MIT Press. 1961. 757-776.

Li Z, Fite KV. GABAergic visual pathways in the frog, *Rana pipiens*. *Vis. Neurosci*. 2001. **18**:457-464.

Lu SM, Guido W, Vaughn JW, Sherman SM. Latency variability of responses to visual stimuli in cells of the cat's lateral geniculate nucleus. *Exp Brain Res*. 1995. **105**: 7-17.

Marin G, Salas C, Sentis E, Rojas X, Letelier JC, Mpodozis J. A cholinergic gating mechanism controlled by competitive interactions in the optic tectum of the pigeon. *J Neurosci.* 2007. **27**: 8112-8121.

Northmore DPM, Gallagher SP. Functional relationship between nucleus isthmi and tectum in teleosts: synchrony but no topography. *Vis. Neurosci.* 2003. **20**: 335-348.

Reynolds JH. Mapping the microcircuitry of attention. *Nature Neurosci*. 2008. **11**: 861-862.

Saltzman H, Zacharatos M, Gruberg ER. Recognition of apertures in overhead transparent barriers by leopard frogs. *Brain Behav. Evol*. 2004. **64**: 11-18.

Sun H, Frost BJ. Computation of different optical variables of looming objects in pigeon nucleus rotundus neurons. *Nature Neurosci*. 1998. **1**:296-303.

Udin SB. A projection from the mesencephalic tegmentum to the nucleus isthmi in the frogs *Rana pipiens* and *Acris crepitans*. *Neuroscience*. 1987. **21**: 631-637.

Wallace MT, Ricciuti AJ, Gruberg ER. Nucleus isthmi: its contribution to Tectal acetylcholinesterase and choline acetyltransferase in the frog *Rana pipiens*. *Neuroscience*. 1990. **35**: 627-636.

Wang SR. The nucleus isthmi and dual modulation of the receptive field of tectal neurons in non-mammals. *Brain Res. Rev*. 2003. **41**: 13-25.

Watts, D.J.; Strogatz, S.H. Collective dynamics of small-world networks. *Nature* 1998 **393**: 409–10

Winkowski DE, Gruberg ER. The representation of the ipsilateral eye in nucleus isthmi of the leopard frog, *Rana pipiens*. *Vis Neurosci*. 2002. **19**: 669-679.

Winkowski DE, Gruberg ER. Superimposed maps of the monocular visual fields in the caudolateral optic tectum in the frog, Rana pipiens. *Vis. NeuroSci.* 2005**. 22:** 101-109.

Worgotter F, Suder K, Funke K. The dynamic spatio-temporal behavior of visual responses in thalamus and cortex. *Restorative Neurology and Neurosci*. **1999**. 15: 137-152.

Zohary E, Shadlen MN, Newsome WT. Correlated neuronal discharge rate and its implications for psychophysical performance. *Nature*. 1994. **370**: 140-143.

Chapter 4:

ON RESPONSES DUE TO CONTEXTUAL INTERACTIONS

ABSTRACT:

Feedback loops have been implicated in affecting contextual interactions in visual systems. The nucleus isthmi is a visual center which shares reciprocal direct topographic connections with the optic tectum. Previous studies have shown that in some systems the isthmi mediates novelty detection or a winner-take-all mechanism, by preferentially selecting new or more salient features of the visual scene, respectively. The winner-take-all mechanism has been shown to be asymmetric in the bird, favoring stimuli in the superficial visual field. Also, the frog has been shown to have a directional preference for ground level nasally placed prey-type stimuli when presented with multiple options simultaneously. Thus, the frog demonstrates a clear asymmetry in its responses to visual stimuli. To investigate a possible connection, units within the nucleus isthmi of the frog, *Rana pipiens*, were presented with multiple visual stimuli inside and outside their receptive fields. The responses to stimuli presented simultaneously both inside and outside of the receptive field were counter intuitively higher than responses to a lone stimulus within the receptive field. This evidence supports the notion that the isthmotectal system of the frog is working as an asymmetric winner-take-

all system as the feedback loop has been suggested to do in other systems. In addition, the isthmic response contains periodic oscillatory bursts which are not of the same frequency components as the stimulus. A model is presented to determine where from these oscillations may be arising.

INTRODUCTION:

Visual context shapes perception and behavior. Attention enhances and modulates processing of sensory input to the brain (Posner, 1980; Gilbert et al., 2007). In many areas, attending to a location in a region of space suppresses responses to stimuli outside of that region while enhancing responses to stimuli presented within the attended space (Desimone et al., 1995; Maunsell et al., 2002; Witten et al., 2006). This modulation most likely acts on many neuronal levels within neural architecture (Deco et al., 2002).

It has been shown that the optic tectum (OT) and the nucleus isthmi (NI) work together to participate in novelty detection and possibly may work as a winner-take-all mechanism (Wang, 2003; Marin et al., 2007; Brandt et al., 2007). While much work has been done to characterize the electrophysiological responses to visual stimuli within the NI of the frog (Gruberg et al., 1980; Winkowski et al., 2002; Wang, 2003), the affects of multiple stimuli have only been investigated behaviorally (Stull et al., 1998).

Here we present the frog with stimuli within, outside, or both with and outside of the receptive field to investigate how the context of a stimulus affects

the response. We recorded extracellularly within the NI and sorted the voltage trace to obtain simultaneous recordings of individual NI units to the stimuli. Surprisingly, the addition of a stimulus external to the receptive field caused the responses to go up in all units studied. Also, the responses to the stimuli contained oscillations in the average firing rates which were in register across all units.

METHODS:

The surgery and preparation, extracellular recordings, and histology were all performed as described in the **Chapter 3**.

Visual Stimulation

The general set-up was that same as described in **Chapter 3**. The stimulation was composed of a picture of a cricket moving with Brownian motion on a white background. The cricket measured approximately 2º by 10º as seen by the eye of the frog. The Brownian motion was constrained in a circle whose diameter was half the screen size of the cricket. The randomness of the Brownian motion was frozen in so that the movements were identical for each trial. The frame rate of the cricket stimuli was 15 Hz; thus each 66.66 ms the cricket assumed a new position on the screen. The optical properties of the movement of the cricket made it seem that the cricket was jittering around a small area to the side of the frog, matching a stimulus which has been shown to excite large responses by the frog (Lettvin et al., 1959; Maturana et al., 1960).

The contextual interaction was tested using three stimulus paradigms (**Fig. 4.1A)**. In the single cricket case, a cricket was placed in the middle of the multiunit receptive field (MURF). The MURF field was mapped out using a laser pointer or a 2º white box on a black background or a 2º black box on a white background controlled by the stimulating computer. In a second single cricket case, the cricket was placed 30º temporal to the center of the MURF. The third case, the double cricket case, had both crickets moving simultaneously in independent random motions.

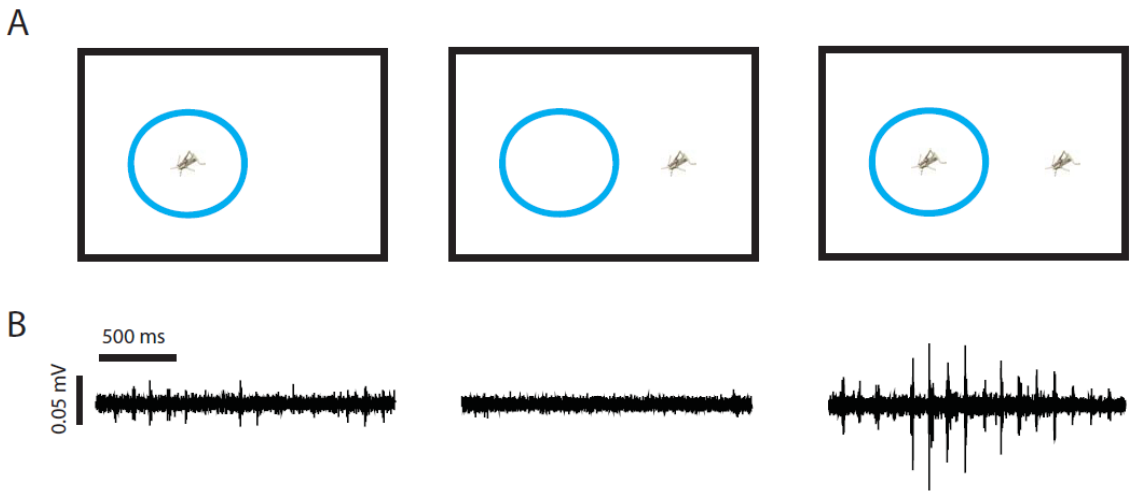

Figure 4.1: (A) Stimulus paradigms with **(B)** multiunit raw voltage responses. **LEFT**: Single cricket within the mapped out MURF (blue circle). **CENTER**: Single cricket 30º temporal to the middle of the MURF. **RIGHT**: "Double cricket" stimulus with both crickets presented simultaneously.

Data Analysis

Fourier transforms (FFT) were computed with the unsmoothed average firing rates with the bin size set to 1 ms. No qualitative difference was observed when

varying the number of trials contributing to the FFT. Auto- and cross-correlations were computed with the unsmoothed average firing rates and a bin size of 10 ms, unless stated otherwise. No significant change was observed in the correlations when using a bin size between 4 - 20 ms. Inter-spike-intervals (ISI) are defined such that: $ISI_n = t_n - t_{n-1}$, where t_n is the time of the n^{th} spike. The joint-ISI distribution is a set of pairs, (ISI_n, ISI_{n-1}), plotted here on a log-log scale to show the long-time course in the spiking patterns of the units.

The Model

We also created a model to try to understand how the population activity within the NI can be responding with waves of nearly synchronous firing. The network consists of two layers of neurons, one presenting the OT and the other presenting the NI. Each layer has 200 neurons that are modeled as leaky-integrate-fire neurons with spike rate adaptation. Therefore the membrane potentials of the OT neuron V_i and nucleus isthmi (NI) V_j evolve according the following equation sets before reaching the spike threshold:

$$\tau_{m,OT}\frac{dV_i}{dt} = E_{r,OT} - V_i - R_{m,OT}(I_{sra,i} + I_{NI\to i} - I_{e,i} + \chi_i),$$

$$\tau_{m,NI}\frac{dV_j}{dt} = E_{r,NI} - V_j - R_{m,NI}(I_{sra,j} + I_{OT\to j} + \chi_j) \quad ,$$

where neurons in the OT are referred using subscript i and neurons in the NI are referred using subscript j. Whenever the membrane potential reaches a

threshold value $V_{\theta,OT/NI}$ it is reset to a value $V_{reset,OT/NI}$ and a spike is interpreted. $E_{r,OT}$ and $E_{r,NI}$ are the resting membrane potentials of OT and NI respectively. The membrane time constants are $\tau_{m,OT}$ and $\tau_{m,NI}$, and the membrane resistances are. $R_{m,OT}$ and $R_{m,NI}$.

The parameters for the OT are adopted from the chicken layer 10 neurons and NI neurons are modified from chicken lpc neurons with $R_{m,NI}=1007$ MΩ and $\tau_{m,NI}=132$ ms (Jing et al. 2009). All parameters have been determined experimentally. The frog values have been measured intracellularly by Mathew Caudill, a member of the group, and are presented in **Chapter 5** below. Layer 10 shepherd's crooks neurons from the chicken OT are used for two reasons. First, the OT neurons which project to the NI in frogs have not been fully electrophysiologically characterized. Also, they perform parallel functions within the two systems, projecting a narrow dendritic tree into the retino-recipient layers of the OT, and projecting an axon off of the dendritic tree to the ipsilateral OT (Lazar et al., 1967; Woodson et al., 1991; Wang et al., 2006).

Neurons in both populations have a spike rate adaptation current I_{sra} (the subscriptions are not included for simplicity), which is described by:

$$I_{sra}=g_{sra}(V-E_{sra}),$$

$$\tau_{sra}\frac{dg_{sra}}{dt}=-g_{sra},$$

where E_{sra} is the adaptation reversal potential, g_{sra} is the spike rate adaptation conductance, and τ_{sra} is the adaptation time constant. Before a spike occurs, the adaptation conductance decays according to the previous equation and when a spike happens the adaptation conductance is changed by

$$g_{sra}(t^+) \rightarrow g_{sra}(t^-) + \Delta g_{sra} \ .$$

Tectal neurons receive isthmic synaptic feedback $I_{NI \rightarrow i}$ that is described by:

$$I_{NI \rightarrow i} = \sum_j \ g_{NI \rightarrow OT} \ P_{ij}(t) \, W_{ij} \ (V_i - E_{NI \rightarrow OT})$$

where $g_{NI \rightarrow OT}$ is the maximum synaptic conductance and $E_{NI \rightarrow OT}$ is the synaptic reversal potential. We choose $g_{NI \rightarrow OT} = 3.12 \times 10^{-2}$ nS and $E_{NI \rightarrow OT} = -5$ mV. The open probability of synaptic conductance P_{ij} has the form:

$$P_{ij}(t) = B_{NI \rightarrow OT} \sum_k \left(\exp(-\frac{t - t_j^k}{\tau_{1,NI \rightarrow OT}}) - \exp(-\frac{t - t_j^k}{\tau_{2,NI \rightarrow OT}}) \right),$$

$$B_{NI \rightarrow OT} = \left(\left(\frac{\tau_{2,NI \rightarrow OT}}{\tau_{1,NI \rightarrow OT}} \right)^{\tau_{rise,NI \rightarrow OT} / \tau_{1,NI \rightarrow OT}} - \left(\frac{\tau_{2,NI \rightarrow OT}}{\tau_{1,NI \rightarrow OT}} \right)^{\tau_{rise,NI \rightarrow OT} / \tau_{2,NI \rightarrow OT}} \right)^{-1},$$

where, $B_{NI \rightarrow OT}$ is the normalization factor. To ensure that the peak value of $P_{NI \rightarrow i}$ generated by a single spike is equal to 1, a summation is performed over all spikes generated by the NI neuron where the variable t_j^k represents the time at which the j^{th} NI neuron generates the k^{th} spike. The time constants $\tau_{1,NI \rightarrow OT}$ and $\tau_{2,NI \rightarrow OT}$ ($\tau_{1,NI \rightarrow OT} > \tau_{2,NI \rightarrow OT}$) determine the time course of the synaptic conductance change. The synaptic rise time is $\tau_{rise,NI \rightarrow OT} = \frac{\tau_{1,NI \rightarrow OT} \tau_{2,NI \rightarrow OT}}{\tau_{1,NI \rightarrow OT} - \tau_{2,NI \rightarrow OT}}$, and $\tau_{1,NI \rightarrow i}$ represents the fall time. We choose a Gaussian function for the weight matrix distribution which has the form:

$$W_{ij} = \exp\left(-\frac{(i-j)^2}{2\Delta_{NI\to OT}^2}\right),\ \Delta_{NI\to OT} = 20.$$

This reflects the fact that the isthmotectal feedback is topographic. The synaptic currents from OT to NI $I_{OT\to j}$ share the same formula as that of $I_{NI\to i}$ and may be acquired by replacing the subscription NI to OT and i to j in the above equations.

In addition to the synaptic input from NI, the OT also receive excitatory current input $I_{e,i}$, mimicking the retinal ganglion cell input, which has form:

$$I_{e,i} = I_0 H(i-60)H(140-i),$$

$$I_0 = 0.1\frac{(\sin(2\pi f_1 t)+1)(\sin(2\pi f_2 t)+1)}{4},$$

where, f_1=9 Hz and f_2=0.6 Hz, respectively, and H is the Heaviside step function, expressing that the current between neuron # 60 and neuron # 140 is non-zero.

To simulate the spontaneous activity, each OT and NI neuron receives uncorrelated noise currents χ_i and χ_j. The noise currents are modeled as uncorrelated white noise:

$$\langle \chi_i(t)\chi_{i'}(t')\rangle = 2\sigma_{OT}^2\delta(t-t')\delta_{ii'},$$

$$\langle \chi_j(t)\chi_{j'}(t')\rangle = 2\sigma_{NI}^2\delta(t-t')\delta_{jj'},$$

with σ_{OT} =0.1 nA since the OT shows relatively small spontaneous activity (data not shown) and σ_{NI} =0.3 nA so that NI neurons will have 2-5 Hz spontaneous activity as observed experimentally and shown in **Chapter 3**.

RESULTS:

In response to a single cricket moving within the center of the multiunit receptive field, all of the units followed the same time course (**Fig. 4.2A**). There was periodic oscillatory bursting in which all units fire in a probabilistic phasic manner, contributing anywhere from zero to three spikes per burst.

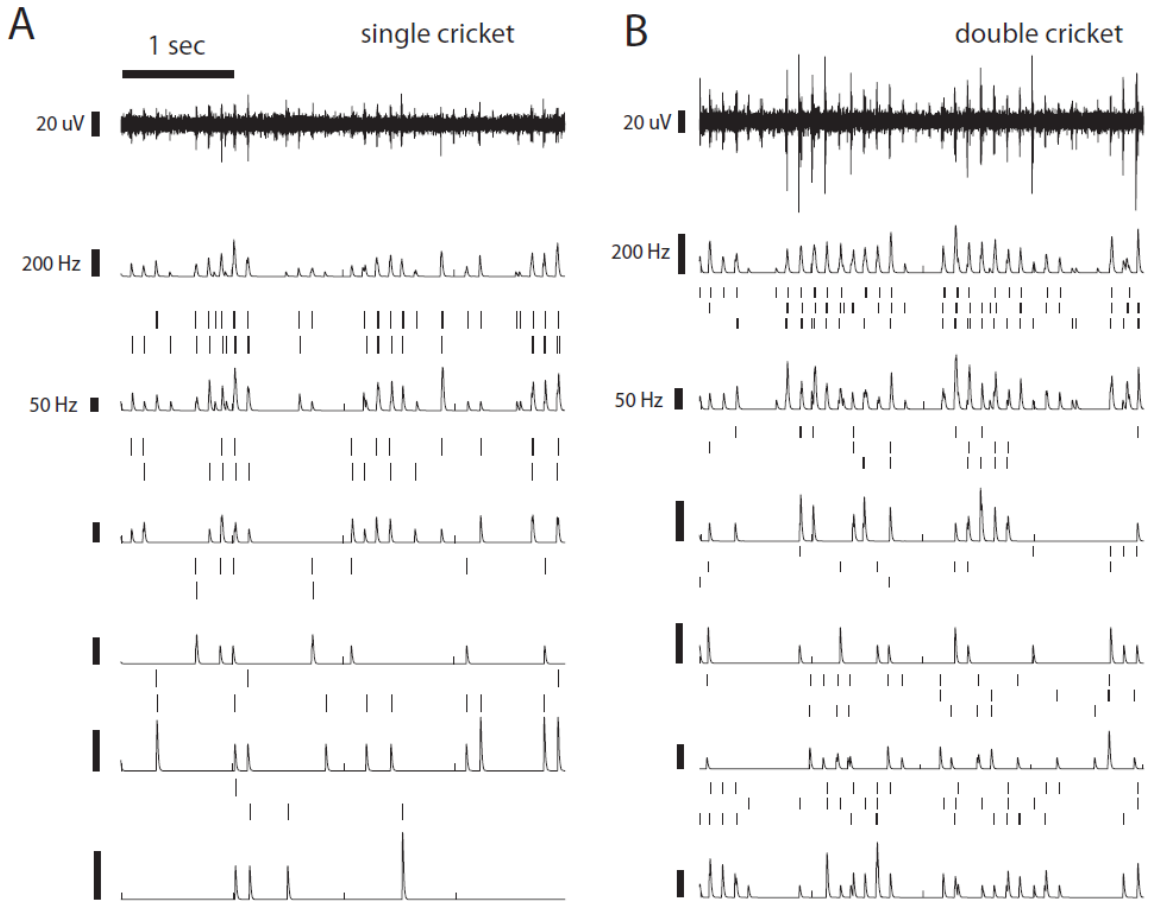

Figure 4.2: Responses of clustered units to cricket stimuli. **(A)** Responses to a single cricket within the center of the multiunit receptive field. **(B)** Responses to the same cricket with an additional cricket placed 30º temporal to the receptive field. See text for details.

In response to a single cricket positioned 30º temporal to the multiunit receptive field, no response was observed (**Fig. 4.1B center**). This is expected since being outside of the classical receptive field by definition means that the stimulus will not elicit a response. However, it should be noted that the small background level of spontaneous activity (2.23 ± 1.28 Hz), present in all units, was notably absent during this stimulus.

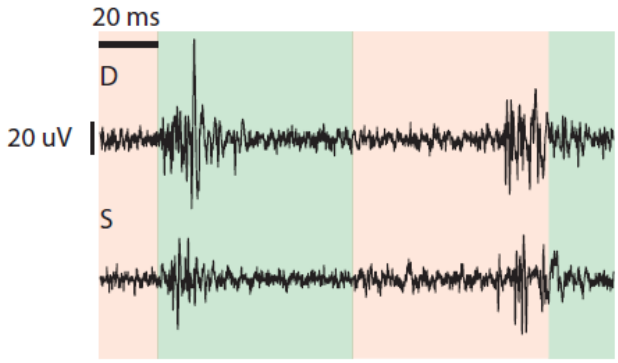

Figure 4.3: Bursting period of the responses to a cricket. Green and tan sections denote the different frames of the visual stimuli. Note that the frequency of the stimuli is distinctly different from the frequency of the response. **D** shows the response to 2 crickets. **S** shows the response to 1 cricket in the receptive field.

In response to both crickets presented simultaneously, the activity of all contributing units went up (**Fig. 4.2B**). This is in striking contrast to the usual effect of additional stimuli presented outside of the classical receptive field. Normally, if an additional stimulus is presented outside of the receptive field, the response goes down because of the presence of an inhibitory surround.

The length of a single burst was between 10-25 ms (**Fig. 4.3**). The time between the start of two successive bursts was between 110-115 ms. We compared this to the frame time (**Fig. 4.3**) to ensure that the frame rate was not affecting the response and no correlation was observed. We checked for peaks in the FFT of the responses to the single cricket within the receptive field or the double cricket stimuli to see if the stimuli frame rate of 15 Hz affected the response (**Fig. 4.4**). All FFTs for all units in either stimulus paradigm were very similar with no qualitative differences. Peaks are seen at 0.6, 1.2, 9, and 18 Hz. There is clearly no peak around 15 Hz. The peaks at 0.6 and 9 Hz (and their multiples) are due to other interactions within the OT, not to the visual stimuli.

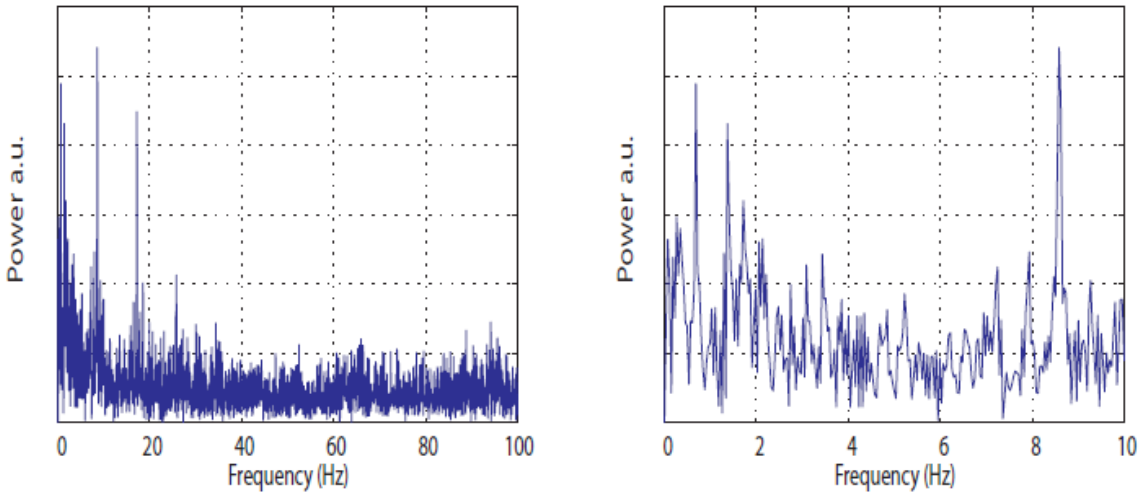

Figure. 4.4: Fourier transforms of the response to the contextual stimuli. FFTs of responses of all units to either stimulus were all qualitatively similar. Note the strong peaks at 0.6 Hz, 1.2 Hz, 9 Hz, and 18 Hz.

The time course of the response can also be explored by looking at the joint-interspike interval distribution (**Fig. 4.5**). The joint-ISI distribution for two

different units to both cricket stimuli shows no clear behavior around 66.6 ms for either unit. Unit 1 had a large average firing rate for all stimulus varieties and unit

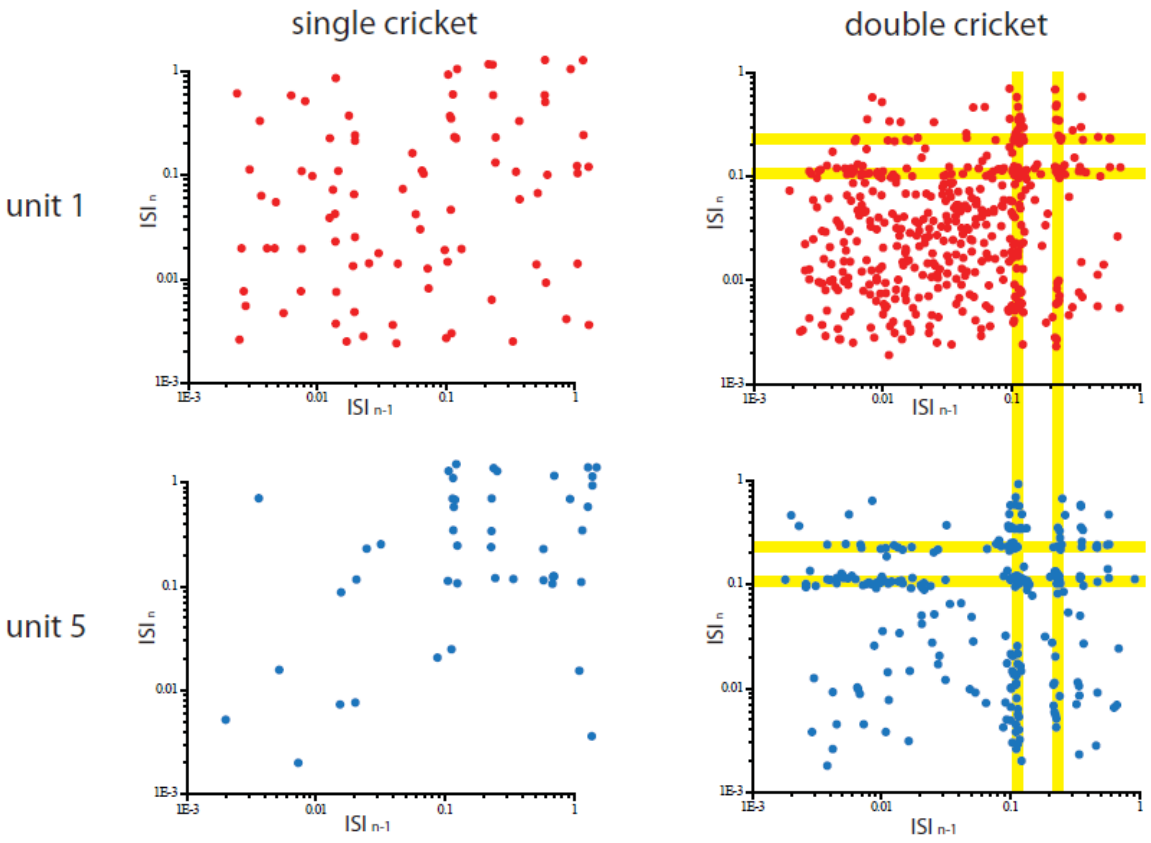

Figure 4.5: Log-log joint-ISI plots of unit 2 and unit 5 in response to either a single cricket within the multiunit receptive field or to the double cricket stimulus. Notice the bands around 110 ms and 220 ms (yellow lines). Times is in ms.

5, in general, had a notably lower average firing rate. There is a lot less structure in the firing pattern of unit 1 than unit 5. Note, however, that both units (and this is true for all units) have bands of activity centered around 110 - 115 ms and 220 - 230 ms (yellow bars in **Fig. 4.5**). This type of joint-ISI pattern can be explained by a unit which fires a Poisson distributed spike train and is driven by a

sinusoidal input, at a frequency around 9 Hz, which only reaches threshold in the top few percent of the duty cycle.

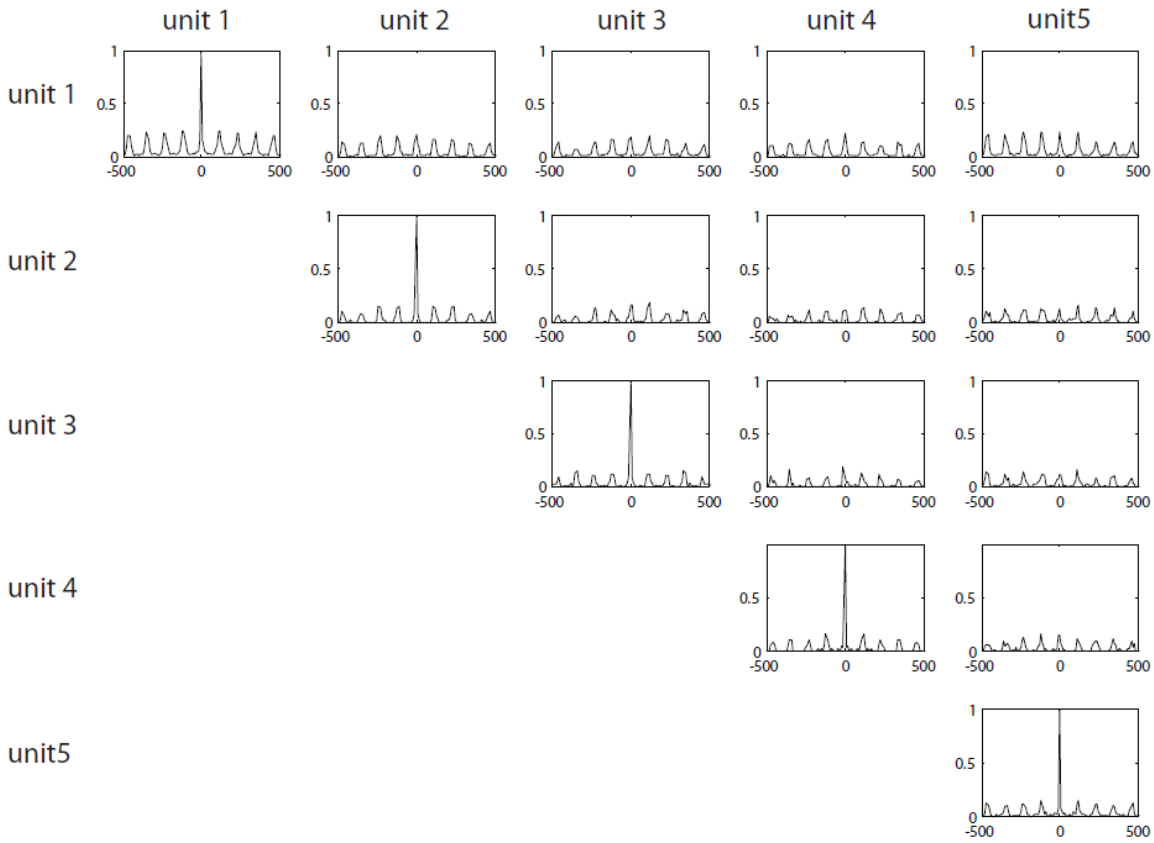

Figure. 4.6: Cross correlation matrix for responses to the single cricket stimulus. Note that the strongest peaks in the autocorrelations (diagonal) are at zero phase lag. Also, note that the cross-correlations, the off-diagonal elements, show roughly level peaks at multiples of 110 - 115 ms. Time axis is in milliseconds.

We looked for correlations between different units in their responses to these varying types of stimuli. A high correlation could imply that neighboring units (as we can assume we are recording) are receiving a very high percentage of shared inputs or that the units are driving each other or interacting with each

other's responses (**Fig. 4.6**). We calculated the cross correlations at phase lags up to 1,000 ms. Note that there are non-zero correlations at multiples of 110 - 115 ms between all units. This simply shows that all units are contributing in a phasic manner to most oscillations in the response. There are no strong peaks

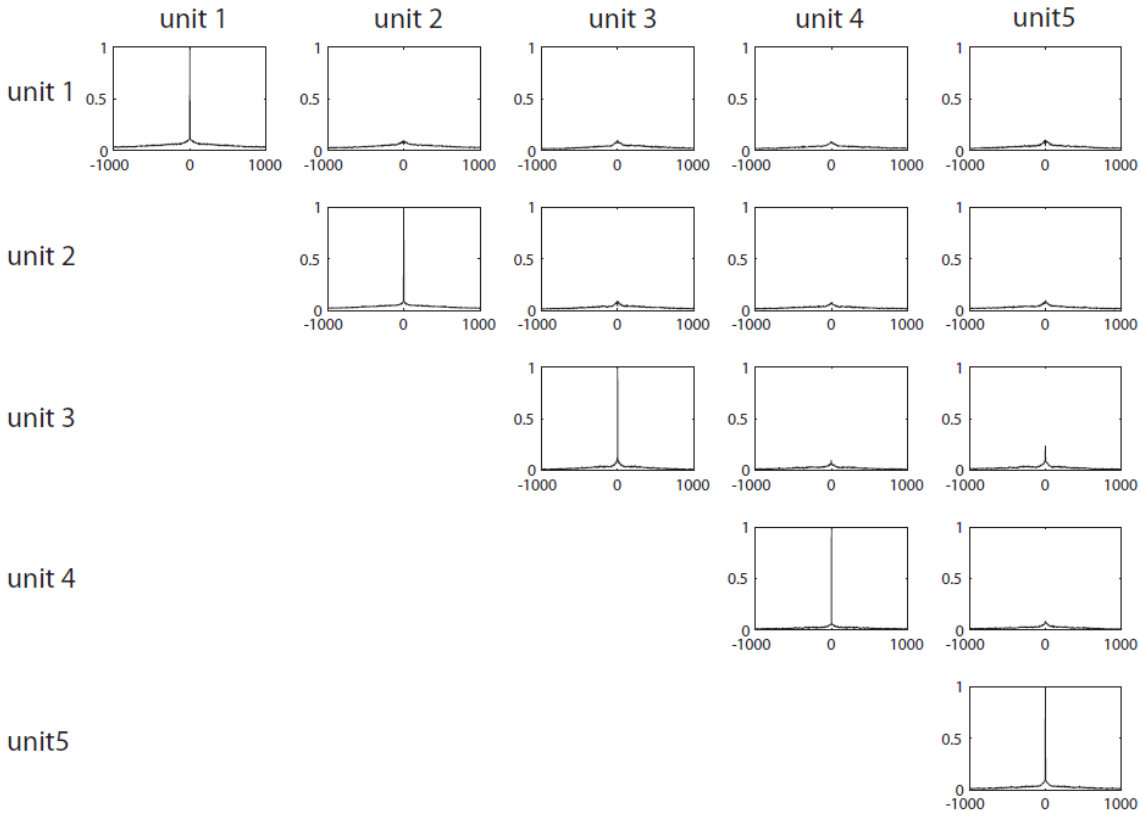

Figure. 4.7: Cross correlation matrix for responses to diffuse illumination steps. Note that the only peaks in the autocorrelations (diagonal) are at zero phase lag. Also, note that the cross-correlations, off-diagonal elements, show nearly zero cross-correlation. Time axis is in milliseconds.

in the cross-correlations (off-diagonal elements) as there are in the auto-correlations (diagonal elements). Thus, no pairs of units are firing with a set lag relative to each other with a strong probability. This behavior was compared to

that seen in the correlations in the responses to other stimuli (**Fig. 4.7**). All other stimuli tested (see previous chapter) had qualitatively similar cross- and auto-correlation matrices as seen here for the diffuse illumination steps. Note that

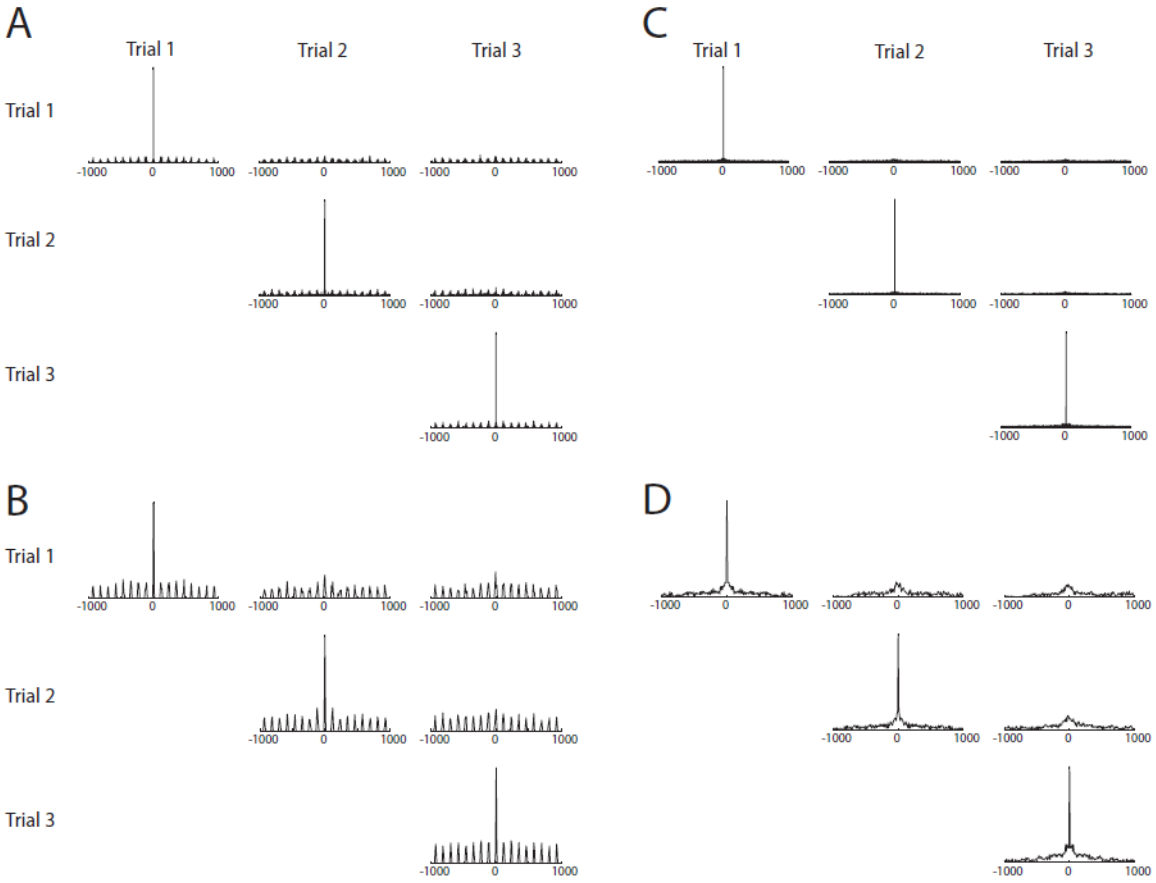

Figure 4.8: Trial-to-trial cross correlations. **(A)** and **(B):** Cross correlations of three trials of the responses of a unit to double cricket stimuli. **(C)** and **(D):** Cross correlations of three trials of the responses of a unit to diffuse illumination steps. Lag time in all plots is in milliseconds. Ordinate scale is normalized to the autocorrelation (diagonal) with the maximum equal to one. Bin size in (A) and (C) is 1 ms. Bin size in (B) and (D) is 10 ms.

there is a significantly high peak in the auto-correlations which is completely absent in all cross-correlations. The correlations all look qualitatively similar if

the bins are set anywhere from 4 - 50 ms. Note that even though all responses are remarkably similar to each other in their time course, there is strikingly little correlation in the spike trains. Calculating the correlations for single trials or for all trials averaged together gives qualitatively similar results. The small non-zero values away from zero phase lag in the autocorrelations are due to the fact that the mean was not subtracted off of the data vectors used in the correlations.

The trial-to-trial variability is very small for all of the responses to the cricket stimuli (**Fig. 4.8**). The cricket moved to a new random position every 66.6 ms. The set of serial movements was frozen in so that every trial was identical. The frame rate of the presentation of the cricket was shown above to not be in register with the periodicity of the response. Yet, even across trials the response is very regular. The trial-to-trial cross correlations are so regular that the peaks are easily discernable (**Fig. 4.8A** and **Fig 4.8B**). The peaks are even spaced at multiples of 110-115 ms. For comparison, we also show the trial-to-trial cross correlations for three trials in response to the diffuse illumination (**Fig. 4.8C** and **Fig 4.8D**). In **Fig 4.8A** and **Fig 4.8C**, the bin width is 1 ms, and so only one spike can possibly be within a bin. In **Fig 4.8B** and **Fig 4.8D,** the bin size is 10 ms so we can see more clearly the regular pattern of activity. This temporal correlation is very puzzling.

We created a simple two-level network model to try to reproduce the responses of the isthmic neurons to the cricket stimuli. The salient aspects of the response are periodic oscillatory bursts with a 9 Hz inter-burst frequency (**Fig.**

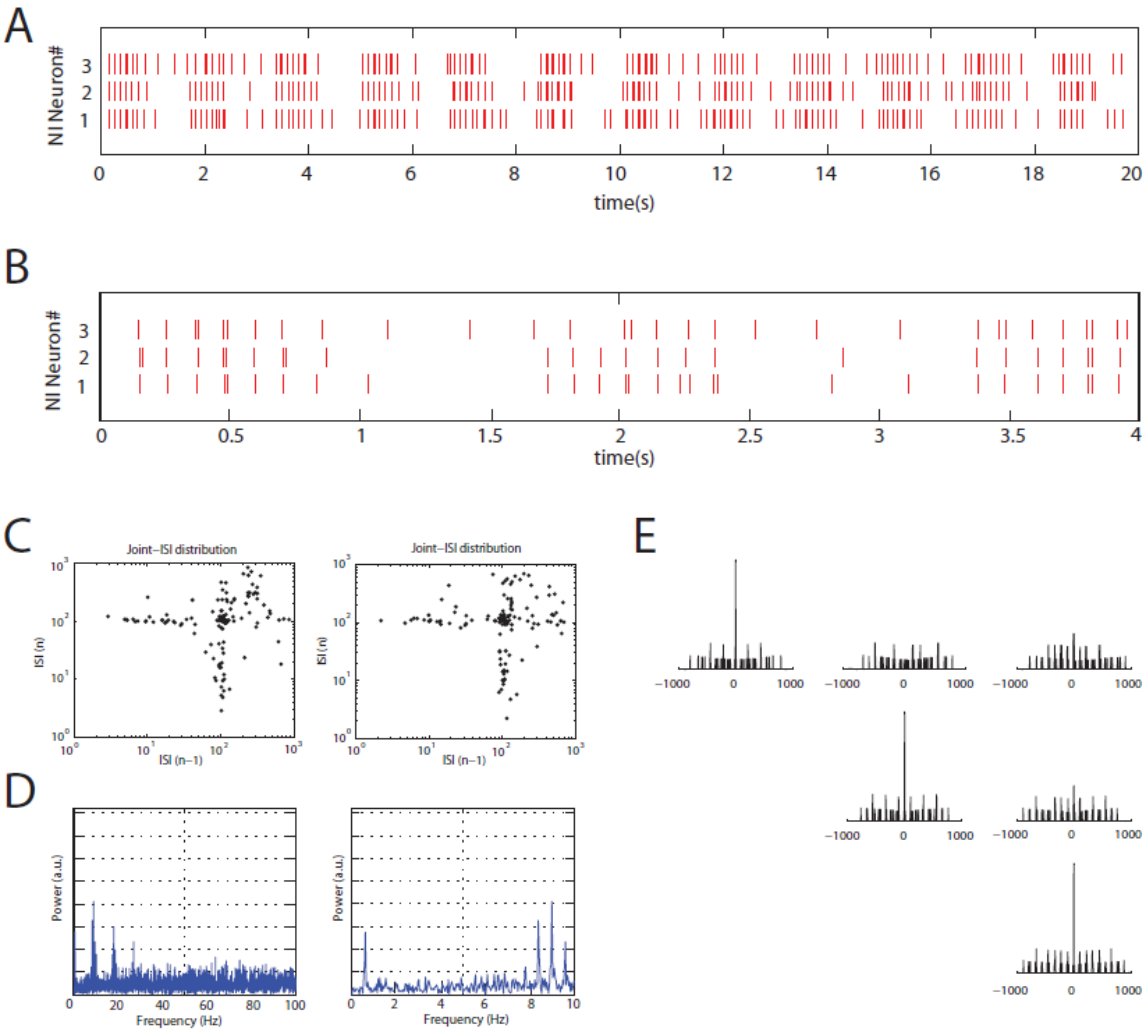

Figure 4.9: Results of the tecto-isthmic model. **(A)** The response of three of the 200 NI units to the OT input. Note the 9 Hz periodic oscillatory bursting modulated by the slower 0.6 Hz frequency. **(B)** A detail of (A) to observe that many units fire multiple times per burst. **(C)** Joint-interspike interval distributions. Scale is a log-log plot in milliseconds. Note the bands just above 100 ms corresponding to the Poisson nature of the intrinsic NI response. **(D)** FFT of the NI response. Note the presence of peaks at multiples of 9 Hz as is seen in **Fig. 4.4**. **(E)** Cross correlations for thee NI units (off-diagonal elements) with autocorrelations (diagonal elements). Lag times are in milliseconds.

4.2). The probability for the bursting to occur is modulated by a slow 0.6 Hz frequency. Also, there is very little correlation among the NI responses, aside from small peaks at multiples at the bursting period (**Fig. 4.6**). The only way we could reproduce these data with a model which reflects the known connectivity and known cellular physiology was to have a global modulation of the OT being driven by these frequencies (**Fig, 4.9**). If the OT receives a constant input or a step input, the NI response is non-oscillatory (data not shown) and produces Poisson spike trains. In the presence of uncorrelated spontaneous activity the correlation between the NI neurons is small; however, all the neurons still have oscillatory components of 9 Hz and 0.6 Hz which is due to the retinal input current to the OT. We were not able to reproduce the odd time course of behavior of **Chapter 3** with this model.

DISCUSSION:

Every unit recorded (N=14) within the NI in response to a cricket presented within the receptive field as well as a cricket 30º temporal to the multiunit receptive field had a larger response than to a lone cricket within the receptive field. Data in other animals overwhelmingly report the opposite affect: an additional stimulus in the surround will suppress responses to a stimulus presented within the classical receptive field (Wang et al., 2004; Paffen et al., 2005; Razak et al., 2005; Hopf et al., 2006; Maczko et al., 2006; Girman et al., 2007; Marin et al., 2007). However, the surround stimulus was not located all around the receptive field but was 30º temporal to it. It has been shown that the frog prefers stimuli presented in the

nasal visual field over stimuli presented in the temporal visual field (Stull et al., 1998). Also, the number of feedback connections from the NI to the OT is much higher in the regions of the OT corresponding to the nasal visual field than that corresponding to the temporal visual field (Dudkin et al., 1999). Thus, since the recording was taken in the visuotopically preferred location, the response went up. Following this logic, if a second cricket is presented 30º nasal to the first, the response should go down at the recording site. Unfortunately, we did not systematically vary the location of the second stimulus, so this experiment must still be performed.

An asymmetric response was seen in the pigeon (Marin et al., 2007). Their experiment differs from ours in that we presented our stimuli simultaneously and they had a time delay between the onset of the two stimuli. When they presented a stimulus in the inferior visual field followed by second stimulus in the superior field, the response in the NI at the location of the inferior field went down drastically. However, when they first presented the superior stimulus followed by the superior stimulus, the response went down at the inferior location, but not nearly as strongly. Thus, there is an inherent asymmetry in the pigeon's NI response as well. Further experiments will need to be carried out in the frog following the paradigm of Marin's paper to investigate the temporal interactions more closely.

A great surprise in all of the responses to the stimuli present here is the omnipresence of the oscillations in the responses of the NI. Some oscillations

were seen in the secondary wave of activity to a diffuse illumination ON step in some units. Also, some oscillations were apparent in some responses to the looming stimuli. However, the oscillations present in the responses presented in this chapter were robust and long lasting. The most apparent is the periodicity of the multiunit bursts with a time between the start of the bursts equal to around 110 - 115 ms. The robust quality of these oscillations is supported by the peak in the FFT at 9 Hz as well as the strong lines in the joint-ISI plots at approximately 110 - 115 and 220 - 230 ms. While the joint-ISI pattern can be explained by a Poisson distributed process being modulated by a sine wave with a 9 Hz frequency, it is not clear from where that modulation is arriving. All of the recorded units had this pattern. Recordings were taken within three separate locations within the NI separated 80 μm dorso-ventrally from each other. The only way for the oscillation to be present in each response is for the 9 Hz oscillation to be a characteristic of the whole of the OT. If there is a local field potential (LFP) which is pervasive within the OT which can only drive the units close to threshold at the highest part of the duty cycle, then the outputs will all fire with the aforementioned pattern. This rhythm could arise in the retina. Strong oscillations have been observed in the retina of the frog (Lettvin et al., 1959; Maturana et al., 1960; Ishikane et al., 1999; Arai et al., 2004; Ishikane et al., 2005) as well as in the cat (Steinberg, 1965). The frequencies of oscillation have all been stimulus and activity dependent. Yet it was shown above that the frequency components of the stimulus did not drive the frequencies of the

responses. The dimming detectors were shown to have 10 Hz or 20 Hz components depending on how strong of an OFF step there were responding to.

A slower oscillation in the FFT at 0.66 Hz was also present in the responses to the crickets. This can be seen in **Fig. 4.1B** and **Fig. 4.2** as an oscillation in the envelope of the response. This may reflect the coherence of the OT input to the NI. At the antinodes of the oscillation, there is very high coherence in the OT output and so there is a high probability for simultaneous spiking in the NI, thus the appearance of large voltage deflections in the raw traces. At the nodes of the oscillation, the OT output is relatively decoherent, leading to non-simultaneous arrivals of spikes at the dendrites of the NI, thus a lower firing probability and therefore a lower probability for overlapping or superposed spikes in the raw voltage waveform. Again, this raises the question: from where is the modulation of the tectum arising? Is there information content in the coherence of the tectal population activity? Strong coupling between neural centers which feedback to each other has been shown to affect precision and information capacity (Andolina et al., 2007; Litaudon et al., 2008), shaping of receptive fields (Schwabe et al., 2006), and behavior (Bair et al., 2001). More work needs to be done in this system to study what effects the isthmotectal feedback projection has on oscillations in the isthmotectal system and on the coherence of the LFP within the OT.

A model was created to try to understand from where these frequencies were arising. If we understand the strongest component of the system as the

topographic feedforward tecto-isthmic projection, then the only way to reproduce the oscillatory nature of the response is to have the OT itself be driven by those frequencies. Unfortunately, this just moves the question back another level: from where are the modulations and frequencies present within the LFP of the OT arising? The NI produce Poisson spike trains to steady input which matches typical responses (data not shown). But to complex temporal stimuli, more complicated interactions must be taking place within the retina or the superficial OT to cause the observed time courses in the responses.

Another great surprise was the strong temporal correlations exhibited trial-to-trial. This implies that the response is driven to be in the same phase at the commencement of the trial by the turning on of the stimulation monitor. There is no other salient part of this stimulus paradigm which could cause such a strong correlation across trials. Some of these trials took place as much as 30 minutes apart, yet the correlation remains strong. Strong trial-to-trial correlations have been observed in frozen noise experiments within the retina (Chichilnisky, 2001; Fellous et al., 2004) and in other sensory areas (Chase et al., 2006). It should be noted that not only the 9 Hz oscillations are in phase trial-to-trial, but also the 0.6 Hz oscillations exhibited in the frequency of the envelope of the voltage response (**Fig. 4.2**). Possibly the combination of the moving crickets and the sudden illumination caused by the screen turning on led to the coherent waves in the local field potential of the OT thus driving the responses further down the synaptic chain into the NI. No oscillation was observed in the last chapter in

response to the strong steps in diffuse illumination. More experiments are required to solve this strange puzzle.

In summary, this chapter has shown that the response in the NI may respond more vigorously to an additional stimulus presented within the classical surround. This is quite counter intuitive and may possibly be further evidence for an asymmetric winner-take-all mechanism in the frog's OT-NI system. More data is needed to follow up on this claim. Also, population-wide simultaneous oscillations in the responses of units within the NI may be caused by global oscillations within the OT which evolves in and out of coherent epochs. These oscillations are robust even trial-to-trial. Where this modulation arises from is still a mystery.

ACKNOWLEDGEMENTS:

I am very indebted to Dihui Lai for fruitful discussions and his programming on the model presented in this Chapter.

REFERENCES:

Andolina IM, Jones HE, Wane W, Sillito AM. Coritcothalamic feedback enhances stimulus response precision in the visual system. *PNAS*. 2007. **104**: 1685-1690.

Arai I, Yamada Y, Asaka T, Tachibana M. Light-evoked oscillatory discharges in retinal ganglion cells are generated by rhythmic synaptic inputs. *J Neurophysiol*. 2004. **92**: 715-725.

Bair W, Zohary E, Newsome WT. Correlated firing in macaque visual are MT: time scales and relationship to behavior. *J Neurosci*. 2001. **21**: 1676-1697.

Brandt SF, Wessel R. Winner-take-all selection in a neural system with delayed feedback. *Biol Cybern*. 2007. **97**: 221-228.

Chase SM, Young ED. Spike-timing codes enhance the representation of multiple simultaneous sound-localization cues in the inferior colliculus. *J. Neurosci.* 2006. **26**: 3889-3898.

Chichilnisky EJ. A simple white noise analysis of neuronal light responses. *Network*. 2001. **12**: 199-213.

Deco ., Pollatos O, Zihl J. The time course of selective visual attention: theory and experiments. *Vision Res*. 2002. **42**: 2925-2945.

Desimone R, Duncan J. Neural mechanisms of selective visual attention. *Annu Rev Neurosci*. 1995. **18**: 193-222.

Dudkin ES, Gruberg ER. Relative number of cells projecting from contralateral and ipsilateral nucleus isthmi to loci in the optic tectum is dependent on visuotopic location: horseradish peroxidase study in the leopard frog. *J. Comp. Neurol*. 1999. **414**: 212-216.

Fellous JM, Tiesinga PHE, Thomas PJ, Sejnowski TJ. Discovering spike patterns in neuronal responses. *J. Neurosci*. 2004. **24**: 2989-3001.

Gilbert CD, Sigman M. Brain states: top-down influences in sensory processing. *Neuron*. 2007. **54**: 677-696.

Girman SV, Und RV. Most superficial sublamina of rat superior colliculus: neuronal response properties and correlates with perceptual figure ground segregation. *J. Neurophysiol*. 2007. **98**: 161-77.

Gruberg ER, Lettvin JY. Anatomy and physiology of a binocular system in the frog *Rana Pipiens*. *Brain Research.* 1980. **192**: 313-325.

Gruberg ER, Wallace MT, Caine HS, Mote MI. Behavioral and physiological consequences of unilateral ablation of the nucleus isthmi in the leopard frog. *Brain Behav Evol*. 1991. **37**: 92-103.

Hopf JM, Boehler CN, Luck SJ, Tsotsos JK, Heinze HJ, Schoenfeld MA. Direct neurophysiological evidence for spatial suppression surrounding the focus of attention in vision. *Proc Natl Acad Sci USA*. 2006. **103**: 1053-1058.

Ishikane H, Kawana A, Tachibana M. Short-and long- range synchronous activities in dimming detectors of the frog retina. *Vis Neurosci*. 1999. **16**: 1001-1014.

Ishikane H, Gangi M, Honda, S, Tachibana M. Synhcornized retinal oscillations encode essential information for escape behavior in frogs. *Nature Neurosci.* 2005. **8**: 1087-1095.

Lee DK, Itti L, Koch C, Braun J. Attention activates winner-take-all competition among visual filters. *Nature Neuro*. 1999. **2**: 375-381.

Lettvin JY, Maturana HR, McCulloch WS, Pitts WH. What the frog's eye tells the frog's brain. *Proceedings of the IRE*. 1959. **47**: 233-258.

Litaudon P, Garcia S, Buonviso N. Strong coupling between pyramiodal cell activity and network oscillations in the olfactory cortex. *Neurosci*. 2008. **156**: 781-787.

Maczko KA, Knudsen PF, Knudsen EI. Auditory and visual space maps in the cholinergic nucleus isthmi pars parvocellularis of the barn owl. *J. Neurosci*. 2006. **26**: 12799-12806.

Marin G, Mpodozis J, Sentis E, Ossandon T, Letelier JC. Oscillatory bursts in the optic tectum of birds represent re-entrant signals from the nucleus isthmi pars parvocellularis. *J Neurosci*. 2005. **25**: 7081-7089.

Marin G, Salas C, Sentis E, Rojas X, Letelier JC, Mpodozis J. A cholinergic gating mechanism controlled by competitive interactions in the optic tectum of the pigeon. *J Neurosci.* 2007. **27**: 8112-8121.

Maturana HR, Lettvin JY, McCulloch WS, Pitts WH. Anatomy and physiology of vision in the frog (Rana pipiens).*J General Physiol*. 1960. **43**: 129-175.

Maunsell JH, Cook EP. The role of attention in visual processing. *Philos. Trans. Roy Soc Lond B Biol Sci.* 2002. **357**: 1063-1072.

Paffen CL, van der Smaqt MJ, te Pas SF, Verstraten FA. Center-surround inhibition and facilitation as a function of size and contrast at multiple levels of visual motion processing. *J Vision*. 2005. **5**: 571-578.

Posner MO. Orienting of attention. *Q.J. Exp Psychol*. 1980. **32**:3-25.

Razak KA, Pallas SL. Neural mechanisms of stimulus velocity tuning in the superior colliculus. *J. Neurophysiol*. 2005. **94**: 3573-3589.

Schitzler A, Gross J. Normal and pathological oscillatory communication in the brain. *Nature Neurosci*. 2005. **6**: 285-296.

Schwabe L, Obermayer K, Angelucci A, Bressloff P. The role of feedback in shaping the extra-classical receptive field of cortical neurons: a recurrent network model. *J Neurosci*. 2006. **26**: 9117-9129.

Steinberg RH. Oscillatory activity in the optic tract of cat and light adaptation. *J. Neurophysiol.* 1966. **29**:139-156.

Stull AK, Gruberg ER. Prey selection in the leopard frog: choosing in biased and unbiased situations. *Brain Behav Evol.* 1998. **52**: 37-45.

Wang Y, Major DE, Karten HJ. Morphology and connections of nucleus isthmi pars magnocellularis in chicks (*Gallus gallus*). *J Comp. Neurol*. 2004. **469**: 275-297.

Winkowski DE, Gruberg ER. The representation of the ipsilateral eye in nucleus isthmi of the leopard frog, *Rana pipiens*. *Vis Neurosci*. 2002. **19**: 669-679.

Witten IB, Bergan JF. Knudsen EI. Dynamic shifts in the owl's auditory space map predict moving sound location. *Nat Neurosci*. 2006. **9**: 1439-1445.

Chapter 5:

ON THE NUMBER OF ELECTROPHYSIOLOGICAL SUB-CLASSES OF NEURONS WITHIN THE NUCLEUS ISTHMI OF THE FROG, RANA PIPIENS

ABSTRACT:

The frog nucleus isthmi (parabigeminal nucleus in mammals) is a visually responsive midbrain structure that shares reciprocal topographic connections with the ipsilateral optic tectum (superior colliculus in mammals). Feedback from the nucleus isthmi is bilateral and strongly influences both tectal cells and retino-tectal transmission. Previous research suggests that the nucleus isthmi of the frog may contain electrophysiologically distinct populations. To test this hypothesis we have measured the cellular properties and extracellular responses of isthmic neurons to current injections and simple visual stimuli. Our results show that the neurons of the frog nucleus isthmi have indistinguishable cellular properties and respond similarly to visual stimulation.

INTRODUCTION:

Despite the prevalence of recurrent connections in vertebrate visual pathways (Gruberg et al., 2006; Wang, 2003; Sillito et al., 2006), there is little consensus

on the functional role of feedback projections in visual perception (Sillito et al., 2006). Characterizing the response properties of individual feedback neurons represents an important step in understanding how these projections influence visual processing. The optic tectum (superior colliculus in mammals) (OT/SC) is the primary retino-recipient structure in many vertebrates (Butler et al., 2005). In amphibia, teleosts, reptiles, birds and mammals this important structure receives feedback projections from the cholinergic nucleus isthmi (parabigeminal nucleus in mammals) (NI/PBN), an anatomically well-defined group of neurons in the midbrain (Butler et al., 2005) (**Fig. 5.1A**). Within the bird (Wang et al., 2004) and turtle (Sereno et al., 1987) the NI is divided into multiple separate and distinct neuron types. These sub-nuclei have different physiological response properties, use different neurotransmitters, and are anatomically separate. Behavioral studies in the frog have shown that the NI is critical for visual processing, as lesions of the NI lead to scotomas (functional blind spots) for moving objects (Gruberg, 1991). We therefore chose the frog NI to characterize the response properties of feedback neurons.

The frog retina projects 350,000 retinal ganglion cell (RGC) axons (Maturana, 1959) to the contralateral OT where the axon terminals form a precise retinotectal map (Gaze, 1958). Four different RGC types terminate in discrete lamina of the superficial OT. The targets of the RGC axons include the apical dendrites of cholinergic neurons, with somata located in layer 6, which project to the ipsilateral NI (Gruberg et al., 1978; Lazar et al., 1985; Gruberg et al., 1994)

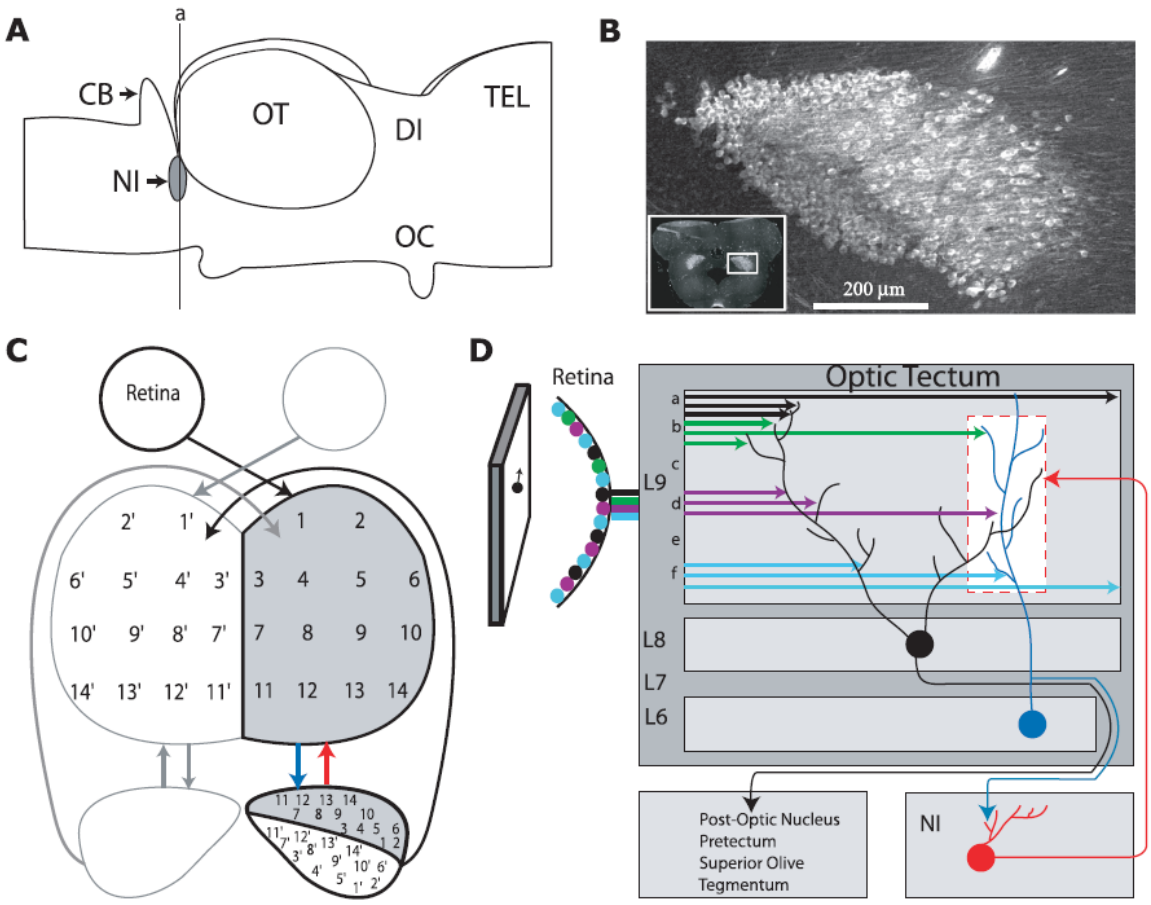

Fig. 5.1. Nucleus isthmi and schematic of retino-isthmo-tectal system. **(A)** Lateral view of the brain. NI is ventral to the caudal pole of the tectum. Rostral is to the right. CB, cerebellum; DI, diencephalon; OC, optic chiasm; TEL, telencephalon. Transverse section a is shown in Fig. 1 B inset. **(B)** Acetylcholine transferase-stain of NI magnified from inset. **(C)** Diagram of connectivity between retina, tectum and NI. Each eye projects a retinotopic map directly to the contralateral OT. The OT in turn projects (blue arrow) to cells in the NI. The numbered areas in the NI correspond to clusters of cells projecting to numbered areas in the OT. Dorsolateral NI cells shown shaded project (red arrow) to the ipsilateral OT. Ventromedial NI cells (not shaded) project to the contralateral OT (Figure adapted from Dudkin et. al., 2007). **(D)** Diagram of ipsilateral retino-tecto-isthmal system. Four retinal ganglion axon types (black, green, purple and light blue

arrows) project to discrete lamina of layer 9 of the OT synapsing onto dendrites of neurons whose cell bodies are located in layer 6 (blue) or layer 8 (black). NI cells (red) receive inputs from layer 6 axons and project back to the column (white box) in the OT from which they received inputs.

(**Fig. 5.1D**). The isthmotectal projection is bilateral and topographically arranged to be in register with the feedforward retinotopic map (Gruberg et al., 1978; Gruberg et al., 1994). Further, within NI, ipsilaterally projecting NI cells are located dorso-rostral-laterally to the contralaterally projecting cells and project to the column in the OT from which they received inputs (**Fig. 5.1 C,D**) (Dudkin et al., 2007). In addition, the NI possess cholinergic and GABAergic neurons (**Fig. 5.1B**) (Wallace et. al., 1990; Marin et. al. 1997; Li et al., 2001). The presence of these types of neurotransmitters along with the spatial segregation of the ipsilateral and contralateral projections, as well as the distinct populations seen in other animals, led us to hypothesize that the 8000 neurons (Gruberg et al., 1978) in the frog NI consist of electrophysiologically distinct populations; a diversity that is common in many neural systems (Wang et al., 2000; Soltesz, 2006).

Here, we address whether the NI contains electrophysiologically distinct populations in two different ways. First, we characterize the cellular properties of the isthmic neurons in response to somatic current injections *in-vitro*. Second, we characterize the visual response properties of simultaneously recorded NI neurons within a small volume around the tip of an extracellular recording electrode.

METHODS: *IN-VITRO*

Surgery & Preparation:

Ten adult *Rana pipiens* were used in this study. All procedures used in this study were approved by the Washington University Institutional Animal Care and Use Committee and conform to the guidelines of the National Institutes of Health on the Care and Use of Laboratory Animals.

Isthmic brain slices were obtained from adult leopard frogs that had been anesthetized by submersion in a 0.1% solution of ethyl m-aminobenzoate. After decapitation the brains were removed and placed in a Petri dish filled with ice-cold saline solution (pH=7.4) composed of (in mM): 112 NaCl, 2 KCl, 3 $MgCl_2$, 17 $NaHCO_3$, 3 $CaCl_2$, 24.2 glucose and saturated with 95% O_2 and 5% CO_2 (Yu et al., 2003). This solution was also used as the bath solution in the recording chamber. The brain was then embedded in a 0.4% solution of low-melting-point agarose (type VII agarose, Sigma, St. Louis, MO, USA) and cooled until hardened. The embedded brain was sectioned at 300 μm on a tissue slicer (Vibroslice, Campden or VF-200, Precisionary Instruments) in the transverse plane. Sections were collected and placed in the ice-cold saline bubbled continuously with 95% O_2 and 5% CO_2. The slice was then transferred to a recording chamber (RC-26G, Warner Instruments) mounted on a fixed-stage upright microscope equipped with differential interference contrast optics (BX-51WI, Olympus). The slice was held gently to the bottom of the chamber with an

anchor of parallel nylon threads, and the chamber was perfused continuously with oxygenated saline at room temperature.

Recordings:

Whole-cell recordings were obtained with glass micropipettes pulled from borosilicate glass (1.5 mm OD, 0.86 mm ID, AM Systems) on a horizontal puller (P-97, Sutter Instruments) and were filled with a solution containing (in mM) 90 K-Gluconate, 25 NaCl, 12 mM HEPES, 1 mM CaCl2, 3 MgCl2, 10 EGTA, pH adjusted to 7.4 with KOH. Electrodes were advanced through the tissue under visual guidance with a motorized micromanipulator (MP-285, Sutter Instruments) while constant positive pressure was applied. The electrode resistance was monitored by brief current pulses. Once the electrode had attached to a membrane and formed a seal, access to the cytosol was achieved by brief suction. Whole-cell recordings were performed with the amplifier (Axoclamp 2B, Axon Instruments) in the bridge mode (current clamp). The series resistance was estimated by toggling between the bridge and the DCC (discontinuous current clamp) mode, and subsequently compensated with the bridge balance. Depolarizing and hyperpolarizing currents were injected through intracellular electrodes. Analog data were low-pass filtered (4-pole Butterworth) at 1 kHz, digitized at 5 kHz, stored, and analyzed on a PC equipped with a PCI-MIO-16E-4 and LabView software (both National Instruments).

Data Analysis:

Intracellular recordings were obtained for 8 NI cells from 10 animals with an average recording time of 19.8 minutes (Range 10.0-30.0 min). After obtaining a whole-cell configuration we measured passive, threshold, and above threshold membrane responses to 1-second current pulses. Below we provide a list of properties determined for each cell in the NI.

Resting membrane potential. The membrane potential V_m (mV) was measured from the voltage trace 1 minute after the whole cell configuration was achieved. The liquid junction potential was measured and estimated to be approximately −9 mV. This correction was ignored, i.e., the real membrane potentials are more negative than the stated values.

Input resistance. Each cell's input resistance R_{In} (MΩ) was calculated from the steady state membrane potential responses to a small hyperpolarizing (-5 to -10 pA) current pulse of 1-second duration.

Membrane time constant. The time constant of the membrane τ_m (ms) represented the elapsed time for the membrane voltage to reach 63% of the steady state value in response to small hyperpolarizing (-5 to -10 pA) current pulses of 1-second duration. This was determined by fitting the response of the voltage with a single exponential function.

Rheobase current. The rheobase current I_{RH} (pA) was measured as the smallest amplitude, 1-second current pulse that elicited a single action potential.

Rheobase latency. The rheobase latency T_{RH} (ms) was measured as the time difference between the onset of the rheobase current pulse and the peak voltage deflection of the action potential.

First spike amplitude. The first spike amplitude was measured as the voltage (mV) difference between the peak amplitude of the action potential and the peak amplitude in the after-hyperpolarization.

Spike half-width. The spike half-width (SHW)was the width of the action potential (ms) at half-maximum amplitude relative to rheobase voltage which was estimated as $SHW = \left(R_{In} \bullet I_{Rh}\right) + V_m$.

After-hyperpolarization. The after-hyperpolarization time constant τ_{AHP} (ms) was calculated from a single exponential decay fitting of the voltage trace starting from the peak in the AHP to the steady state voltage following a single AP elicited at the rheobase current.

Interspike Interval. The time course of the interspike interval was measured in response to a 1-second current pulse with an amplitude of 90 pA. This current was chosen because it was well above the rheobase current for all cells. To quantify the spike-rate adaptation, the interspike interval data was fit with an exponential decay function and the time constant ISI_{τ} (ms) and steady state values $ISI_{Steady-State}$ (ms) were determined.

Stimulus current to spike frequency relation. Depolarizing current injections between 0 - 100 pA in 10 pA steps were applied in a pseudo-random sequence to obtain the current to spike frequency relationship. Data gathered from all cells was averaged and is presented with standard deviations. In addition, the instantaneous frequency, defined as the inverse of the first interspike interval, was also calculated, averaged across cells, and is presented with standard deviations (SD).

All numerical results are presented as means ± SD.

Principal Component Analysis

We used a principal component analysis to assess whether the cells could be categorized into two or more populations based on their electrophysiological characteristics. Briefly, we standardized each of the measurements above by:

$x_i \rightarrow \frac{x_i - \bar{x}}{\Delta \bar{x}}$, where x_i is a single measurement of one of the properties listed above, $\bar{x}$ is the average of all cells for a given property and $\Delta \bar{x}$ is the standard deviation. The resultant parameter means are zero and the standard deviation is ±1.0. This normalization allows each parameter to contribute equally to the similarities and differences among cells. Each of these values is an element in the correlation matrix of the data. We then determined the eigenvalues and eigenvectors of this correlation matrix using MATLAB 6.5 (Mathworks, Natick

MA, USA) and projected the measured data onto the principal components (eigenvectors) with the largest eigenvalues.

METHODS: *IN-VIVO*

The same procedures were followed herein as were described in **Chapter 3** above.

To analyze the similarities and differences of the responses of the units to the various stimuli, we investigated the most salient aspects of the responses. The salient aspects include: the strong initial response to the ON illumination step, the secondary wave of activity in response to the ON step, the strong response to the OFF step (**Fig. 3.1**), the strong response to the commencement of motion of a moving spot (**Fig. 3.3**), the delayed response to the cessation of a moving spot (**Fig. 3.5**), and the response to a looming stimulus (**Fig. 3.6**). The responses were quantified by summing the average firing rate of a given unit over the epoch of time during which the salient aspect of the response took place. This quantity was then normalized by dividing by the total number of spikes a given unit fired during the entire experiment. This way, the response of each unit was calculated in relation to its total response. This was repeated for all stimulus types (each direction of moving spot and each apparent approach velocity of looming spot). Thus, 37 salient aspects of the responses were used in the analysis. Probability distributions were computed for each of the different salient responses. Principle component analysis (PCA) was also performed on

the total set of responses for all units in which responses were recorded for the whole set of stimuli.

In total, 48 recording sites in 22 frogs were utilized to obtain the data herein presented. At those sites, 152 units were well isolated from each other and the background noise. Of those, 80 units were tested with the entire set of stimulus varieties. These 80 units are used for the PCA analysis. Individual probability distributions are composed of greater numbers of units, as mentioned below.

RESULTS: *IN-VITRO*

The NI is a structure situated ventral to the caudal pole of the OT (**Fig. 5.1A,B**) (Khalil et al., 1976). Within the structure there is an anatomical division between cells projecting to the ipsilateral and contralateral OT (Dudkin et al., 2007). We performed intracellular recordings (in whole-cell patch mode) from 8 NI neurons in brain slices of 6 young adult *Rana pipiens*. Although the locations of the recording sites (**Fig. 5.2A**) were distributed throughout the extent of the NI, all recorded neurons displayed similar tonic discharge patterns in response to 1-second depolarizing current injections. To characterize the passive, threshold and above threshold membrane responses of NI neurons we measured 10 properties listed in the data analysis section of this paper. Below we summarize the results of these measurements.

Passive membrane properties

Of the 8 neurons recorded, 2 were spontaneously spiking with mean rate of 2.5 Hz. Their resting potential was measured to be -60 ± 7 mV and their input resistances were very high 1,007 ± 20 MΩ. This result agrees with earlier studies that have shown that the neurons of the NI are small with somata diameters ranging from 8 to 12 μm (Li et al., 2001). In addition we determined the membrane time constant for 7 of the cells to be 132 ± 23 ms. This time constant along with the input resistance gives a passive membrane capacitance of 136 ± 35 pF. This data is summarized in **Table 5.1** and in **Fig. 5.3A**.

Threshold membrane properties

One result of the high input resistances of the NI cells is that pico-ampere current injections bring the cells to threshold for spiking. The rheobase current was measured to be 20 ± 4 pA with a first spike latency of 294 ± 178 ms. The high variability in the first spike latency is not due to outliers but rather to an even distribution of data points between the highest and lowest recorded values (**Fig. 5.3A**). The rheobase current elicited an average of 1.8 spikes for the 1-second duration pulse. The amplitudes of the first spike measured relative to the trough in the after-hyperpolarization was 69 ± 13 mV and the spike half-width at half-max relative to the rheobase voltage was 1.7 ± 0.4 ms. Following this first spike, all cells displayed a monophasic AHP (**Fig. 5.2B**) with a time constant of 94 ± 46 ms. Although the variance of τ_{AHP} is high there is a smooth distribution of data

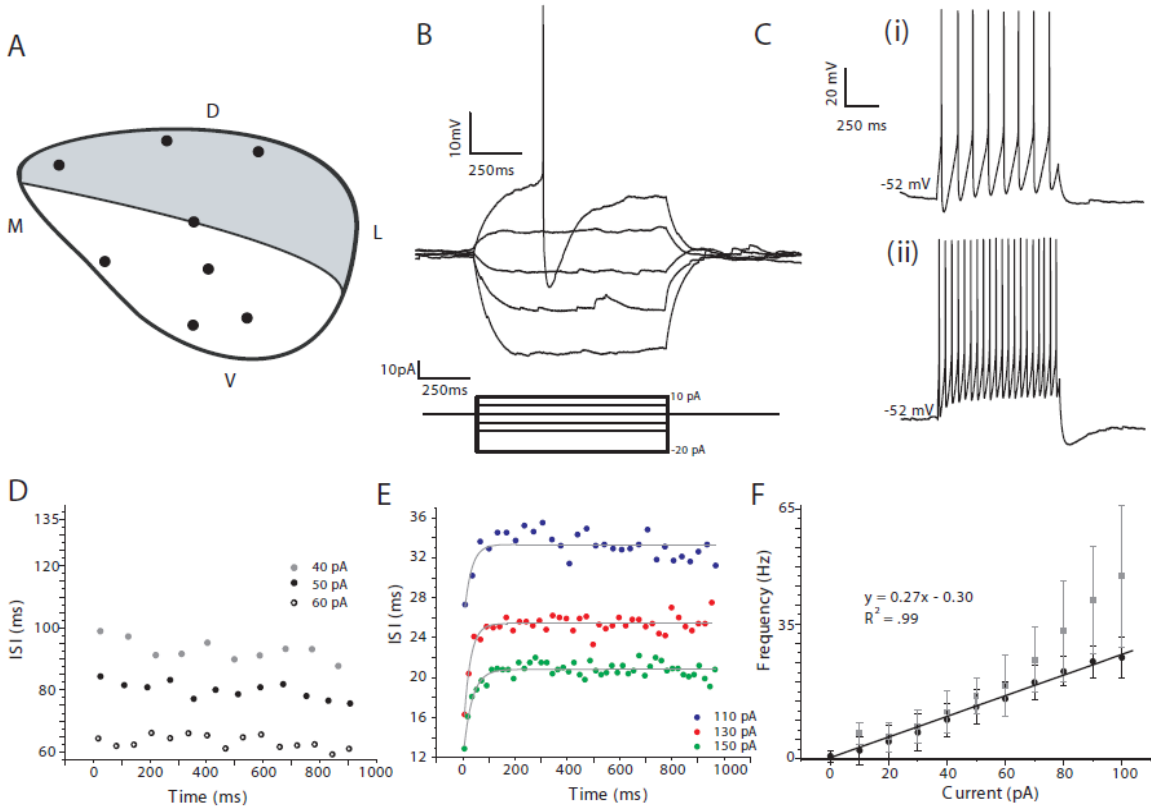

Fig. 5.2. Cellular and electrophysiological properties of frog NI neurons. **(A)** Recording sites of 8 NI neurons. D, dorsal; L, lateral; V, ventral; M, medial. **(B)** Responses of NI neurons to small hyperpolarizing and depolarizing current injections. Note monophasic after-hyperpolarization. **(C)** (i-ii) All cells recorded from respond with tonic discharge patterns for currents above rheobase and maintain firing for the 1-second duration current pulse. Shown here are the responses of two cells. **(D)** At low current injections (<60 pA) the interspike intervals are constant. **(E)** Higher current injections show significant spike rate adaptation. Grey lines are exponential fits to the data. **(F)** Current to spike frequency relationship is linear (filled black circles) for currents up to 100 pA. The instantaneous frequency is (grey boxes) is nonlinear for currents exceeding 60 pA.

points between the highest and lowest values recorded (**Fig. 5.3A**). A summary of this data is presented in **Table 5.1** and in **Fig 5.3A**.

Above threshold properties

To current injections above the threshold for spiking, NI neurons responded with tonic discharge patterns that lasted the length of the 1-second stimulus pulse (**Fig 5.2C**). To characterize these discharge patterns we measured the interspike interval at low currents (**Fig. 5.2D**) and at high currents (**Fig. 5.2E**). At low currents the ISI remained constant or slightly decreased throughout the length of the discharge. At a 90 pA current injection, the isthmic cells exhibited spike rate adaptation with time constants of 29 $\pm$ 23 ms and steady state ISI values of 50 $\pm$ 15 ms. The high variability within this dataset is attributed to one outlier in the data distribution (**Fig. 5.3A**). The short time constant for the spike rate adaptation of NI neurons is a feature found in other non-mammalian vertebrates including birds (Shao et. al., 2009) and turtles (Saha et al., 2008). The tonic responses were further characterized by measuring the relationship of the current to the spike frequency. We found a linear F-I curve with slope of 0.27 Hz/pA for current intensities below 100 pA.

Table 5.1. Electrophysiological properties of nucleus isthmi neurons.

V_m(mV)	R_{in}(MΩ)	τ_m(ms)	I_{Rh}(pA)	T_{Rh}(ms)	A_{Spike}(mV)	W_{spike}(ms)	τ_{AHP}(ms)	τ_{ISI}(ms)	ISI_{steady}(ms)
-60 $\pm$ 7	1007±20	132±23	20 $\pm$ 4	294±178	69 $\pm$ 13	1.7± 0.4	94 $\pm$ 46	29± 23	50 $\pm$ 15

Principal Component Analysis:

The distribution of data measured across all cells is shown in **Fig 5.3A**. Each column is a different measurement (see data analysis) and each colored circle is a cell. Some measurements do not have all 8 cells because two of the cell's responses degraded over the recording time of 20 minutes. To assess whether this data can be categorized into two or more groups based on the cellular properties, we performed a principal component analysis (Jolliffe, 1986) on 6 of the 8 cells. We could only use 6 cells because 2 had degraded responses over time precluding the determination of all ten measurements. Using standardized variables we computed the eigenvalues of the correlation matrix (**Fig. 5.3B inset**) and determined how much each eigenvalue accounts for of the data's variance (**Fig. 5.3B**). We found that the first two eigenvalues account for 94% of the data's cumulative variance. This motivated our choice to keep the first two principal components thus reducing the parameter space to two dimensions. **Fig. 5.3C** shows the projection of the original data onto these two principal components. The six cells are scattered about the mean (zero in standardized variables) with no discrete clusters readily apparent. Thus based on the distribution in **Fig. 5.3A** and the principal component projection in **Fig. 5.3C**

Our data suggest that the cellular and electrophysiological properties of the NI neurons are homogeneously distributed.

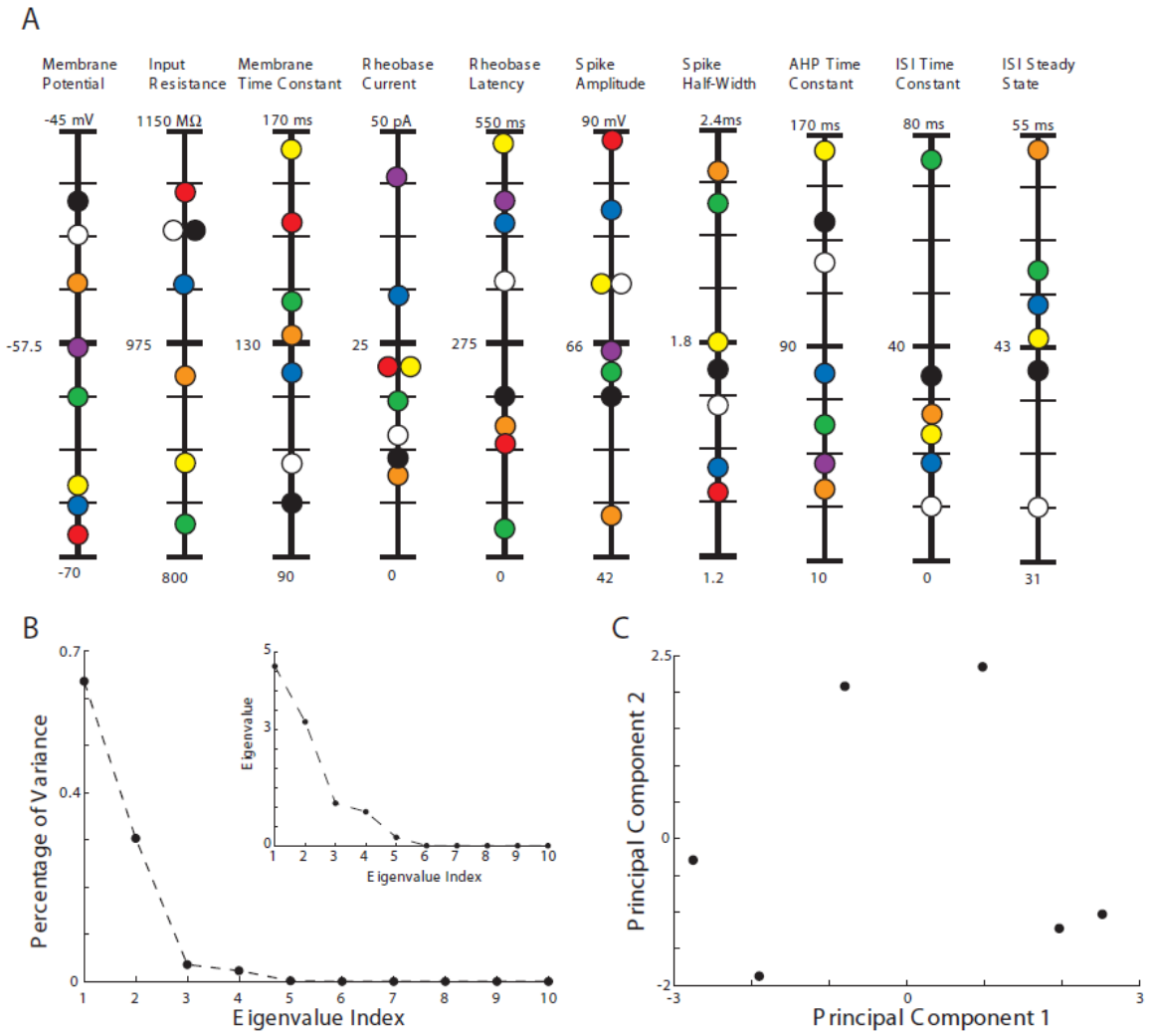

Fig. 5.3: Principal component analysis of the cellular properties of NI neurons. **(A)** Ten different measurements taken from each cell are plotted in separate columns. Colored circles represent individual cells. Note for some measurements only 6 or 7 cells are shown. This is due to deterioration of cellular responses for recordings exceeding 20 mins. **(B)** Eigenvalues determined by a principal component analysis of the 6 cells that appear in all 10 columns of A are shown in the inset. The larger figure shows that the first two eigenvalues account for >90% of the data's variance. This motivates the choice to keep only two principal components (eigenvectors). **(C)** Projection of standardized measurements in A onto the principal components corresponding to the largest two eigenvalues in B

is distributed about the mean values (standardized to be 0). Thus no discrete clusters are apparent for these 6 cells in the 2-dimensional principal component space.

RESULTS: *IN VIVO*

Units were recorded at 48 locations within the NI *in vivo* in 22 leopard frogs. These locations were distributed throughout the entire NI, sampling thoroughly the ipsilaterally-projecting dorso-lateral section of the isthmi as well as the contralaterally-projecting ventro-medial section of the NI. We are presenting only well isolated single unit activity which was sorted from multi-unit voltage recordings using the spike sorting methods described in **Chapter 2**. **Fig. 5.4** shows the results of spike sorting at one specific location. Note that if no spike sorting is done, then the average spike shape of all spikes recorded is clearly a combination of different units (top of **Fig. 5.4A**). In addition, the interspike interval distribution of the unsorted spike shape has no refractory period (top of **Fig. 5.4B**). The interspike interval distribution displayed here corresponds to the diffuse illumination tests shown in **Fig. 3.1**. Note that the sorted spikes have well defined shapes with no kinks in their standard deviations (red lines, **Fig. 5.4A**), and a clear refractory period at interspike intervals less than 1-2 ms (**Fig. 5.4B**).

The responses of each unit recorded within the NI were very qualitatively similar in response to all presented stimulus paradigms. For example, in response to a diffuse illumination step (**Fig. 3.1**), all units take part in a strong

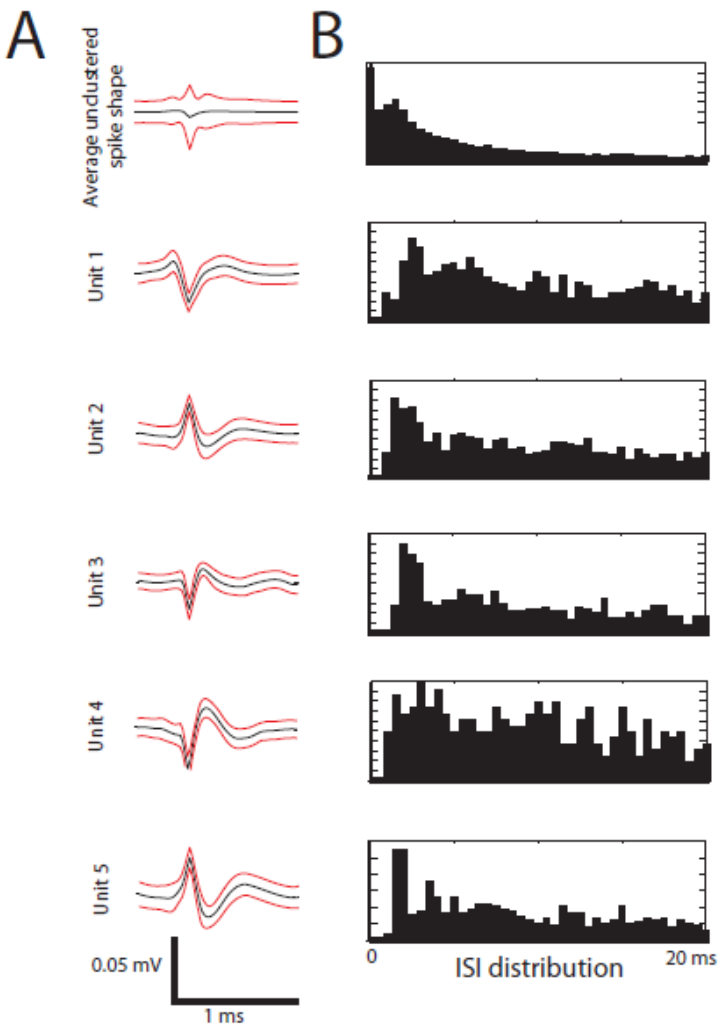

Figure 5.4: Sorted spike shapes and associated ISI distributions. In this penetration, there were 72,563 detected spikes. **(A)** Average spike shape of whole set of spikes (top) and of each cluster. **(B)** Associated ISI distributions for all of the spikes (top) and for each cluster in response to the diffuse illumination steps. Note the lack of refractory period for the whole group of spikes shown by large values at low ISI value. After clustering, none of the clusters displays ISIs under 1ms.

initial response to the ON step with approximately the same latency of 80-120 ms. All recorded units also displayed a sudden and long lasting quiescent period

following this strong burst of activity. All units then responded with a strong second wave of resurgent activity after 1,700 ms of the tacit response. This response was very robust and observed in all frogs studied. Even more peculiar responses, such as the delayed response to the cessation of motion of a moving spot (regardless of the direction of motion or size of spot) was shared among all units in all frogs (**Fig. 3.5**). The only apparent difference for any of these salient aspects of the response was the firing rates of the units.

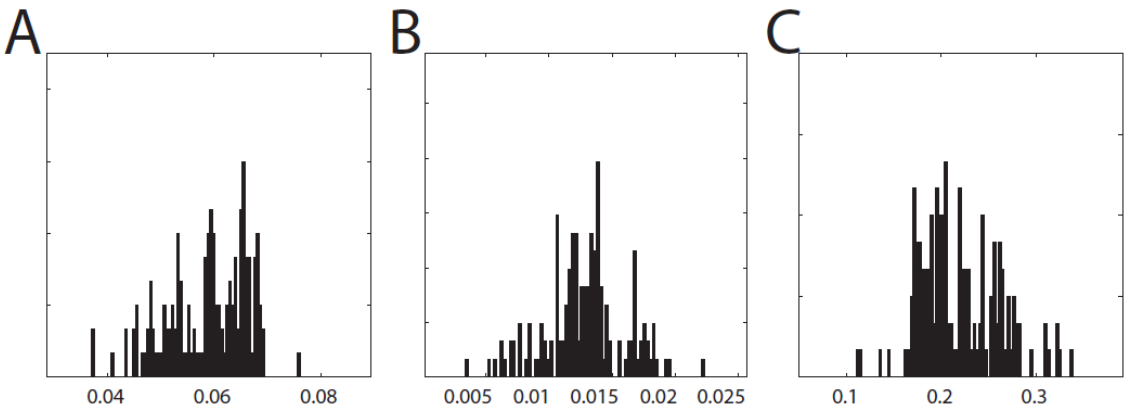

Figure 5.5: Probability distributions of the normalized responses of all recorded units to salient features of the responses to visual stimuli. **(A)** Responses to the close approach of a looming spot. **(B)** Responses to the delayed response of the cessation of a moving spot moving superior-inferiorly. **(C)** Responses to the ON step of diffuse illumination. All abscissa are unit less due to being normalized by the total number of spikes fired in response to a given stimulus paradigm by a given unit.

To quantify the differences of the responses, probability distributions were created of the normalized responses of each unit (**Fig. 5.5**). All response distributions appear to contain a spread of response values without any clear

separation into distinct clusters. That is, none of the salient aspects of the responses appear to have some units which contribute vigorously with other units quiescent. In summary, there do not appear to be any clear qualitative differences in the responses of the NI units.

This was further verified by performing PCA on a set of 80 units which were presented with all stimulus varieties (**Fig. 5.6**). No clear distinction can be

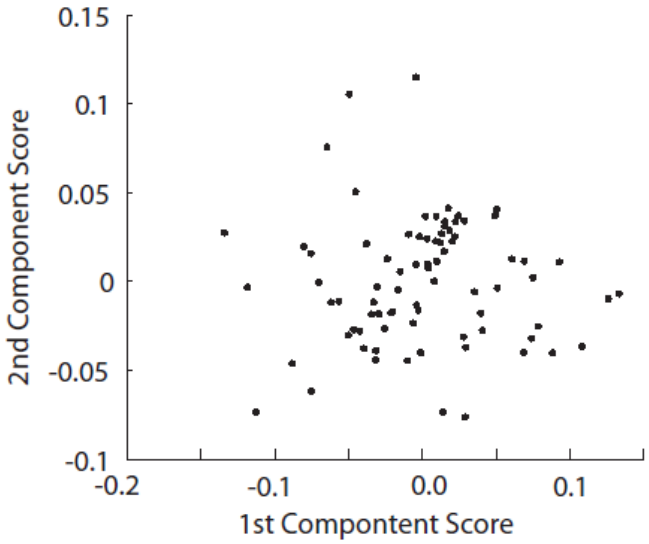

Figure 5.6: Projection of principle component scores onto the plane of first two principle components. Note the lack of any clear distinction between possible multiple clusters.

found in the sets of responses. If there is a set of NI units which responds vigorously to one aspect of a stimulus such as the dimming of light intensity or the motion of a spot, and a different set which responds to very different aspects of the visual scene, it should be apparent in the PCA. Yet, no structure is seen. There appears to simply be a distribution of excitability of units.

DISCUSSION:

In this study we have used two techniques to characterize the electrophysiological properties of frog NI neurons. First, we performed a principal component analysis on 10 variables that quantified the responses of NI cells to current injections *in-vitro.* This analysis reduced the number of dimensions of the parameter space of isthmic responses and demonstrated that no electrophysiological distinction could be made between isthmic cells. Secondly, we performed extracellular recordings *in vivo* of isthmic cells in response to diffuse illumination, moving spots, and looming spots. The responses of each set of simultaneously recorded units to all forms of visual stimuli showed no qualitative differences. Some complex times courses were observed for the responses and even these were shared by all recorded units at multiple locations throughout the NI. Together these results indicate that in response to somatic current injections and simple visual stimuli, the NI cells are electrophysiologically homogeneous. This result is surprising because several lines of evidence suggest that the NI may contain multiple populations. These include comparisons with isthmotectal systems from other vertebrates, anatomical connections in the isthmotectal system and isthmic neurotransmitter types.

The frog NI is similar to other vertebrates such as bony fish, reptiles and birds in that it makes reciprocal topographic projections with the ipsilateral OT (Gruberg et. al., 2006). However, in birds and reptiles the NI consists of two or three sub-nuclei with electrophysiologically distinct populations of neurons. In

birds, the isthmi pars parvocellularis (Ipc) and the isthmi pars magnocellularis (Imc) subnuclei differentially modulate tectal cell activity. The cholinergic Ipc projects in a narrow dorsoventral column in the OT while the GABAergic Imc projects feedback widely to the OT heterotopically (Wang et al., 2004; Wang et al., 2006). This spatial distribution allows the Imc and Ipc sub-nuclei to influence the responsiveness of tectal cells and draw attention to salient visual targets (Wang et al., 2000; Gruberg et. al., 2006). In the frog, differential responses have been extracellularly recorded throughout the OT layers in response to NI stimulation (Xiao et al., 1999). The latency of responses indicates that some of the connections between the NI and OT were monosynaptic while others were polysynaptic. Recent ultrastructural studies have shown that many contralaterally projecting isthmotectal axons terminate on GABA-immunoreactive dendrites in the OT (Rybicka et al., 2005). Thus it seems plausible that visual attention mechanisms may be mediated through inhibitory tectal interactions in the frog.

Anatomically, neurons of the frog NI are segregated into two spatially distinct groups; neurons in the dorsolateral half of the isthmi project to the ipsilateral OT and neurons in the ventromedial half project to the contralateral OT with no single cell projecting to both tectal lobes (Dudkin et. al., 2007). A similar bilateral connectivity pattern is found in the parabigeminocollicular pathway of mammals such as cats, rodents and primates (Wilson et al., 1970; Cynader et al., 1972; Graybiel, 1978; Cusick et al., 1982; Stevenson et al., 1982; Künzle et al., 1984; Mufson et al., 1986; Petry et al., 1989; Binns et al.,2000; Wu et al.,

2000; Major et al., 2003). For instance in rats, the PBN (homolog of the NI) is divided into a dorsal, middle and ventral division (Tokunaga et al., 1978; Jen et. al., 1984). The dorsal and ventral divisions project to the ipsilateral tectum and the middle division projects to the contralateral tectum (Jen et. al., 1984). We recorded from sites in both the dorsolateral and ventromedial frog NI and found no electrophysiological distinctions between the cells projecting ipsilaterally and contralaterally.

Neurons in the NI of amphibians, reptiles and birds as well as those of the PBN of mammals all stain for acetylcholinesterase (AChE) and acetyltransferase (ChAT) (Wang, 2002). In frogs, this cholinergic pathway can influence tectal cells and even retinal inputs (Dudkin et al., 2003). In addition, the NI has been shown to possess a population of GABA containing neurons that project to the OT (Li et al., 2001). This may account for the dual modulation of tectal cells observed when the NI is electrically stimulated (Hoshina et al., 2006; Xiao et al., 1999). Our recordings from the NI did not discern any electrophysiological distinctions between the cholinergic and GABAergic populations. It is possible that both populations possess similar electrophysiological properties or that one population greatly outnumbers the other so that the probability of having recorded from the minority population was low.

To summarize we have characterized the cellular and visual response properties of NI neurons. We examined cells in the dorsolateral half of the isthmi that contains neurons projecting to the ipsilateral OT and cells in the

ventromedial half of the NI projecting to the contralateral OT. We found no electrophysiolgical distinctions between the cells in response to either current injections in-vitro or simple visual stimuli in-vivo.

ACKNOWLEDGEMENTS:

I am very indebted to Matt Caudill for fruitful discussions about the tecto-isthmic system and his *in-vitro* work in the frog. Matt had to overcome tremendous obstacles to even obtain his intracellular recordings.

REFERENCES:

Binns KE, Salt TE The functional influence of nicotinc cholinergic receptors on the visual responses of neurons in the superficial superior colliculus. *Vis Neurosci.* 2000. **17**:283-289.

Butler AB, Hodos W Comparative vertebrate neuroanatomy: evolution and adaptation. 2005 Wiley, New York.

Cusick CG, Kaas JH Retinal projection in adulat and newborn grey squirrels. *Brain Res.* 1982. **256**:275-284.

Cynader M, Berman N Receptive field organization of monkey superior colliculus. *J Neurophysiol*. 1972. **35**:187-201.

Desan PH, Gruberg ER, Grewell KM, Eckenstein F. Cholinergic innervation of the optic tectum in the frog *Rana pipiens*. *Brain Res*. 1987. **413**:344-349.

Dudkin EA, Gruberg ER. Nucleus isthmi enhances calcium influx into optic nerve fiber terminals in *Rana pipiens. Brain Res.* 2003. **969**:44-52.

Dudkin EA, Sheffield JB, Gruberg ER. Combining visual information from the two eyes: The relationship between isthmotectal cells that project to ipsilateral and to contralateral optic tectum using fluorescent retrograde labels in the frog, *Rana pipiens*. *J Comp Neurol*. 2007. **502**:38-54.

Eggebrecht AT. Mechanisms of feedback within the visual system. Dissertation Ch. 2, 2009. Washington University Saint Louis.

Gaze RM. The representation of the retina on the optic lobe of the frog. *Q J Exp Physiol.* 1958. **43**:209-214.

Graybiel AM. A satellite system of the superior colliculus: the parabigemnal nucleus and its projections to the superficial collicular layers. *Brain Res* 1978. **145**: 365-374.

Gruberg E, Dudkin E, Wang Y, Marín G, Salas C, Sentis E, Letelier J, Mpodozis J, Malpeli J, Cui H, Ma R, Northmore D, Udin S. Influencing and interpreting visual input: The role of a visual feedback system. *J. Neurosci* 2006. **26**:10368-10371.

Gruberg ER, Udin SB Topographic projections between the nucleus isthmi and the tectum of the frog *Rana pipiens*. *J Comp Neurol*. 1978. **179**:487-500.

Gruberg ER, Wallace MT, Caine HS. Behavioral and physiological consequences of unilateral ablation f the nucleus isthmi in the leopard frog. *Brain Behav Evol*. 1991. **37**:92-103.

Hoshino N, Tsurudome K,Nakagawa H, Matusumoto N. Current source density analysis of contra- and ipsilateral isthmotectal connections in the frog. *Vis Neurosci*. 2006. **23**:713-719.

Jen LS, Dai ZG, So KF. The connections between the parabigeminal nucleus and the superior colliculus in the golden hamster. *Neurosci Lett*. 1984. **5**:189-194.

Jolliffe IT. Principal component analysis. 1986 Springer-Verlag, New York.

Khalil SH, Lázár GY. Nucleus isthmi of the frog: structure and tecto-isthmic projection. *Acta Morphol Acad Sci Hung*. 1977. **25**:51-59.

Kunzle H, Schnyder H. The isthmus-tegmentum complex in the turtle and rat: a comparative analysis of its interconnections with the optic tectum. Exp *Brain Res.* 1984. **56**:509-522.

Li Z, Fite KV. GABAergic visual pathways in the frog *Rana pipiens. Vis Neurosci* 2001. **18**:457-464.

Li Z, Wang SR, Xu HY. Acetylcholinesterase staining patterns ot the tectum-nucleus isthmi systems in frogs and pigeons. *Acta Anat Sinica* 1987 **18**:44-47.

Major DE, Rodman HR, Libedinsky C, Karten HJ. Pattern of retinal projections in the California ground squirrel spermophilus beecheyi: anterograde tracing study using cholera toxin. *J Comp Neurol* 2003. **463**:317-340.

Maturana HR. Number of fibers in the optic nerve and the number of ganglion cells in the retina of anurans. *Nature*. 1959. **183**:1406-1507.

Mufson EJ, Martin TL, Mash DC, Wainer BH, Mesulam MM. Cholinergic projections from the parabigeminal nucleus to the superior colliculus in the mouse: a combined analysis of horse radish peroxidase transport and choline acetyltransferase immunohistochemistry. *Brain Res.* 1986. **370**:144-148.

Petry HM, Agarwala S, May JG 3rd. Striped pattern of labeling in ground squirrel superior colliculus following intraocular HRP injections. *Brain Res* 1989. **489**:199-203.

Quiroga RQ, Nadasy Z, Ben-Shaul Y. Unsupervised spike detection and sorting with wavelets and superparamagnetic clustering. *Neural Comp* 2004. **16**:1661-1687.

Rybicka KK, Udin SB. Connections of contralaterally projecting isthmotectal axons and GABA-immunoreactive neurons in *Xenopus* tectum: An ultrastructural study. *Vis Neurosci* .2005. **22**:305-315.

Saha D, Ariel M, Wessel R. Dynamics of excitatory and inhibitory synaptic currents in a visual feedback loop in turtle. 2008 SFN poster #665.6

Shao J, Lai D, Meyer U, Luksch H, Wessel R. Generating oscillatory bursts from a network of regular spiking neurons without inhibition. *J Comput Neurosci*. Doi: 2009 10.1007/s10827-009-0171-5.

Sillito AM, Cudeiro J, Jones HE. Always returning: feedback and sensory processing in visual cortex and thalamus. *Trends in Neurosci.* 2006. **29**:307-316.

Soltesz I .Diversity in the neuronal machine. 2006 Oxford Univ. Press, New York.

Tokunaga A, Otani K .Neuronal organization of the corpus parabigeminum in the rat. *Exp Neurol* 1978. **58**:361-375.

Wallace MT, Ricciuti AJ, Gruberg ER. Nucleus isthmi: its contribution to tectal acetylcholinesterase and choline acetyltransferase in the frog *Rana pipiens. Neurosci*. 1990. **35**:627-636.

Wang S-R. The nucleus isthmi and dual modulation of tectal neurons in non-mammals. *Brain Res Rev* 2002. **41**:13-25.

Wang Y, Luksch H, Brecha NC, Karten HJ. Columnar projections from the cholinergic nucleus isthmi to the optic tectum in chicks *Gallus gallus*: a possible substrate for synchronizing tectal channels. *J Comp Neurol* 2006. **494**:7-35.

Wang Y, Major DE, Karten HJ. Morphology and connections of nucleus isthmi pars magnocellularis in chicks *Gallus gallus. J Comp Neurol.* 2004. **469**:275-297.

Wang Y, Xiao J, Wang SR. Excitatory and inhibitory receptive fields of tectal cells are differentially modified by magnocellular and parvocellular divisions of the pigeon nucleus isthmi. *J Comp Physiol A Neuroethol Sens Neural Behav* Physiol 2000. **186**:505-511.

Wilson ME, Toyne MJ. Retino-tectal and cortico-tectal projections in *Macaca mulatta. Brain Res* 1970. **24**:395-406.

Wu HH, Cork RJ, Huang PL, Shuman DL, Mize RR. Refinement of the ipsilateral retinocollicular projection is disrupted in double endothelial and neuronal nitric oxide synthase gene knockout mice. *Brain Res Dev Brain Res.* 2000. **120**:105-111.

Xiao J, Wang Y, Wang S-R.Effects of glutamatergic, cholinergic and GABAergic antagonist on tectal cells in toads. *Neurosci* 1999. **90**:1061-1067.

Yu CJ, Debski EA. The effects of nicotinic and muscarinic receptor activation on patch-clamped cells in the optic tectum of *Rana pipiens. Neurosci.* 2003. **118**:135-144.

Chapter 6:

CONCLUSIONS AND FUTURE DIRECTIONS

This dissertation addresses the mechanisms of a feedback loop in the visual system. As a model system, we used the leopard frog, *Rana pipiens*, due to the accessibility of the OT and the NI and because the loop of interest is well isolated from the rest of the neural architecture. Because this system had not been previously characterized in the time domain, and because timing is of critical importance when considering not only what effects a feedback loop has on the information processing of the neural system, but also in what ways the feedback loop can interact to bring about those effects, we set out to characterize the responses of the NI to visual stimuli with a focus on the time courses of the responses.

In **Chapter 2**, the spike sorting procedure used throughout the extracellular recordings was explained. We developed a novel threshold to use on the filtered voltage waveform. This threshold is robust down to a low signal-to-noise level and the algorithm it uses may be completely unsupervised allowing for a fast and efficient implementation. The fact that the threshold works well in a low signal-to-noise environment makes it ideally suited for use in the frog's NI because of the small and densely packed cell bodies from which we recorded.

Also, the complete spike sorting procedure was detailed to show how the false-positives detected by the threshold can be clustered out of the set of actual spike shapes with a high confidence level. In addition, this chapter details how, with one extracellular electrode placement, we can actually record simultaneously the activity of 1-7 well separated units within the neural tissue.

This threshold and spike sorting procedure were utilized in **Chapter 3** where the temporal aspects of the frog's NI responses to dynamic visual stimuli were first observed. The responses display surprisingly long time courses which are explainable neither by the time course of the visual stimuli nor by the activity within the OT to the same classes of stimuli. Specifically, following an ON step in diffuse illumination, all NI units respond with a strong initial response, followed by over a second of suppressed response. The units then display a strong second wave of activity which lasts well over one second. These long time courses are unexpected given known normal cellular process time constants as well as the known network architecture. Also, in response to the cessation of a moving spot, there is a significant response in all units which is delayed by over two seconds. While this may reflect a tectal input from a small population of neurons, the specific cause for the long time delay remains a mystery.

The time course of the responses within the NI to visual stimuli was further explored in **Chapter 4**, this time to visual stimuli which incorporates contextual interactions. In response to a stimulus presented simultaneously outside of the receptive field as well as inside the receptive field led to a larger response from

all units than to a stimulus presented within the receptive field alone. While this response appears counterintuitive, it may be evidence for an asymmetric winner-take-all mechanism within the tectoisthmic system. This winner-take-all system may be constructed out of the asymmetric levels of cholinergic feedback from the NI onto topographic and visuotopic locations within the superficial layers of the OT. This cholinergic feedback may use a paracrine mechanism of neurotransmitter release which causes the acetylcholine to affect the axon terminals of the RGCs in a way which increases their likelihood of synaptic transmission. At the same time, either the acetylcholine or the choline left after the acetylcholinestherase breaks down the acetylcholine may act preferentially as either an excitatory or inhibitory agent on the GABAergic interneurons found throughout the superficial OT.

Oscillations in the population response of the NI units were also observed in response to the contextual stimuli. These may be caused by a global local field potential within the OT which drives the excitability of the neurons as is seen in the thalamus of mammals. The tectal local field potential displays an oscillation of its coherence which may be moderated by retinal inputs. We created a model based on the known connectivity of the tectoisthmic system with biologically constrained parameters. We found that the oscillations seen in the isthmic response must indeed be driven by a global modulation of the OT. This oscillation must arise within the retina or may possibly be due to non-trivial interactions with the tectal circuitry. The model was able to reproduce the

oscillatory aspect of the isthmic response seen in **Chapter 4** but not the non-trivial responses seen over longer time courses seen in **Chapter 3.**

In **Chapter 5**, intracellular data from current injections was combined with a comparative analysis of the extracellular responses to visual stimuli. Principal component analysis was performed on the set of variables extracted from the intracellular data. No clear distinctions in the electrophysiological properties of the NI neurons have been found. PCA analysis was also performed on the set of normalized responses of 80 neurons within all regions of the NI. Here also we failed to separate possible clusters within the data. This is a surprise given that in other systems there is a clear heterogeneity in the population of isthmic neurons. In addition, the NI of the frog displays multiple neurotransmitter types, and contains separate sets of neurons which project either ipsilaterally or contralaterally

Many questions remain to be answered so that a fuller picture of the role of the NI in the tectoisthmic feedback loop can be understood. There is still no data supporting or disproving intra-isthmic connections, aside from a small number of gap junctions. It is unclear how many isthmic cells contain GABA and whether or not this neurotransmitter is used in an isthmotectal projection. It is not known what types of GABA receptors are present on isthmic neurons. A systematic study of intracellular fills of isthmic cells would illuminate the morphology of the isthmic neurons. This may help answer questions about the

extent of intra-isthmic connections as well as the level of convergence in the tectoisthmic projection.

The results herein raise further questions. Can isthmic units respond during the suppressed activity following an ON step? If not, is this caused by a synaptic depression or by a strong inhibition? If the latter, then GABA blockers may be useful in finding the receptors present in the isthmi. If it is GABA, then from where is the GABAergic projection? Is the delayed response to the cessation of motion caused or affected by the feedback from the isthmi to the tectum? Acetylcholine blockers may be able to block the feedback without affecting the rest of the neural circuit. If the NI feedback does not affect this, what functional use does the feedback serve? Is it contributing to predictive responses as evidenced by the fact that the isthmic units peak in firing to the looming stimuli is, in many cases, at the moment of collision even though there is an 80-120 ms latency in response?

While many questions remain unanswered, this project has served to uncover the temporal aspects of the responses of units within the NI to dynamic visual stimuli. This provides a necessary further step in unraveling the role of isthmo-tectal feedback in the processing of visual information.